# Aspects of Chiral Symmetry Breaking in Lattice QCD

Derek P. Horkel

A dissertation
submitted in partial fulfillment of the
requirements for the degree of

Doctor of Philosophy

University of Washington

2016

Reading Committee:

Stephen R. Sharpe, Chair

Silas Beane

Nikolai Tolich

Program Authorized to Offer Degree:
Physics

University of Washington

**Abstract**

Aspects of Chiral Symmetry Breaking in Lattice QCD

Derek P. Horkel

Chair of the Supervisory Committee:
Professor Stephen R. Sharpe
Physics

In this thesis we describe two studies concerting lattice quantum chromodynamics (LQCD): first, an analysis of the phase structure of Wilson and twisted-mass fermions with isospin breaking effects, second a computational study measuring non-perturbative Greens functions. We open with a brief overview of the formalism of QCD and LQCD, focusing on the aspects necessary for understanding how a lattice computation is performed and how discretization effects can be understood. Our work in Wilson and twisted-mass fermions investigates an increasingly relevant regime where lattice simulations are performed with quarks at or near their physical masses and both the mass difference of the up and down quarks and their differing electric charges are included. Our computation of a non-perturbative Greens functions on the lattice serves as a first attempt to validate recent work by Dine et. al. [24] in which they calculate Greens functions which vanish in perturbation theory, yet have a contribution from the one instanton background.

In chapter 2, we determine the phase diagram and pion spectrum for Wilson and twisted-mass fermions in the presence of non-degeneracy between the up and down quark *and* discretization errors, using Wilson and twisted-mass chiral perturbation theory. We find that the CP-violating phase of the continuum theory (which occurs for sufficiently large non-degeneracy) is continuously connected to the Aoki phase of the lattice theory with degenerate quarks. We show that discretization effects can, in some cases, push simulations with

physical masses closer to either the CP-violating phase or another phase not present in the continuum, so that at sufficiently large lattice spacings physical-point simulations could lie in one of these phases.

In chapter 3, we extend the work in chapter 2 to include the effects of electromagnetism, so that it is applicable to recent simulations incorporating all sources of isospin breaking. For Wilson fermions, we find that the phase diagram is unaffected by the inclusion of electromagnetism—the only effect is to raise the charged pion masses. For maximally twisted fermions, we previously took the twist and isospin-breaking directions to be different, in order that the fermion determinant is real and positive. However, this is incompatible with electromagnetic gauge invariance, and so here we take the twist to be in the isospin-breaking direction, following the RM123 collaboration. We map out the phase diagram in this case, which has not previously been studied. The results differ from those obtained with different twist and isospin directions. One practical issue when including electromagnetism is that the critical masses for up and down quarks differ. We show that one of the criteria suggested to determine these critical masses does not work, and propose an alternative.

In chapter 4, we delve deeper into the technical details of the analysis in chapter 3. We determine the phase diagram and chiral condensate for lattice QCD with two flavors of twisted-mass fermions in the presence of nondegenerate up and down quarks, discretization errors and a nonzero value of $\Theta_{\mathrm{QCD}}$. We find that, in general, the only phase structure is a first-order transition of finite length. Pion masses are nonvanishing throughout the phase plane except at the endpoints of the first-order line. Only for extremal values of the twist angle and $\Theta_{\mathrm{QCD}}$ ($\omega = 0$ or $\pi/2$ and $\Theta_{\mathrm{QCD}} = 0$ or $\pi$) are there second-order transitions.

In chapter 5 we move on to a new topic, working to make a first measurement of non-perturbative Greens functions which vanish in perturbation theory but have a non-vanishing one-instanton contribution, as suggested in recent work by Dine et. al. [24] using a semi-classical approach. This measurement was done using $16^3 \times 48$ configurations generated by

the MILC collaboration, with coupling $\beta = 6.572$, light quark mass $m_\ell a = 0.0097$, strange quark mass $m_s a = 0.0484$, lattice spacing $a \approx 0.14$ fm and pion mass $m_\pi a = 0.2456$. The analysis was done by separating the Green function of interest into pseudoscalar and scalar components. These are separately calculated on 440 configurations, using the Chroma software package. To improve statistics, we used the various reduction technique suggested in Ref. [13]. We subtracted out the long distance contributions from the pion, excited pion and $a_0$ from the Green function, in the hope of obtaining the short distance form predicted by Ref. [24]. Unfortunately, after subtraction of the $a_0$ and pion states only noise remained. While the results are not in themselves useful, we believe this approach will be worth repeating in the future with finer lattices with a fermion action with better chiral symmetry.

# TABLE OF CONTENTS

# LIST OF FIGURES

# LIST OF TABLES

# ACKNOWLEDGMENTS

I would like to thank my advisor, Steve Sharpe. In our 3 years working together, Steve has artfully guided me towards projects which both have pushed me to learn new skills while utilizing and improving my strengths. He has given me invaluable advice, criticism and feedback without which I could not have grown and flourished as a physicist. Beyond strictly academic matters, Steve has always been incredibly understanding when life gets in the way of research.

Next I would like to thank both the professors and my peers in UW's Particle Theory group, Nuclear Theory group, and INT. They have helped me learn both by giving memorable talks and lectures, and by attending and offering guidance during my many journal club and other practice talks throughout the years. In particular, would like to thank my current and former office mates, who have acted as a sounding board for all matters, academic and otherwise. Special mention also goes to Michael Wagman who spent many hours with to get Chroma working and Akshay Ghalsasi with whom I have worked on innumerable assignments and enjoyed innumerable meals.

I thank my exam committee, and in particular my reading committee. They offered tough but fair questioning during both my general exams and have made the cat-herding which is scheduling as painless as possible.

I could not have made it to this point without my family: my father, sister and grandmother who have always believed in me, even when I haven't believed in myself.

Lastly, I thank my fiance, Elise, who has stayed beside me and supported me despite living 3,000 miles apart during the 5 years of each of our graduate programs. We have survived this challenge as I know we will survive all those ahead of us.

This work was facilitated though the use of advanced computational, storage, and networking infrastructure provided by the Hyak supercomputer system at the University of Washington. The measurements done in Ch. 5 was performed using the Chroma software package, distributed by JLab [27].

# DEDICATION

For my father

# Chapter 1
# INTRODUCTION

In this Introduction, we present a brief overview of some of the important ideas and tools used in the main body of this thesis. We begin in Sec. 1.1 with an introduction to lattice quantum chromodynamics (LQCD) and lattice hadron spectroscopy which are utilized in Ch. 5. In Sec. 1.2 we give a minimal introduction to chiral perturbation theory which is the primary tool used in Ch. 2-4.

## *1.1 Introduction to lattice QCD*

In this section, we present an concise overview of the formulation of LQCD with a focus on the portions which are relevant to the main body of this dissertation. In the following we derive the Wilson gauge action, discuss various formulations of lattice fermions, and summarize steps in implementing a computer simulation, including building and extracting correlation functions. The following discussion is carried out entirely in Euclidean spacetime, which is obtained from Minkowski time $t$ by Wick rotating as $t \to i\tau$. A finite temperature, $T$, can be included in a lattice formulation by making the Euclidean time direction periodic with period of the inverse temperature and identifying $\tau_{max} = 1/T$. For the sake of brevity, this discussion only considers zero temperature where $\tau$ is unbounded.

### *1.1.1 Continuum Gauge Action*

The continuum QCD gauge action is,

$$S_{gauge} = \frac{1}{2g^2} \int d^4x \, \mathrm{tr}(G^b_{\mu,\nu}(x) G_b^{\mu,\nu}(x)) \tag{1.1}$$

where $G^b_{\mu,\nu}$ is the gluon field strength tensor and "$b$" is color index, running from 1 to 8 over the eight generators of QCD gauge group, SU(3). "$\mu$" and "$\nu$" run from 1 to 4 over the 4 Euclidean spacetime directions. $G^b_{\mu,\nu}$ can be expressed in terms of the gauge field, $A^b_\mu$,

$$G^b_{\mu,\nu}(x) = \partial_\mu A^b_\nu(x) - \partial_\nu A^b_\mu(x) + i\left[A^c_\mu(x), A^d_\nu(x)\right] f^{bcd}, \qquad A^b_\mu(x) = A_\mu(x)T^b \ .$$

where $f^{bcd}$ is the group structure constant and $T^b$ are the 3x3 traceless hermitian Gell-Mann matrices which are the generators of SU(3). $G^b_{\mu,\nu}$ transforms under a local SU(3) transformation $\Omega(x)$ as,

$$G^b_{\mu,\nu}(x) \to G'^b_{\mu,\nu}(x) = \Omega(x) G^b_{\mu,\nu}(x) \Omega^\dagger(x) \ . \tag{1.2}$$

As seen from the presence of the gauge fields multiplying the generators, the continuum action is written in term of elements of the group algebra su(3) rather than than group elements. The following presents the lattice gauge action, written in terms group elements. By construction, the lattice action obtained agrees with Eq. 1.1 in the continuum limit.

### *1.1.2 Discretized Action*

In order to discretize QCD, spacetime must first be discretized. The simplest and most widely used discretization is a four-dimensional hypercubic lattice with lattice spacing $a$. The four-dimensional position vector $x$ is replaced by a discrete position vector $n = (n_x, n_y, n_z, n_\tau)$ and the spacetime integral is replaced by a discrete sum,

$$x = (x, y, z, \tau) \to an = a(n_x, n_y, n_z, n_\tau), \qquad \int d^4x \to a^4 \sum_n \ .$$

Rather than considering the $A^b_\mu$'s as the gluon degrees of freedom, we instead use Wilson lines of length $a$ connecting adjacent lattice sites

$$U_\mu(n) = \exp(ia \sum_{b=1}^{8} A^b_\mu(n)) \ .$$

Here $\mu$ is the direction of the link and $n$ is the location of the starting lattice site, as can be seen in Fig. 1.1 These gauge links transform on the left at the starting point of the link and

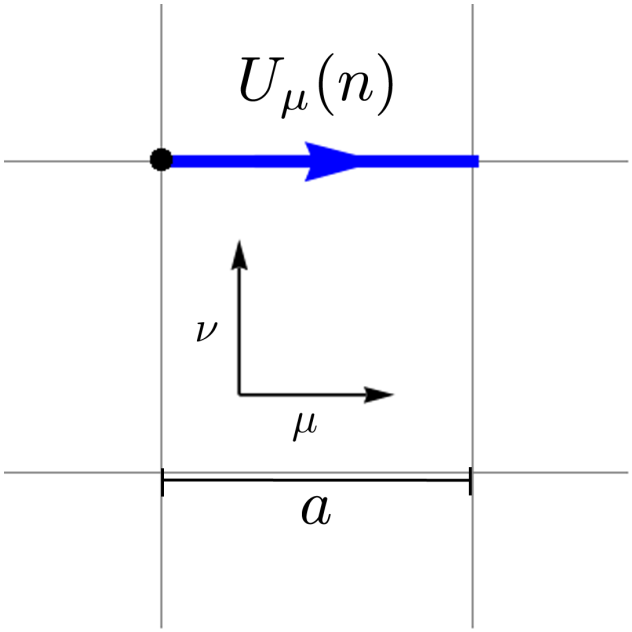


Figure 1.1: Gauge field link at point $n = (n_x, n_y, n_z, n_\tau)$

on the right at the end point

$$U_\mu(n) \to U'_\mu(n) = \Omega(n) U_\mu(n) \Omega^\dagger(n + \hat{\mu}) \ . \tag{1.3}$$

A gauge invariant action can be constructed from a path ordered product of links forming a closed loop. The simplest non-trivial gauge invariant product of links is called an elementary plaquette; it is formed by making a 1x1 loop of links.

$$\begin{aligned} \mathrm{tr}(\mathcal{P}_{\mu,\nu}(n)) &= \mathrm{tr}\left(U_\mu(n) U_{-\nu}(n + \hat{\mu}) U_{-\mu}(n + \hat{\mu} - \hat{\nu}) U_\nu(n - \hat{\nu})\right) \\ &\to \mathrm{tr}(\Omega(n) U_\mu(n) \Omega^\dagger(n + \hat{\mu}) \Omega(n + \hat{\mu}) U_{-\nu}(n + \hat{\mu}) \Omega^\dagger(n + \hat{\mu} - \hat{\nu}) \\ &\Omega(n + \hat{\mu} - \hat{\nu}) U_{-\mu}(n + \hat{\mu} - \hat{\nu}) \Omega^\dagger(n - \hat{\nu}) \Omega(n - \hat{\nu}) U_\nu(n - \hat{\nu} \Omega^\dagger(n))) \\ &= \mathrm{tr}\left(U_\mu(n) U_{-\nu}(n + \hat{\mu}) U_{-\mu}(n + \hat{\mu} - \hat{\nu}) U_\nu(n - \hat{\nu})\right) \end{aligned} \tag{1.4}$$

Links oriented in the $-\mu$ and $-\nu$ directions can be related to the links in the positive direction as,

$$U_{-\mu}(n) = U_\mu(n - \hat{\mu})^\dagger \ . \tag{1.5}$$

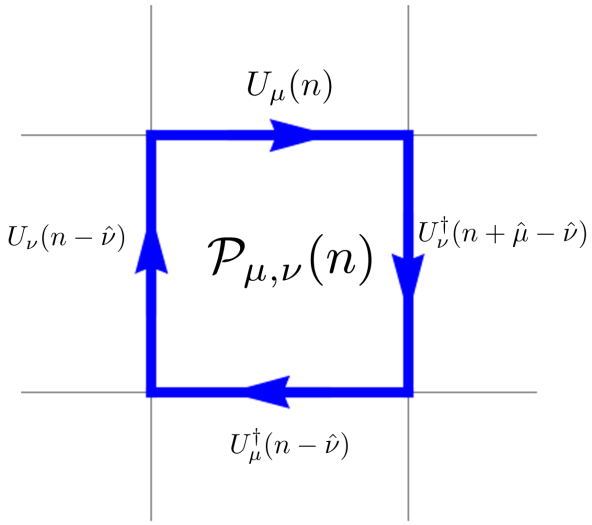


Figure 1.2: Elementary plaquette

A picture of a plaquette, labeled using only positively oriented links is shown in Fig. 1.2.

One form of the action that can be constructed out of plaquettes is the Wilson action,

$$S_{gauge} = \frac{4}{g^2} \sum_n \sum_{\mu,\nu} \mathrm{Re}\,\mathrm{tr}(\mathbb{1} - \mathcal{P}_{\mu,\nu}(\mathrm{n})) \ . \tag{1.6}$$

To see that this form is consistent with continuum action in the continuum limit, $a \to 0$, each link can be Taylor expanded in powers of $a$. In order to maintain a local action, gauge fields that result from links shifted from point $n$ in the $\hat{\mu}$ or $\hat{\nu}$ direction can themselves be expanded in terms of derivatives of the gauge field

$$A_\mu(n+\hat{\nu}) = A_\mu(n) + a\partial_\nu A_\mu(n) + \mathcal{O}(a^2) \ . \tag{1.7}$$

Collecting terms is a simple yet tedious exercise which can be found in some greater detail in [32]. The action that results from this expansion is,

$$S_{gauge} = \frac{a^4}{2g^2} \sum_n \sum_{\mu,\nu} \left(\mathrm{tr}(G^b_{\mu,\nu}(n) G^{\mu,\nu}_a(n)) + \mathcal{O}(a^2)\right) \ . \tag{1.8}$$

In the $a \to 0$ limit, assuming that fields, $G$, are smoothly varying on the scale of the lattice spacing, the sum over $n$ is converted to an integral over $x$ and $\mathcal{O}(a^2)$ terms vanish, yielding the original continuum action Eq. 1.1.

### *1.1.3 Lattice fermions*

In order to discretize the fermion part of the QCD action, we start with the continuum action,

$$S_{fermion} = \int d^4x \overline{\psi}(x) \left(\gamma_\mu \mathcal{D}_\mu(x) + m\right) \psi(x), \quad \mathcal{D}_\mu(x) = \partial_\mu + iA_\mu(x) \ . \tag{1.9}$$

In general, the fermion field $\psi$ can be a vector of dimension $N_f$, the number of flavors, in which case $m$ is an $N_f \times N_f$ mass matrix. For simplicity, we focus on one flavor here. The components of the action transform as,

$$\begin{aligned}
&\psi(x) \to \psi'(x) = \Omega(x)\psi(x), \\
&\overline{\psi}(x) \to \overline{\psi}'(x) = \overline{\psi}(x)\Omega^\dagger(x), \\
&\mathcal{D}_\mu(x) \to \mathcal{D}'_\mu(x) = \Omega(x)\mathcal{D}_\mu(x)\Omega^\dagger(x) \ .
\end{aligned}$$

In order to discretize, it is easiest to start with the free theory, without gauge fields, and insert gauge links where needed to have a gauge invariant action. In addition to replacing the integral with a sum, the derivative acting on $\psi$ must be replaced with a finite difference

$$\partial_\mu \psi(x) = \frac{1}{2a}(\psi(n+\hat{\mu}) - \psi(n-\hat{\mu})) \ . \tag{1.10}$$

The discretized free fermion action is now

$$S_{free} = a^4 \sum_n \overline{\psi}(n) \left(\gamma_\mu \frac{(\psi(n+\hat{\mu}) - \psi(n-\hat{\mu}))}{2a} + m\psi(n)\right) \ . \tag{1.11}$$

From the above gauge transformation of $\psi$ and $\overline{\psi}$ it is clear the finite difference term is not gauge invariant. This can be fixed by inserting gauge links

$$\overline{\psi}(n)U_\mu(n)\psi(n+\hat{\mu}) \to \overline{\psi}(n)\Omega^\dagger(n)\Omega(n)U_\mu(n)\Omega^\dagger(n+\hat{\mu})\Omega(n+\hat{\mu})\psi(n+\hat{\mu}) \ . \tag{1.12}$$

This yields the discretized fermion action,

$$S_{fermion} = a^4 \sum_n \overline{\psi}(n) \left( \gamma_\mu \frac{U_\mu(n)\psi(n+\hat{\mu}) - U_\mu^\dagger(n-\hat{\mu})\psi(n-\hat{\mu})}{2a} + m\psi(n) \right) . \tag{1.13}$$

Similar to the gauge action, this action also agrees with the continuum action in the $a \to 0$ limit. This action is referred to as the naive fermion action. It is called "naive" due to having doublers, which are unphysical quark mass poles. This can be seen by looking at the naive Dirac operator, $D(n,m)$,

$$S_{fermion} = a^4 \sum_{n,m} \overline{\psi}(n) D(n,m) \psi(m) \tag{1.14}$$

$$D(n,m) = \gamma_\mu \frac{U_\mu(n)\delta_{n+\hat{\mu},m} - U_\mu^\dagger(n-\hat{\mu})\delta_{n-\hat{\mu},m}}{2a} + m\psi(n)\delta_{n,m} . \tag{1.15}$$

One way to see the presence of doublers is to restrict ourselves to the free theory, $U_\mu(n) = \mathbb{1}$, and Fourier transforming the naive Dirac operator. Skipping intermediate steps [32], the Fourier transformed naive Dirac operator is,

$$\tilde{D}(n,m) = \frac{1}{V} \sum_{n,m} e^{-ip\cdot na} D(n,m) e^{iq\cdot ma} \tag{1.16}$$

$$= \delta(p-q) \left( m\mathbb{1} + ia^{-1}\gamma_\mu \sin(p_\mu a) \right) = \delta(p-q)\tilde{D}(p) . \tag{1.17}$$

Where $V$ is the lattice spacetime volume and $p_\mu$, $q_\mu$ are momenta which have values in the range $(-\pi/a, \pi/a]$ with $-\pi/a$ and $\pi/a$ identified. This operator can then be inverted to obtain the quark propagator,

$$\tilde{D}^{-1}(p) = \frac{m\mathbb{1} - ia^{-1}\gamma_\mu \sin(p_\mu a)}{m^2 + a^{-2}\sum_\mu \sin^2(p_\mu a)} . \tag{1.18}$$

The sum over $\mu$ in the denominator is shown explicitly to emphasize that it is separate from the sum in the numerator. The doublers are easiest to see in limit of massless quarks, $m \to 0$, where the propagator has the form,

$$\tilde{D}^{-1}(p)|_{m=0} = \frac{-ia\gamma_\mu \sin(p_\mu a)}{\sum_\mu \sin^2(p_\mu a)} . \tag{1.19}$$

Taking the continuum limit with fixed $p$ results in the correct pole at $p = (0, 0, 0, 0)$. For non-zero lattice spacing, poles appear whenever one or more components of $p$ equals $\pi/a$, resulting in 15 non-physical doublers.

There are several solutions which eliminate the undesired doublers, each having their own benefits, which we briefly discuss after introducing the simplest solution, Wilson fermions.

### *1.1.4 Wilson Fermions*

The earliest solution to the doubling problem is the use of Wilson fermions [cite Wilson]. The idea behind Wilson fermions is to add a term to the action that vanishes in the continuum limit while giving the doublers masses proportional to $a^{-1}$ such that they become extremely massive and decouple from the theory as $a \to 0$. This is accomplished by subtracting a discretized covariant Laplacian from the naive Dirac operator,

$$D(n,m)_{Wilson} = D(n,m)_{naive} - a\frac{U_\mu(n)\delta_{n+\hat{\mu},m} - 2\delta_{n,m} + U_\mu^\dagger(n-\hat{\mu})\delta_{n-\hat{\mu},m}}{2a^2} \ . \tag{1.20}$$

For the free theory, this results in the inverse propagator, in momentum space,

$$\tilde{D}(p) = \left( m\mathbb{1} + ia^{-1}\gamma_\mu \sin(p_\mu a) + a^{-1}\sum_\mu (1 - \cos(p_\mu a))\mathbb{1} \right) \ . \tag{1.21}$$

The added term (the last term) vanishes both for fixed $p$ as $a \to 0$ and at the massless physical pole, $p = (0, 0, 0, 0)$. Each doubler has an effective mass of

$$m_{doubler} = m + \frac{2N}{a} \tag{1.22}$$

where $N$ is the number of components of $p$ equal to $\pi/a$.

While Wilson fermions solve the doubling problem, the solution comes at the expense of chiral symmetry, which is discussed further in Sec. 1.2. One modification to the Wilson action is twisted mass where the quark mass matrix is given an axial $\mathrm{SU(N_f)}$ phase such that the mass and Wilson terms in the action do not mix. Twisted mass fermions are one of the main focuses of this dissertation and are discussed in much greater detail in chapter 2.

### *1.1.5 Numerical simulation*

The basic principle behind an actual lattice simulation is considering the exponential of the action as a probability density function describing the importance of various configurations of gauge fields. In order to have a probability density function that can be accurately sampled with a finite number of gauge configurations, it is necessary to rotate to Euclidean time,

$$\mathcal{Z} = \int \mathcal{D}\left(U\right) \mathcal{D}\left(\psi\right) \mathcal{D}\left(\overline{\psi}\right) e^{-S_{Euclidean}} \ . \tag{1.23}$$

This formulation favors configurations with lower action, which is consistent with the principle of least action from classical physics [1]

In order to include fermions, the Grassmann Gaussian integral over the fermionic fields is performed, replacing the integral over $\psi$ and $\overline{\psi}$ with a factor of the determinant of the Dirac operator for each flavor. This fermion determinant then acts as a weighting, changing the importance of different gauge field configurations,

$$\int \mathcal{D}\left(U\right) \mathcal{D}\left(\psi\right) \mathcal{D}\left(\overline{\psi}\right) e^{-(S_{gauge} + \int d^4x \overline{\psi}\left(\not{D} + m_f\right)\psi} = \int \mathcal{D}\left(U\right) \left( \prod_f \det\left[\not{D} + \mathrm{m_f}\right] \right) e^{-S_{gauge}} \ . \tag{1.24}$$

In continuum field theory, expectation values of operators are calculated just like moments of a probability density, by integrating the operator over configuration space, weighted by the exponentiated action and normalized by the partition function,

$$\langle \mathcal{O} \rangle = \frac{1}{\mathcal{Z}} \int \mathcal{D}\left(U\right) \mathcal{D}\left(\psi\right) \mathcal{D}\left(\overline{\psi}\right) e^{-S_{Euclidean}} \mathcal{O}\left(U, \psi, \overline{\psi}\right) \ . \tag{1.25}$$

An alternative, equivalent approach, is to calculate the operator and average over configurations which are selected from the probability distribution. If the selected configurations faithfully sample all of configuration space, the expectation values of operators can be calculated with errors which scale as $N^{-1/2}$ where $N$ is the number of configurations sampled,

$$\langle \mathcal{O} \rangle = \lim_{N \to \infty} \frac{1}{N} \sum_{conf} \mathcal{O}\left(U, \psi, \overline{\psi}\right) = \frac{1}{N} \sum_{conf} \mathcal{O}\left(U, \psi, \overline{\psi}\right) + O(1/\sqrt{N}) \ . \tag{1.26}$$

---

[1] In actuality, classical physics is restricted to a stationary action, $\delta S = 0$, such that the action is a local minima but not necessarily a global minima.

The numerical challenge is now to generate an ensemble of gauge field configurations which sample the distribution of possible gauge fields. In order to sample the physical ensemble, this generation must be aperiodic and ergodic, meaning every possible configuration could eventually be reached.

The basic procedure for generating these configurations begins with thermalization. Configurations are first initialized, most often with either a "cold start" or a "hot start" where each link is set to the identity or a random SU(3) phase, respectively. Then, each link is sucessively updated. There are several kinds of update algorithms but the simplest is the Metropolis update. In a Metropolis update, a candidate link is obtained by making a small change to the original link by multiplying it by an SU(3) matrix, $X$, which is near the identity,

$$U_\mu(n)^{candidate} = XU_\mu(n)^{old} \ . \tag{1.27}$$

This change is accepted if it lowers or does not change the action, and is accepted with probability,

$$e^{-(S(U^{candidate})-S(U^{old}))} \tag{1.28}$$

if the action is increased. This process must be repeated until the configuration generated can be said to have thermalized. There are multiple ways to check when thermalization has been attained, typically involving measuring when observables, such as the average plaquette value, fluctuate about a stable value. Factors that can result in more configurations needing to be generated until thermalization include small gauge coupling, $g$, and large lattice sizes. How close the candidate generating matrix $X$ is to the identity can also effect thermalization. Too small of a change and the gauge fields will change slowly, too large of a change and the action may greatly increase, causing candidate gauge fields to be rejected. In practice, thermalization can be somewhat sped up by using sequences of different update algorithms.

Once thermalized, future configurations can be used for actual measurements of QCD observables. Due to the sequential nature of the update, successive configurations are correlated. In order for errors to be well understood and fall as $N^{-1/2}$, this correlation must be

accounted for. One strategy is to only save configurations that are sufficiently spaced out along the chain of successive updates. This spacing is chosen by determining the correlation between measurements of a representative operator, such as the average plaquette. The details are beyond the scope of this introduction and are discussed elsewhere, such as [32]. Another strategy is blocking the configurations. Rather than considering the mean value of some operator on each configuration, the mean value on a block of $M$ configurations is measured. The size of each block, $M$, is increased, until the variance falls as $M^{-1}$, at which point, the measurement on each block can be considered independent.

The number of independent configurations required for a measurement depends on the quantity's intrinsic fluctuation, measured by its standard deviation, and the desired precision. It is desirable to include enough configurations such that the statistical error is smaller than any systematic errors. In practice, modern studies typically use hundreds to thousands of configurations.

### *1.1.6 Hadron correlators*

In order to discuss hadronic states, we must first introduce the Euclidean correlator. Consider some operator $\widehat{O}$ which acts on a Hilbert space to either create or destroy a state. Using the completeness relationship in some orthonormal basis,

$$\mathbb{1} = \sum_n |e_n\rangle\langle e_n| \tag{1.29}$$

the trace of the operator $\widehat{O}$ is defined as,

$$\mathrm{tr}\left(\widehat{O}\right) = \sum_n \langle e_n|\widehat{O}|e_n\rangle \ . \tag{1.30}$$

A Euclidean correlator relates states that are created or destroyed at some space-time separation $x_\mu$. As we are interested in the energies of hadron states, we will restrict ourselves to Euclidean time separations, $\tau$. The points are connected using the Euclidean time evolution operator $e^{-\widehat{H}\tau}$ where $\widehat{H}$ is the Hamiltonian operator. Considering a space-time which is

periodic in the time direction, as is the case in many lattice simulations, the returning time evolution operator is $e^{-\widehat{H}(\tau_{max}-\tau)}$. A general Euclidean correlator then has the form,

$$\langle O_2(\tau)O_1(0)\rangle = \frac{1}{\mathcal{Z}}\,\mathrm{tr}\left(e^{-\widehat{H}(\tau_{max}-\tau)}\widehat{O}_2 e^{-\widehat{H}\tau}\widehat{O}_1\right)\ , \tag{1.31}$$

where the normalization factor is $\mathcal{Z} = \mathrm{tr}\left(e^{-\widehat{H}\tau_{max}}\right)$. The natural choice of basis is the eigenstates of $\widehat{H}$, where $\widehat{H}|n\rangle = E_n|n\rangle$. Here $E_n$ are the discrete real valued energy eigenvalues chosen to be ordered such that,

$$E_0 \leq E_1 \leq E_2... \tag{1.32}$$

where $E_0$ is the vacuum energy. In this basis, the Euclidean correlator becomes,

$$\langle O_2(\tau)O_1(0)\rangle = \frac{1}{\mathcal{Z}}\sum_{m,n}\langle m|\widehat{O}_2|n\rangle\langle n|\widehat{O}_1|m\rangle e^{-E_m(\tau_{max}-\tau)}e^{-E_n\tau}\ . \tag{1.33}$$

An overall factor with the vacuum energy $e^{-E_0\tau_{max}}$ can be factored out and included in the normalization factor $\mathcal{Z}$. The vacuum energy state $e^{-E_0\tau}$ and $e^{E_0\tau}$ can be canceled between the two exponentials. This can be done such that we are only considering energy differences from the vacuum, as this is the energy which is observable in real world experiments. For ease of notation, we will simply set $E_0 = 0$. In the $\tau_{max} \to \infty$ limit, which corresponds to zero temperature, only the $E_m = 0$ term in the sum survives, resulting in,

$$\lim_{\tau_{max}\to\infty}\langle O_2(\tau)O_1(0)\rangle = \sum_n \langle 0|\widehat{O}_2|n\rangle\langle n|\widehat{O}_1|0\rangle e^{-E_n\tau}\ . \tag{1.34}$$

The factor $e^{-E_0\tau_{max}}/\mathcal{Z}$ equals unity in the $\tau_{max} \to \infty$ limit so it does not appear here. $\widehat{O}_1$ and $\widehat{O}_2$ can be chosen to be $\widehat{O}_h^\dagger$ and $\widehat{O}_h$ respectively. These operators create or destroy from the vacuum a state with the quantum numbers of some hadron $h$. The above can now be written as,

$$\lim_{\tau_{max}\to\infty}\langle O_h(\tau)O_h^\dagger(0)\rangle = |\langle h|\widehat{O}_h^\dagger|0\rangle|^2 e^{-E_h\tau} + |\langle h'|\widehat{O}_h^\dagger|0\rangle|^2 e^{-E_{h'}\tau} + \text{higher energy excitations}\ , \tag{1.35}$$

where $E_h$ is the lowest energy state with the quantum numbers $h$ and $E_{h'}$ is the energy of the first excited state. Each successive excited state will fall off more quickly with $\tau$, allowing

extraction of mass of a hadron by measuring at the Euclidean correlator at large values of $\tau$. All sorts of hadronic matter can be studied using this method, including mesons, baryons, and gluonic matter, including glueballs and exotics. For simplicity and as it is most relevant to Ch. 5, we will look just at mesons using the pion for illustration. The pion is psuedoscalar that is composed of a light quark and antiquark, indicating it can be created the operator $O_{\pi_+} = \bar{d}\gamma_5 u$. Technically, this is the state of the charged $\pi_+$ but for simulations without electromagnetism and degenerate up and down quark masses, all three pions are degenerate. A correlator that can be used to extract the pion mass is,

$$C(n_\tau) = \sum_{\vec{x}} \langle \overline{u}\gamma_5 d(\vec{x}, n_\tau)\bar{d}\gamma_5 u(0)\rangle = A_0 \left(e^{-m_\pi a n_\tau} + e^{-m_\pi a(N_\tau - n_\tau)}\right) + \text{higher energy excitations}\,. \tag{1.36}$$

This equation differs from Eq. 1.35 in several ways. $\tau$ has been replaced with $an_\tau$ as space-time is now discretized. A sum over space on each time-slice is included to project out only the zero momentum mode such that the only energy contribution is from the mass of the pion. Lastly, due to finite time extent with periodic boundary conditions, the image pion propagator $e^{-m_\pi a(N_\tau - n_\tau)}$ appears. This can be written compactly using the cosh function,

$$C(n_\tau) = \tilde{A}_0 \cosh(m_{eff}(n_\tau - N_\tau/2))\,. \tag{1.37}$$

The mass of the pion is extracted either by fitting the measurement to Eq. 1.37 or by looking at an effective mass plot, which is generated by solving,

$$\frac{C(n_\tau)}{C(n_\tau + 1)} = \frac{\cosh(m_{eff}(n_\tau - N_\tau/2))}{\cosh(m_{eff}(n_\tau + 1 - N_\tau/2))} \tag{1.38}$$

for $m_{eff}$ at each time slice $n_\tau$ and finding where the value of $m_{eff}$ reaches a stable plateau. An example of the pion correlator and an effective mass can be seen in Fig. 1.3a and 1.3b.

## *1.2 Introduction to chiral symmetry and chiral perturbation field theory*

In this section, we will lay the groundwork for and introduce chiral perturbation field theory ($\chi$PT) such that it may be used in Ch. 2-4. For a more in depth review of $\chi$PT I recommend the lectures Ref. [59], [41], and the textbook Ref. [51].

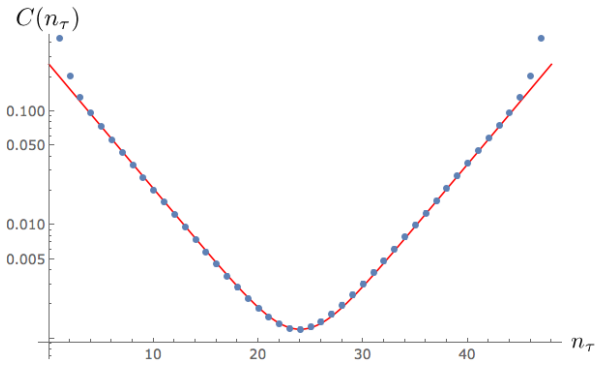


(a) Ensemble averaged pion correlator, with fit to Eq. 1.37.

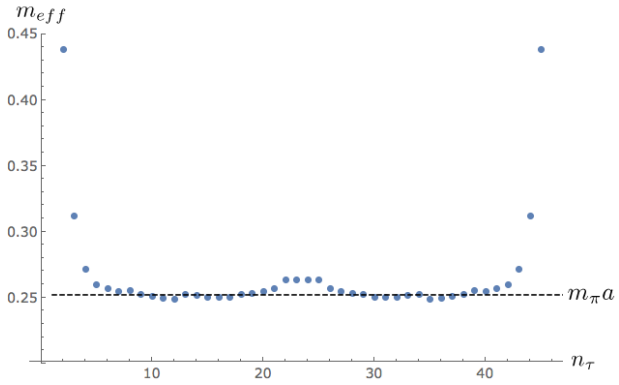


(b) Ensemble averaged pion effective mass, calculated using Eq. 1.38

### *1.2.1 Chiral symmetry*

The massless QCD Lagrangian obeys a $\mathrm{SU}(N_f)_L \times \mathrm{SU}(N_f)_R$ chiral symmetry. As only the up, down and strange quarks are light compared to the natural scale of QCD $\Lambda_{\mathrm{QCD}} \sim 300$ MeV it is only sensible to consider the $N_f = 2$ and $N_f = 3$ theories. The fermionic field, $\psi$ is a vector of quark fields

$$\psi = \begin{pmatrix} u \\ d \\ s \end{pmatrix} \qquad \overline{\psi} = \left(\overline{u}, \overline{d}, \overline{s}\right) \ , \tag{1.39}$$

where $s$ is included in the $N_f = 3$ theory but not the $N_f = 2$ theory. The chiral symmetry of the Lagrangian can be made clear using the chiral projectors $P_{L/R} = (\mathbb{1} \pm \gamma_5)/2$, which have the properties,

$$\begin{aligned} (P_{L,R})^2 = \mathbb{1} \quad P_L P_R = P_R P_L = 0 \\ \gamma_\mu P_{L,R} = P_{R,L} \gamma_\mu \end{aligned} \tag{1.40}$$

and act on fermionic fields as,

$$\begin{aligned} \mathbb{1}\psi = (P_L + P_R)\psi = P_L \psi_L + P_R \psi_R \\ \overline{\psi}\mathbb{1} = \overline{\psi}(P_L + P_R) = \overline{\psi}_R P_L + \overline{\psi}_L P_R. \end{aligned} \tag{1.41}$$

where each left or right-handed fermionic field independently transforms under a left or right handed chiral transformation,

$$\begin{aligned}
\text{Left-handed transformation: } & \psi_L \to U_L \psi_L & \psi_R \to \psi_R \\
& \overline{\psi}_L \to U_L^\dagger \overline{\psi}_L & \overline{\psi}_R \to \overline{\psi}_R \\
\text{Right-handed transformation: } & \psi_L \to \psi_L & \psi_R \to U_R \psi_R \\
& \overline{\psi}_L \to \overline{\psi}_L & \overline{\psi}_R \to U_R^\dagger \overline{\psi}_R \ .
\end{aligned} \tag{1.42}$$

Using these properties, the massless QCD fermionic Lagrangian can be seen to be invariant under a chiral transformation,

$$\begin{aligned}
\overline{\psi} \not{D} \psi &= \overline{\psi}(P_L + P_R) \not{D} (P_L + P_R)\psi \\
&= (\overline{\psi}_R P_L + \overline{\psi}_L P_R) \not{D} (P_L \psi_L + P_R \psi_R) \\
&= \overline{\psi}_R \not{D} \psi_R + \overline{\psi}_L \not{D} \psi_L \\
\text{Left-handed transformation: } &\to \overline{\psi}_R \not{D} \psi_R + \overline{\psi}_L U_L^\dagger \not{D} U_L \psi_L \\
&= \overline{\psi}_R \not{D} \psi_R + \overline{\psi}_L \not{D} \psi_L \\
\text{Right-handed transformation: } &\to \overline{\psi}_R U_R^\dagger \not{D} U_R \psi_R + \overline{\psi}_L \not{D} \psi_L \\
&= \overline{\psi}_R \not{D} \psi_R + \overline{\psi}_L \not{D} \psi_L
\end{aligned} \tag{1.43}$$

where $\not{D} = \gamma_\mu(\partial^\mu + igA^\mu)$. While chiral symmetry is a symmetry of the massless QCD Lagrangian, it is spontaneously broken by the vacuum, which obtains a nonzero quark condensate $\langle \overline{\psi}\psi \rangle \sim \Lambda_{\text{QCD}}^3$. The condensate is not invariant under an arbitrary chiral transformation as its left and right handed components do not separate,

$$\langle \overline{\psi}\psi \rangle = \langle \overline{\psi}_L \psi_R + \overline{\psi}_L \psi_R \rangle \neq 0 \ . \tag{1.44}$$

The left and right handed transformations can be repackaged into a vector transformation, where $U_L = U_R$ and an axial transformation, $U_L = U_R^\dagger$. While not preserving full chiral symmetry, as long as the condensate for each flavor is equal, $\langle \overline{u}u \rangle = \langle \overline{d}d \rangle (= \langle \overline{s}s \rangle)$ a SU($N_f$) vector symmetry is preserved while the axial transformation is not. Goldstone's theorem tells

us that the number of broken generators, in this case the axial generators, is equal to the number of massless Nambu-Goldstone bosons. In the three flavor theory, $\mathrm{SU}(3)_L \times \mathrm{SU}(3)_R \to \mathrm{SU}(3)_V$ with eight mesons— the four kaons, three pions and the eta. In the two flavor theory, $\mathrm{SU}(2)_L \times \mathrm{SU}(2)_R \to \mathrm{SU}(2)_V$ with three mesons, the pions.

In reality, the up, down and strange quarks are not massless and are not degenerate, which explicitly breaks both the axial and the vector transformation. Despite this explicit breaking, spontaneous breaking by a non-vanishing condensate is still considered the primary cause of chiral symmetry breaking due to the approximate $\mathrm{SU}(3)_V$ symmetry which manifests itself in the eight light mesons and the even better $\mathrm{SU}(2)_V$ symmetry manifesting in the pions which are the lightest hadronic states. This is due to the three light quark masses being small relative to the scale of the condensate $m_{u,d,s}/\Lambda_{\mathrm{QCD}} \ll 1$.

### *1.2.2 Chiral perturbation theory*

Chiral perturbation theory ($\chi$PT) is the energy effective field theory that describes QCD at energies below the chiral scale $\Lambda_\chi \sim 1$ GeV, where the light mesons fields are the degrees of freedom. The chiral scale $\Lambda_\chi$ is the mass scale of hadrons made up of the three light quarks which are not psuedo Nambu-Goldsone bosons, such as the rho and the proton. The condensate can be treated as the vacuum expectation value of a dynamical field, $\Sigma(x)$, which is an element of $\mathrm{SU}(3)_V/\mathrm{SU}(2)_V$,

$$\begin{aligned} &\langle\overline{\psi}\psi\rangle \propto \langle U_R^\dagger U_L + U_L^\dagger U_R\rangle = \langle\Sigma\rangle \\ &\Sigma(x) \to U_L \Sigma(x) U_R^\dagger \end{aligned} \tag{1.45}$$

The field parametrizes the light meson fields as,

$$\Sigma(x) = \langle\Sigma\rangle e^{2i\pi^a(x)T^a} \tag{1.46}$$

where $f \sim 92$ MeV (the pion decay constant in the chiral $m_{u,d,s} \to 0$ limit) is a low energy coefficent (LEC). $\pi^a$ are the meson fields and $T^a$ are the Gell-Mann matrices in the three

flavor theory and the Pauli matrices in the two flavor theory,

$$\mathrm{SU}(3)_V: \quad \pi^a T^a = \begin{pmatrix} \frac{\pi^0}{2} + \frac{\eta}{\sqrt{12}} & \frac{\pi^+}{\sqrt{2}} & \frac{K^+}{\sqrt{2}} \\ \frac{\pi^-}{\sqrt{2}} & -\frac{\pi^0}{2} + \frac{\eta}{\sqrt{12}} & \frac{K^0}{\sqrt{2}} \\ \frac{K^-}{\sqrt{2}} & \frac{\overline{K^0}}{\sqrt{2}} & -\frac{2\eta}{\sqrt{12}} \end{pmatrix} \tag{1.47}$$

$$\mathrm{SU}(2)_V: \quad \pi^a T^a = \begin{pmatrix} \frac{\pi^0}{2} & \frac{\pi^+}{\sqrt{2}} \\ \frac{\pi^-}{\sqrt{2}} & -\frac{\pi^0}{2} \end{pmatrix}$$

From here, we follow the normal strategy of an effective field theory, writing down the most general Lagrangian by including all non-trivial terms that obey the symmetries of this theory, starting with the lowest dimension terms. At leading order (LO), this is simply the kinetic term,

$$\mathcal{L}_\chi = \frac{f^2}{4} \operatorname{tr}\left[\partial_\mu \Sigma \partial_\mu \Sigma^\dagger\right] \ . \tag{1.48}$$

As the quarks are not massless, the quark mass matrix must be included, although it does not respect chiral symmetry. To get around this, we use the spurion trick, where the mass matrix, $M$, is treated as though it transforms like $\Sigma$, with the actual value of $M$ only substituted when evaluating,

$$\begin{aligned} M &\to U_L M U_R^\dagger \\ M &= \begin{pmatrix} m_u & 0 & 0 \\ 0 & m_d & 0 \\ 0 & 0 & m_s \end{pmatrix} \ , \end{aligned} \tag{1.49}$$

where the third row and column is deleted in the two flavor theory. The mass term enters the LO Lagrangian with a new LEC $B_0$,

$$\mathcal{L}_\chi = \frac{f^2}{4} \operatorname{tr}\left[\partial_\mu \Sigma \partial_\mu \Sigma^\dagger - 2B_0(M\Sigma^\dagger + \Sigma M^\dagger)\right] \ . \tag{1.50}$$

Expanding the above equation in powers of $\pi^a$, the meson masses are found to be,

$$m^2_{q_f, q_{f'}} = B_0(m_f + m_{f'}), \qquad f \neq f', \qquad f = \{u, d, s\} \tag{1.51}$$

with the exception of the $\pi^0$ and $\eta$ in the three flavor theory that mix, resulting in a corrections to the masses that go as $B_0(m_u - m_d)^2/m_s$.

For greater accuracy, next to leading order (NLO) corrections can be included as well by including higher dimension terms in the Lagrangian. To determine the next terms that must be included, a power counting must be established. The leading Lagrangian scales as $\mathcal{O}(p^2 \sim B_0 m_f)$, which is small compared to the natural scale of $\chi$PT $\Lambda_\chi^2 = (4\pi f)^2$. The NLO Lagrangian will include terms which are suppressed by an additional factor of $\Lambda_\chi^2$,

$$\text{LO:}\frac{p^2}{\Lambda_\chi^2} \sim \frac{B_0 m_f}{\Lambda_\chi^2} \qquad \text{NLO:}\frac{p^4}{\Lambda_\chi^4} \sim \frac{p^2 B_0 m_f}{\Lambda_\chi^4} \sim \frac{(B_0 m_f)^2}{\Lambda_\chi^4} \ . \tag{1.52}$$

In the three flavor theory, there are 10 independent terms, but here we show only the 8 which do not include external sources,

$$\begin{aligned}\mathcal{L}_{\chi,NLO} = &- L_1 \operatorname{tr}\left[\partial_\mu \Sigma \partial_\mu \Sigma^\dagger\right]^2 + L_2 \operatorname{tr}\left[\partial_\mu \Sigma \partial_\nu \Sigma^\dagger\right] \operatorname{tr}\left[\partial_\mu \Sigma \partial_\nu \Sigma^\dagger\right] \qquad (1.53)\\ &+ L_3 \operatorname{tr}\left[\partial_\mu \Sigma \partial_\mu \Sigma^\dagger \partial_\nu \Sigma \partial_\nu \Sigma^\dagger\right] + L_4 \operatorname{tr}\left[\partial_\mu \Sigma \partial_\mu \Sigma^\dagger\right] \operatorname{tr}\left[2B_0(M\Sigma^\dagger + \Sigma M^\dagger)\right]\\ &+ L_5 \operatorname{tr}\left[\partial_\mu \Sigma \partial_\mu \Sigma^\dagger 2B_0(M\Sigma^\dagger + \Sigma M^\dagger)\right] - L_6 \left(\operatorname{tr}\left[2B_0(M\Sigma^\dagger + \Sigma M^\dagger)\right]\right)^2\\ &- L_7 \left(\operatorname{tr}\left[2B_0(M\Sigma^\dagger - \Sigma M^\dagger)\right]\right)^2 - L_8 \operatorname{tr}\left[4B_0^2\left(M\Sigma^\dagger M\Sigma^\dagger + \Sigma M^\dagger \Sigma M^\dagger\right)\right] \ . \qquad (1.54)\end{aligned}$$

In the two flavor theory, by exploiting identities among traces of SU(2) matrices, the NLO Lagrangian can be further reduced to 7 independent terms. The LEC for each of these terms, the $L_i$'s, are called the Gasser-Leutwyler coefficents. These coefficents are fundamental parameters of QCD, some of which can be measured experimentally, while others can be calculated on the lattice, exploiting the fact that lattice simulations are not restricted to a single set of quark masses.

# Chapter 2

# PHASE DIAGRAM OF NON-DEGENERATE TWISTED MASS FERMIONS [1]

## *2.1 Introduction*

It has long been known, in the case of three light quarks, that there is a transition to a CP-violating phase for non-degenerate quarks when one of the quark masses becomes sufficiently negative [19]. For example, using leading order (LO) SU(3) chiral perturbation theory ($\chi$PT), and fixing $m_d$ and $m_s$, the transition occurs when $m_u = -m_d m_s/(m_d + m_s)$ [16]. The neutral pion becomes massless on the transition line, and within the new phase the chiral order parameter, $\langle\Sigma\rangle$, becomes complex. For physical QCD this is mostly a curiosity, since increasingly accurate determinations of the quark masses indicate clearly that all are positive relative to one another [11, 4]. Thus physical QCD, despite the non-degeneracy of the up and down quarks, lies away from the critical line.

For lattice QCD (LQCD), however, the situation is less clear. The position of the transition can be shifted closer to the physical point by discretization effects. Indeed, it is well known that, with degenerate Wilson-like fermions,[2] discretization effects can lead to the appearance of a new phase—the Aoki phase—in which isospin is spontaneously broken and $\langle\Sigma\rangle$ is complex [3, 56]. In addition, advances in simulations now allow calculations to be done at the physical light-quark masses, including, very recently, the physical non-degeneracy between up and down quarks [14]. It is thus natural to ask how, in LQCD with non-degenerate quarks, discretization effects change the position and nature of the CP-violating phase. This question is particularly acute in the case of twisted-mass fermions, where additional symme-

[1] This chapter is adapted with minimal changes from Ref. [38]

[2] "Wilson-like" indicates that the analysis holds for both Wilson fermions and various improvements thereof, in particular for non-perturbatively $\mathcal{O}(a)$-improved Wilson fermions.

try breaking is explicitly included.

In this chapter we address this question for Wilson-like and twisted-mass lattice fermions. We do so using $\chi$PT, specifically the versions of $\chi$PT in which the effects of discretization have been included. Our work also allows us to address a related issue: In what way is the CP-violating phase of the continuum theory related to the Aoki phase of the lattice theory?[3]

Since twisted-mass QCD is only defined for even numbers of fermion flavors [28], a necessary step for our work is to rephrase the continuum SU(3) $\chi$PT analysis of Ref. [16] in the two-flavor theory obtained by integrating out the strange quark. This requires that the contributions of one of the next-to-leading order (NLO) low-energy coefficients ($\ell_7$) be treated as parametrically larger than the others. Thus we are led to a somewhat non-standard power-counting, but one which reproduces the SU(3) phase diagram, including the CP-violating phase, within SU(2) $\chi$PT. This approach has been used before along the line $m_u = -m_d$ [61]; here we extend the analysis to arbitrary mass splitting. Similar work has also been done recently in the context of a effective theory including the $\eta$ meson [5].

The organization of this article is as follows. In Sec. 2.2 we briefly recall the results for the phase structure and pion masses at LO in SU(2) and SU(3) $\chi$PT, and show how they differ. Section 2.3 describes the matching of SU(3) and SU(2) $\chi$PT. In Sec. 2.4, we recall briefly how discretization effects are incorporated in $\chi$PT for degenerate Wilson-like fermions, and the resulting phase structure. We then present our first new results: the phase diagram including both discretization effects and non-degeneracy. In Sec. 2.5 we move onto twisted-mass fermions, focusing first on the phase diagram and pion masses in the case of maximal twist, where most simulations have been done because of the property of automatic $\mathcal{O}(a)$ improvement [28]. It is nevertheless interesting to understand how the results with untwisted and maximally twisted fermions are connected, and so, in Sec. 2.6, we discuss the phase diagram for general twist.

Up to this stage, our analysis is done using the LO terms due to the average quark

[3]This issue has been raised previously by Mike Creutz and his conjectured answer is confirmed by the present analysis [18].

mass, discretization effects and non-degenerate quark masses. To understand how robust the results are we consider, in Sec. 2.7, the impact of including the next higher order terms in our power counting. Some conclusions are collected in Section 2.8.

### *2.2 Continuum Vacuum Structure at leading order in $\chi$PT*

In this section we review the vacuum structure predicted by LO $\chi$PT for both two and three light flavors. The LO chiral Lagrangian in Euclidean space-time is, for any number of light flavors,

$$\mathcal{L}_\chi = \frac{f^2}{4}\,\mathrm{tr}\left[\partial_\mu\Sigma\partial_\mu\Sigma^\dagger - (\chi\Sigma^\dagger + \Sigma\chi^\dagger)\right]\,, \tag{2.1}$$

where $\Sigma \in SU(N_f)$ and $\chi = 2B_0M$ (with $M$ the mass matrix), while $f \sim 92$ MeV and $B_0$ are low-energy constants (LECs).

For two light flavors the chiral order parameter can be parametrized as $\langle\Sigma\rangle = \exp(i\theta\hat{n}\cdot\vec{\tau})$. Although the mass matrix $M = \mathrm{diag}(m_u, m_d)$ has both singlet and triplet components, the leading order potential depends only on the former

$$\mathcal{V}_{SU(2),\,LO} = -\frac{f^2}{4}\,\mathrm{tr}\left[\chi\Sigma^\dagger + \Sigma\chi^\dagger\right] = -\frac{f^2}{2}\cos\theta\,\mathrm{tr}[\chi] \equiv -f^2\cos\theta\,\chi_\ell\,. \tag{2.2}$$

In the last step we have defined the convenient quantity $\chi_\ell = B_0(m_u + m_d)$. The potential is minimized at $\theta = 0$ if $\chi_\ell > 0$ and at $\theta = \pi$ if $\chi_\ell < 0$, resulting in the phase diagram sketched in Fig. 2.1. In terms of the behavior of the condensate, this is a first-order phase transition at which the condensate flips sign. This characterization is somewhat misleading, however, because the two sides of the transition are related by a non-anomalous flavor rotation. Such a transformation can change $M \to -M$ and $\Sigma \to -\Sigma$, while leaving physics unchanged. Thus by adding an extra dimension to the phase diagram (as we will do later) one finds that the two sides are connected.

Expanding the potential about its minimum, using $\Sigma = \langle\Sigma\rangle\exp(i\vec{\pi}\cdot\vec{\tau}/f)$ we find the standard LO result for the pion masses, $m_\pi^2 = |\chi_\ell|$. These thus vanish along the phase transition line. That they vanish at the origin follows from Goldstone's theorem due to the spontaneous breaking of the exact axial symmetry. That they vanish away from the origin

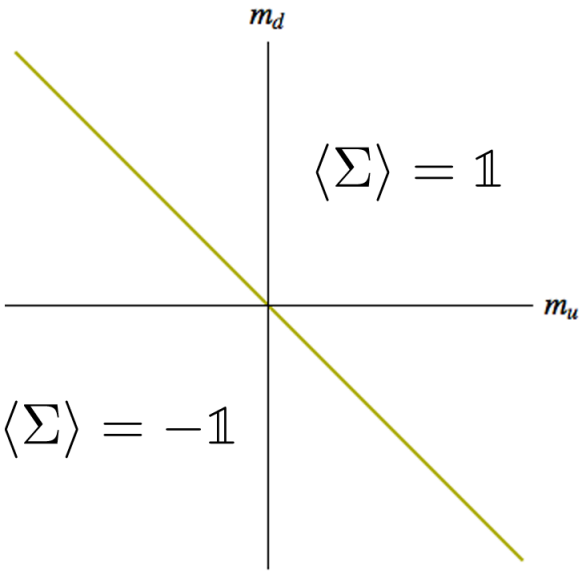


Figure 2.1: Phase diagram at lowest order in SU(2) $\chi$PT.

along the transition line is not expected from symmetry arguments, and indeed holds, as we will see, only at LO in $\chi$PT.

The phase diagram of the three-flavor theory has a more interesting structure, as elucidated most extensively by Creutz [16]. Since $m_s \gg m_u, m_d$ in nature, it is natural to hold $m_s$ fixed and vary the other two quark masses. The resulting phase diagram at LO is sketched in Fig. 2.2. The "normal" region, in which $\langle\Sigma\rangle = \mathbb{1}$, ends at a transition line along which $m_{\pi^0}$ vanishes. This occurs (for fixed $m_s > 0$) when one of the other masses, say $m_u$, becomes sufficiently negative. The explicit expression for the neutral pion mass in this phase is

$$m^2_{\pi^0\,SU(3)} = \frac{2}{3}B_0\left(m_u + m_d + m_s - \sqrt{m_u^2 + m_d^2 + m_s^2 - m_u m_d - m_u m_s - m_d m_s}\right) , \quad (2.3)$$

which vanishes when $m_u = -m_d m_s/(m_d + m_s)$. The charged pions remain massive throughout the normal phase except at the origin.

Moving outside the normal phase one enters a CP-violating phase in which the condensate

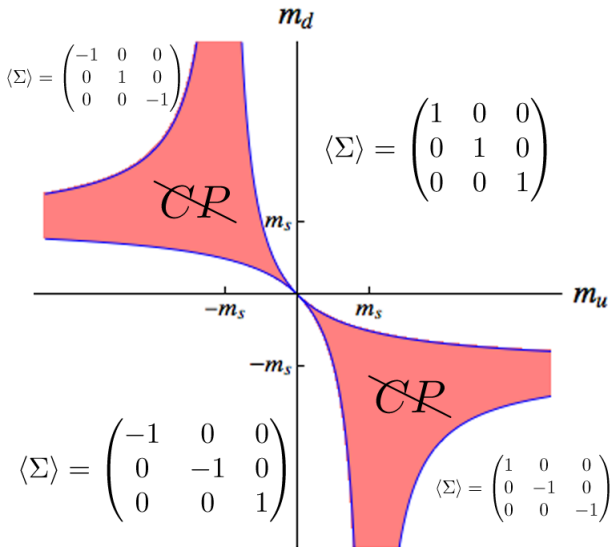


Figure 2.2: Phase diagram at lowest order in SU(3) $\chi$PT with fixed strange quark mass. Equations for the positions of phase transition lines are given in the text.

is complex. The explicit form is

$$\langle\Sigma\rangle = \begin{pmatrix} \exp i\phi & 0 & 0 \\ 0 & \exp i\psi & 0 \\ 0 & 0 & \exp -i(\phi+\psi) \end{pmatrix} \tag{2.4}$$

where the phases satisfy

$$m_u \sin\phi = m_d \sin\psi = -m_s \sin(\phi+\psi)\,. \tag{2.5}$$

In this case there is a genuine phase transition at the boundary. It is of second order: $\langle\Sigma\rangle$ is continuous, and a single pion becomes massless.

The phase diagram is symmetric under both $m_u \leftrightarrow m_d$ interchange and inversion through the origin (with $m_s$ fixed). Inversion is brought about by a non-anomalous axial isospin transformation, which also changes the condensate as shown in Fig. 2.2. We note that the CP-violating region is of finite width.[4] Specifically, as one moves away from the origin along

[4]The theory along the $m_u = -m_d$ diagonal is identical to that with $m_u = m_d$ at $\theta_{\rm QCD} = \pi$, and has

the $m_u = -m_d$ diagonal, the width of this region grows proportionally to $(m_u - m_d)^2/m_s$.

As the figure shows, there are additional phase boundaries in the second and fourth quadrants. These occur, however, when $|m_u|, |m_d| > |m_s|$, and thus lie far from the region of physical interest. In the rest of our analysis, we consider only the region in which $|m_u|, |m_d| \ll |m_s|$, and thus zoom in on the vicinity of the origin in Fig. 2.2.

### *2.3 Matching SU(2) and SU(3) χPT for non-degenerate quarks*

If we choose the quark masses to satisfy $|m_u|, |m_d| \ll |m_s| \ll \Lambda_{\rm QCD}$, then the properties of pions can be simultaneously described by both SU(2) and SU(3) $\chi$PT, and the predictions of the two theories must agree. The results of the previous section show that this is not the case if we work to LO in both theories—the CP-violating phase is absent in SU(2) $\chi$PT. The discrepancy is resolved by noting that the CP-violating phase has a width proportional to $(m_u - m_d)^2$, indicating that it arises at NLO in SU(2) $\chi$PT. In this section we recall how the two theories are matched, and show how the CP-violating phase can then be obtained in SU(2) $\chi$PT when including the resulting NLO term.

To do the matching, one considers quantities accessible in both SU(2) and SU(3) theories, namely pion masses and scattering amplitudes. Expanding the LO SU(3) result in powers of $m_{u,d}/m_s$, the leading terms match with the LO SU(2) result, while the first subleading terms match with an NLO SU(2) contribution. The subleading terms in the SU(3) results are in fact proportional to $(m_u - m_d)^2$, because they arise from intermediate $\eta$ propagators and involve two factors of the $\pi^0 - \eta$ mixing amplitude. The only source of such mass dependence at NLO in the SU(2) theory is the $\ell_7$ term in the NLO potential

$$\mathcal{V}_{SU(2)\,NLO} = -\frac{\ell_3}{16}[\mathrm{tr}(\chi^\dagger\Sigma + \Sigma^\dagger\chi)]^2 + \frac{\ell_7}{16}[\mathrm{tr}(\chi^\dagger\Sigma - \Sigma^\dagger\chi)]^2\,. \tag{2.6}$$

Writing $\chi$ as

$$\chi = \chi_\ell \mathbb{1} + \epsilon\tau_3\,, \quad \text{with} \quad \epsilon = B_0(m_u - m_d)\,, \tag{2.7}$$

been discussed extensively in the literature. In particular, a $\chi$PT analysis of this theory has been given in Ref. [61].

we see that only the $\epsilon$ part contributes to the $\ell_7$ term. Thus this term leads to contributions proportional to $(m_u - m_d)^2$. Other NLO contributions (i.e. those proportional to different NLO LECs or coming from loops) do not have this mass dependence.

The simplest quantity with which to do the matching is the neutral pion mass, and this was used to determine the value of $\ell_7$ in Ref. [31]. The LO SU(3) result [given in Eq. (2.3) above] expands to

$$m^2_{\pi^0 SU(3)\,LO} = \chi_\ell - \frac{\epsilon^2}{4B_0 m_s} + \mathcal{O}\left(\frac{\epsilon^2 m_{u,d}}{m_s^2}\right) . \tag{2.8}$$

The SU(2) result at NLO is

$$m^2_{\pi^0 SU(2)\,NLO} = \chi_\ell - \frac{2\ell_7 \epsilon^2}{f^2} + \mathcal{O}\left(\frac{\chi_\ell^2}{\Lambda_\chi^2}\right) , \tag{2.9}$$

where $\Lambda_\chi = 4\pi f$ is the chiral scale. The $\chi_\ell^2$ contributions arise from terms in the NLO chiral Lagrangian (including $\ell_3$) as well as from chiral logarithms. Equating these two results one finds [31]

$$\ell_7 = \frac{f^2}{8B_0 m_s} . \tag{2.10}$$

One can show that with this value for $\ell_7$, contributions to all pion $n$-point amplitudes proportional to $\epsilon^2/m_s$ agree in the two theories.

We stress that in this matching we are not taking into account "standard" NLO contributions, i.e. those suppressed relative to LO results by factors of $m_{u,d}/\Lambda_{\rm QCD} \sim (m_\pi/\Lambda_\chi)^2$ (up to logarithms). Such contributions arise in both SU(3) and SU(2) $\chi$PT and must be included in a full NLO matching. This is not necessary for our purposes since such terms lead to small isospin-conserving corrections to the vacuum structure and pion masses—they do not introduce qualitatively new effects. By contrast, the $\epsilon^2$ terms that we keep lead to isospin breaking, and are the leading order contributions which do so. Indeed, for this reason $\ell_7$ is not renormalized at this order, since, as already noted, one-loop chiral logarithms do not contain a term proportional to $\epsilon^2$. Thus it is consistent to work with the classical potential, rather than the one-loop effective potential. This is not the case for other LECs such as $\ell_3$, which are renormalized and thus scale-dependent [31].

We can formalize this by noting that standard NLO contributions are parametrically smaller than the terms we keep by a factor of $m_s/\Lambda_{\rm QCD}$. This allows the development of a consistent power-counting scheme in which the $\epsilon^2$ terms are larger than generic $m^2$ contributions.[5] We discuss this in the following section. To be consistent we should also account for NLO contributions in SU(3) $\chi$PT of size $m_s/\Lambda_{\rm QCD}$ relative to LO terms. These, however, lead only to a renormalization of the SU(2) constants $f$ and $B_0$ relative to their SU(3) counterparts. Since we work henceforth entirely in the SU(2) theory, we choose to leave this renormalization implicit.

We now show that the inclusion of the $\ell_7$ term leads to the same phase diagram as found in the LO SU(3) analysis. Given the matching result Eq. (3.4), we always assume $\ell_7 > 0$ in the following. Using $\langle\Sigma\rangle = \exp(i\theta\hat{n}\cdot\vec{\tau})$, the potential becomes

$$\mathcal{V}_{SU(2)} = -f^2\left(\chi_\ell\cos\theta + c_\ell\epsilon^2 n_3^2\sin^2\theta\right)\,, \tag{2.11}$$

where $c_\ell = \ell_7/f^2$. Since $\ell_7 > 0$, the potential is always minimized by choosing $|n_3| = 1$. Since $n_3 = 1$ and $n_3 = -1$ are related by changing the sign of $\theta$, we can, without loss of generality, set $n_3 = 1$. The resulting potential is stationary with respect to $\theta$ at the "normal" values $\theta = 0$ and $\pi$, and in addition at

$$\cos\theta = \frac{\chi_\ell}{2c_\ell\epsilon^2}\,. \tag{2.12}$$

This new stationary value always leads to the global minimum of the potential where it is valid, i.e. when $|\cos\theta| \le 1$. Thus, for fixed $\epsilon$, there is a new phase for $-2c_\ell\epsilon^2 \le \chi_\ell \le 2c_\ell\epsilon^2$, within which $\langle\Sigma\rangle$ is complex and CP is violated. Although $\cos\theta$ is fixed, the sign of $\theta$ is not, with the two possible vacua begin related by a CP transformation. This phase matches continuously onto the normal phases with $\cos\theta = \pm 1$ at its boundaries. Thus the phase transition is of second order.

[5] The numerical basis for this power-counting is not very strong. For example, $\ell_7$ and $\ell_3(\mu)$ are comparable in size for reasonable values of the scale $\mu$. Thus the numerical size of the standard NLO corrections we are dropping may be comparable to those proportional to $\epsilon^2$ that we are keeping. The key point, however, is that we are interested in qualitatively new effects, rather than a precise quantitative description.

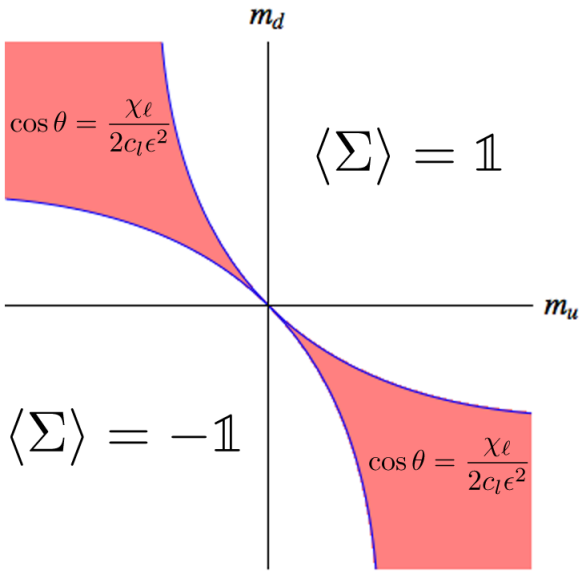


Figure 2.3: Phase diagram from SU(2) $\chi$PT including $\ell_7$ term with $\ell_7 > 0$. Equations for the positions of phase transition lines are given in the text.

The resulting phase diagram is sketched in Fig. 2.3. This is not only qualitatively similar to the central portion of the LO SU(3) phase diagram, Fig. 2.2, but is in fact in complete quantitative agreement at the appropriate order. For example, expanding the SU(3) result for the phase boundary, $m_u = -m_d/(1 + m_d/m_s)$, in powers of $m_{u,d}/m_s$, and keeping only the leading non-trivial term, one finds that the boundary occurs at $\chi_\ell = \epsilon^2/(4B_0 m_s)$. This agrees with the SU(2) result $\chi_\ell = 2\ell_7\epsilon^2/f^2$ using the matching condition (3.4). We have also checked that the pion masses agree throughout the phase plane. We do not quote results for pion masses here, since they are included in the more general analysis presented below.

The fact that the CP-violating phase can be reproduced within SU(2) $\chi$PT was first explained by Smilga [61]. His work considered only the case $m_u = -m_d$, which, as noted above, is the same as $m_u = m_d$ with $\theta_{\rm QCD} = \pi$. The analysis presented here gives the (very simple) generalization to arbitrary non-degenerate quark masses. There is also a close relation between our analysis and the recent work of Aoki and Creutz [5]. These authors do not use $\chi$PT *per se*, but rather an effective theory containing both pions and the $\eta$ meson. If

the $\eta$ were integrated out then their theory would reduce to that we consider here, including the $\ell_7$ term, plus small corrections. We think, however, that it is preferable to work in a strict effective theory framework, in which only the light particles are kept as dynamical degrees of freedom.

### *2.4 Including discretization effects for Wilson-like fermions*

In this section we recall how lattice artifacts can be incorporated into $\chi$PT, and study their impact on the phase structure described above at leading non-trivial order. We do this for untwisted Wilson-like fermions—twist will be considered in the following sections. The method leads to the chiral effective theory describing lattice simulations close to the continuum limit. We begin by recalling the analysis for degenerate quarks and then add in non-degeneracy. We work entirely in the two-flavor theory obtained after the strange quark (and the charm quark too, if present) has been integrated out. For untwisted Wilson-like fermions (unlike for twisted-mass fermions), the analysis could also be carried out within SU(3) $\chi$PT, but there is no advantage to doing so as the dominant long-distance dynamics lies in the SU(2) sector.

Both quark masses and discretization effects break chiral symmetry, and it is important to understand the relative size of these effects. Our focus here is on state-of-the-art simulations, which have $m_{u,d}$ close to their physical values ($m_u \approx 2.5$ MeV and $m_d \approx 5$ MeV in the $\overline{\text{MS}}$ scheme at $\mu = 2$ GeV), and lattice spacings such that $1/a \approx 3$ GeV. In this case, the relative size of discretization effects is characterized by $a\Lambda_{\text{QCD}} \approx 0.1$ (using $\Lambda_{\text{QCD}} = 300$ MeV), so that

$$a\Lambda_{\text{QCD}}^2 \approx 30\,\text{MeV} \gg m_{u,d} \approx a^2\Lambda_{\text{QCD}}^3 \approx 3\,\text{MeV}\,. \tag{2.13}$$

The appropriate power-counting is thus (in schematic notation) $a^2 \sim m$. This is the Aoki regime, in which competition between discretization and mass effects leads to interesting phase structure [3, 56].

Discretization effects can be incorporated into $\chi$PT following the method of Ref. [56]. For unimproved (or partially improved) Wilson fermions, the dominant discretization effect

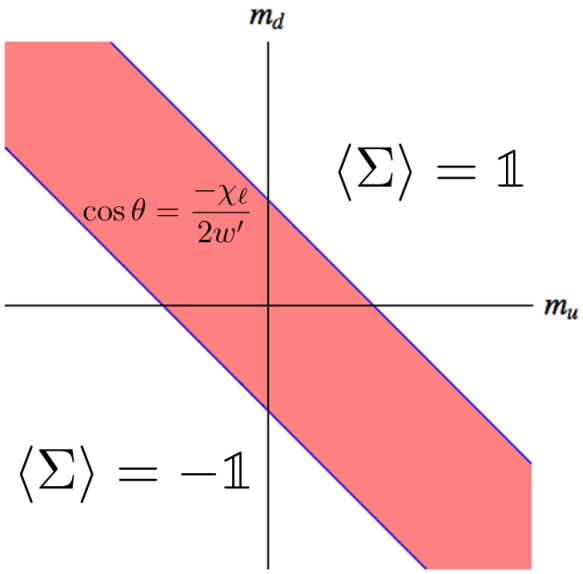


Figure 2.4: Phase diagram in LO SU(2) $\chi$PT including discretization effects with $w' < 0$ (Aoki scenario). Equations for the positions of phase transition lines are given in the text.

is proportional to $a$. In the pion sector, however, this contribution can be absorbed entirely into a common shift in all quark masses [56], and we assume below that this shift has been made. The first non-trivial discretization effect is that proportional to $a^2$. This changes the LO potential to [56]

$$\mathcal{V}_{a^2} = -\frac{f^2}{4}\,\mathrm{tr}(\chi^\dagger\Sigma + \Sigma^\dagger\chi) - W'[\mathrm{tr}(\hat{A}^\dagger\Sigma + \Sigma^\dagger\hat{A})]^2\,. \tag{2.14}$$

Here we are using the notation of Ref. [57], in which $\hat{A} = 2W_0 a\mathbb{1}$ is a spurion field, with dimensions of mass squared, and proportional to the identity matrix in flavor space. $W_0$ and $W'$ are new LECs.

The analysis of the vacuum structure for degenerate quarks was given in Ref. [56]. Since $\mathcal{V}_{a^2}$ is independent of the $\epsilon$, the results are unchanged at LO in the presence of non-degeneracy. To determine the vacuum we must minimize

$$\mathcal{V}_{a^2} = -f^2\left(\chi_\ell\cos\theta + w'\cos^2\theta\right)\,, \tag{2.15}$$

where $w' = 64W'W_0^2a^2/f^2$. For $w' < 0$, the analysis is essentially the same as that for $\mathcal{V}_{SU(2)}$ with $\ell_7 > 0$, as given in the previous section. Stationary points are at $\cos\theta = \pm 1$ and

$$\cos\theta = -\frac{\chi_\ell}{2w'}\,, \tag{2.16}$$

with the latter being the global minimum where valid ($|\cos\theta| \leq 1$). This leads to the phase diagram shown in Fig. 2.4, with an Aoki phase [3] separated from the normal phases by second-order transitions at $|\chi_\ell| = -2w'$. Strictly speaking, the name "Aoki phase" has been applied previously only on the diagonal $m_u = m_d$ axis, but in the present approximation it holds also for non-degenerate quarks. Within the Aoki phase the potential is independent of the direction of the condensate, $\hat{n}$, so that there are two massless Goldstone bosons, the charged pions. Parity and flavor are violated within this phase. With the canonical choice of the direction of the condensate, $\hat{n} = \hat{z}$, CP is also violated.

For $w' > 0$, the global minimum lies at $\cos\theta = \text{sign}(\chi_\ell)$, with a first-order transition at $\chi_\ell = 0$. The phase diagram is thus identical to that in the continuum, Fig. 2.1. The only difference is that here the yellow line indicates a genuine first-order transition, since on the lattice there are no symmetries connecting the two sides. This case is referred to as the first-order scenario [56].

We are now ready to combine the effects of non-degeneracy with discretization errors. This requires that we adopt an appropriate power-counting scheme for the relative importance of $\epsilon^2$, $m$ and $a^2$, where $m$ indicates a generic quark mass. Recalling that $\epsilon^2$ terms are enhanced compared to generic $m^2$ terms we use

$$m \sim a^2 > \epsilon^2 > ma \sim a^3 > a\epsilon^2 > m^2 \sim ma^2 \sim a^4 \ldots . \tag{2.17}$$

This can be thought of as treating $\epsilon \sim a^{1+\delta}$, with $0 < \delta < 1/2$. The utility of this power counting is that allows us to first add the $\epsilon^2$ term to those proportional to $m$ and $a^2$, and then consider terms of order $ma \sim a^3$ at a later stage (in Sec. 2.7 below). Indeed, we could, for the purposes of this section, set $\delta = 0$, and treat the $\epsilon^2$ term as of LO. We do not do so, however, since this would require us to later treat $a\epsilon^2$ terms as of the same size as those

proportional to $ma \sim a^3$. Nevertheless, we will loosely describe the inclusion of $m$, $a^2$ and $\epsilon^2$ terms as constituting our LO analysis, while treating the $ma \sim a^3$ terms as being of NLO. Terms of yet higher order will not be considered.

With the power counting in hand, we can extend the inclusion of discretization errors into $\chi$PT to incorporate the effects of non-degeneracy. This leads to the appearance of new operators in the Symanzik effective Lagrangian, and thus, potentially, to new terms in the chiral Lagrangian. The constraints on additional operators in the Symanzik Lagrangian in the presence of non-degeneracy were worked out in Ref. [65]. Using their results within our power-counting scheme, we find that the lowest order new operator is $\sim a\epsilon^2\bar{\psi}\psi$. This is, however, of higher order than we consider here.[6] All other operators are of yet higher order. Thus, at the order we work, non-degeneracy only enters our calculation through the continuum $\ell_7$ term. The LO potential thus becomes

$$\mathcal{V}_{a^2,\ell_7} = -\frac{f^2}{4}\,\mathrm{tr}(\chi^\dagger\Sigma + \Sigma^\dagger\chi) - W'[\mathrm{tr}(A^\dagger\Sigma + \Sigma^\dagger A)]^2 + \frac{\ell_7}{16}[\mathrm{tr}(\chi^\dagger\Sigma - \Sigma^\dagger\chi)]^2\,. \tag{2.18}$$

We stress that it is self-consistent to determine the vacuum structure and pion masses from a tree-level analysis of $\mathcal{V}_{a^2,\ell_7}$ since loop effects only come in at $\mathcal{O}(m^2, ma^2, a^4)$.

In terms of the parameters of $\langle\Sigma\rangle$, the potential is now given by

$$-\frac{\mathcal{V}_{a^2,\ell_7}}{f^2} = \chi_\ell\cos\theta + c_\ell\epsilon^2 n_3^2\sin^2\theta + w'\cos^2\theta\,. \tag{2.19}$$

As before, we can set $n_3 = 1$ without loss of generality. The stationary points are at $\cos\theta = \pm 1$ and

$$\cos\theta = \frac{\chi_\ell}{2(c_\ell\epsilon^2 - w')}\,. \tag{2.20}$$

The latter minimizes the potential if $c_\ell\epsilon^2 - w' > 0$ and is valid for $|\cos\theta| \leq 1$. This results in the phase diagrams of Figs. 2.5a and 2.5b for $w' < 0$ and $w' > 0$, respectively. In the former case, corresponding to the Aoki phase for degenerate quarks, the second-order transition

[6] Furthermore, when mapped to the chiral Lagrangian, it leads to contributions which can be absorbed by making the untwisted mass $m$ have a weak dependence on $\epsilon$. Thus it does not lead to new phases, but only to a small distortion of the phase diagram.

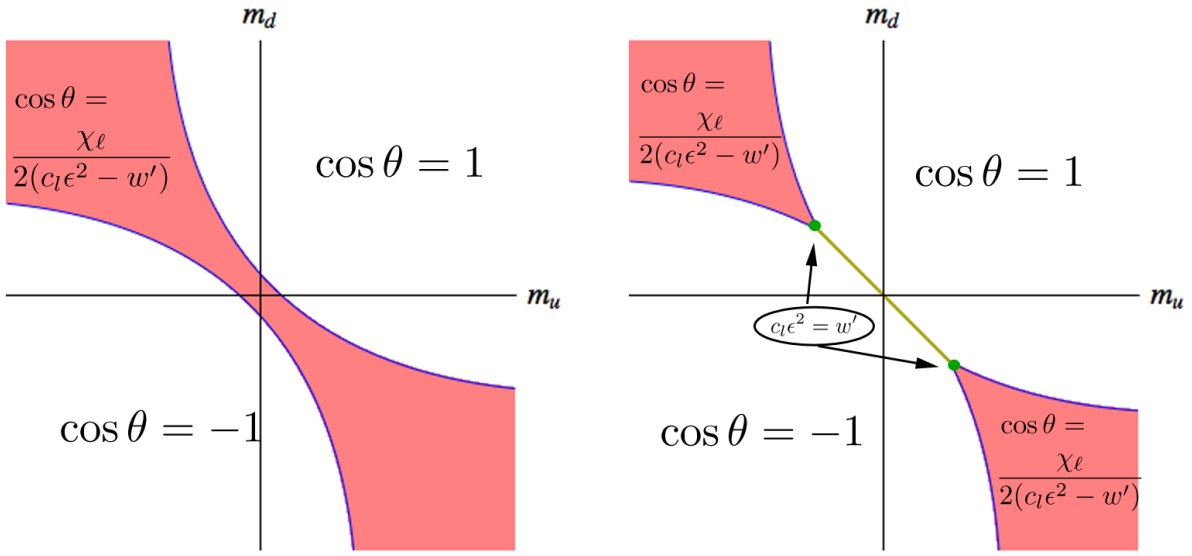


(a) Aoki scenario ($w' < 0$). (b) First-order scenario ($w' > 0$).

Figure 2.5: Phase diagrams including effects of both discretization and non-degeneracy. Blue (yellow) lines indicate second (first) order transitions. Equations for the positions of phase transition lines are given in the text.

lines lie at

$$\chi_\ell = \pm 2(c_\ell \epsilon^2 - w') \,. \tag{2.21}$$

Thus the width of the phase grows as $|\epsilon|$ increases. Furthermore, comparing to Fig. 2.4, we see that the continuum CP-violating phase and the Aoki phase are continuously connected.[7] The only subtlety in this connection is that the condensate definitely points in the $n_3$ direction for $\epsilon \neq 0$ (i.e. the direction picked out by the non-degenerate part of the mass term), whereas for $\epsilon = 0$ the direction is arbitrary.

In the first-order scenario, Fig. 2.5b, the first-order transition along the $m_u = -m_d$ line weakens as $|\epsilon|$ increases, until, at $c_\ell \epsilon^2 = w'$, the CP-violating phase appears. The second-order transition lines are then given by $|\chi_\ell| = 2(c_\ell \epsilon^2 - w')$, i.e. by the same equation as in

[7] This result is in agreement with Creutz' conjecture [18].

the Aoki scenario.

We next calculate the pion masses throughout the phase plane, expanding about the vacuum as

$$\Sigma = \exp(i\theta\tau_3)\exp(i\vec{\pi}\cdot\vec{\tau}/f)\,. \tag{2.22}$$

Outside the CP-violating phase, we find

$$m_{\pi^0}^2 = |\chi_\ell| - 2(c_\ell\epsilon^2 - w')\,, \tag{2.23}$$

$$m_{\pi^\pm}^2 = m_{\pi^0}^2 + 2c_\ell\epsilon^2\,. \tag{2.24}$$

while within the CP-violating phase we have

$$m_{\pi^0}^2 = 2(c_\ell\epsilon^2 - w')\sin^2\theta \tag{2.25}$$

$$m_{\pi^\pm}^2 = 2c_\ell\epsilon^2\,, \tag{2.26}$$

where $\theta$ is given in Eq. (2.20). These results are plotted versus $\chi_\ell$ for various characteristic choices of $\epsilon$ and $w'$ in Fig. 2.6.

Figures 2.6a and b show the continuum results for degenerate and non-degenerate masses, respectively. The neutral pion mass vanishes along the second-order transition line, as expected. The full degeneracy at $\chi_\ell = 0$ is due to the fact that the theory regains flavor symmetry (with $\theta_{\rm QCD} = \pi$) at this point. A characteristic feature of the spectrum at this order is that the charged pion mass is independent of $\chi_\ell$ within the CP-violating phase. This holds also when discretization errors are included.

Figures 2.6c and d show the spectrum for degenerate quarks with discretization errors included, respectively for the Aoki and first-order scenarios, reproducing the results of Ref. [56].

Our new results are those of Figs. 2.6e-g, which include the effects of both discretization errors and non-degeneracy. In this case the charged and neutral pion masses differ in general. Figure 2.6e shows the behavior in the Aoki scenario, where $m_{\pi^0}$ vanishes on the phase transition lines, and rises above $m_{\pi^\pm}$ in the central region of the CP-violating phase. There are thus two values of $\chi_\ell$ where all pions are degenerate, but these are accidental degeneracies

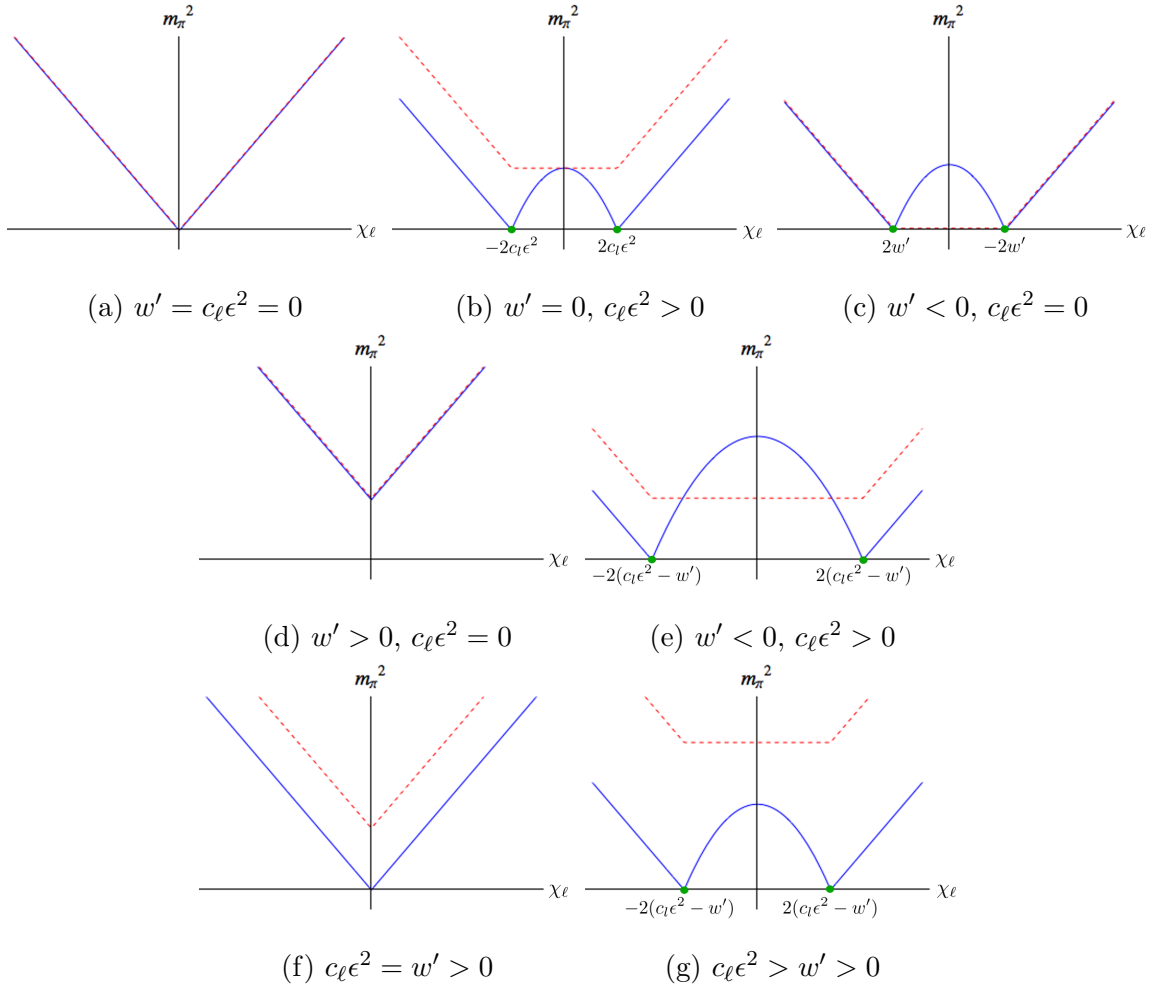


(a) $w' = c_\ell\epsilon^2 = 0$ (b) $w' = 0$, $c_\ell\epsilon^2 > 0$ (c) $w' < 0$, $c_\ell\epsilon^2 = 0$

(d) $w' > 0$, $c_\ell\epsilon^2 = 0$ (e) $w' < 0$, $c_\ell\epsilon^2 > 0$

(f) $c_\ell\epsilon^2 = w' > 0$ (g) $c_\ell\epsilon^2 > w' > 0$

Figure 2.6: Pion masses for untwisted Wilson fermions including the effects of both discretization ($w' \neq 0$) and non-degeneracy ($\epsilon \neq 0$). $m^2_{\pi^0}$ is shown by solid (blue) lines, $m^2_{\pi^\pm}$ by dashed (red) lines. Explicit expressions for the masses are given in the text. Vertical scales differ between the figures.

and not indicative of any symmetry. For the first-order scenario Fig. 2.6f shows the spectrum when $\epsilon$ is chosen so that the plot passes through the end-point of the second-order transition line, while Fig. 2.6g shows what happens as one moves through the CP-violating phase. In this case, there are no degenerate points.

Simulations using Wilson-like fermions at physical masses, including isospin breaking, have recently begun [14]. What is the significance of our results for such simulations? The main issue is whether discretization effects can move the CP-violating phase such that it lies closer to, or even includes, the physical point. Clearly one wants to avoid simulating in this phase, since it has a different vacuum structure from the continuum theory. But even lying close to a second-order transition could lead to algorithmic issues due to critical slowing down. What we have found is that the phase does move closer to the physical point in the Aoki scenario, Fig. 2.5a. In this scenario, the CP-violating phase now includes a region of positive quark masses. On the other hand, for the first-order scenario, discretization effects move the CP-violating phase away from the physical point. A positive aspect of our results is that discretization errors lead only to a overall shift in pion masses (outside of the CP-violating phase), so that the difference $m^2_{\pi^\pm} - m^2_{\pi^0}$ takes its continuum value $2c_\ell\epsilon^2$ in both scenarios.

### *2.5 Twisted-mass fermions at maximal twist*

In this section we extend the previous analysis to twisted-mass fermions [30] at maximal twist. Such fermions have the important practical property of automatic $\mathcal{O}(a)$ improvement [28]. They are being used to simulate QCD with quarks at or near their physical masses [1, 15], and isospin breaking is now being included [23]. The main question we address here is the same as for untwisted fermions: How do discretization effects change the continuum phase structure and pion masses?

In the continuum, twisted mass fermions are obtained by a non-anomalous axial rotation,

$$\mathcal{L}_{\rm QCD} = \overline{\psi}(\not{D}+m_\ell+\epsilon_\ell\tau_3)\psi \to \overline{\psi}(\not{D}+m_\ell e^{i\gamma_5\tau_1\omega}+\epsilon_\ell\tau_3)\psi = \overline{\psi}(\not{D}+m+i\gamma_5\tau_1\mu+\epsilon_\ell\tau_3)\psi\,, \quad (2.27)$$

with $m_\ell = (m_u+m_d)/2$, $\epsilon_\ell = (m_u-m_d)/2$, $m = m_\ell\cos\omega$, $\mu = m_\ell\sin\omega$, and $\omega$ the twist angle. Conventionally, $m$ is called the untwisted (average) mass and $\mu$ the twisted (average) mass. Choosing the twist in a direction orthogonal to $\tau_3$ leaves the $\epsilon_\ell$ term unchanged. In the continuum this is a convenience, but not a necessity. Once one discretizes $\not{D}$ with a Wilson term, however, it is mandatory to twist in a direction orthogonal to $\tau_3$ if one wants to keep the fermion determinant real [29].[8]By convention, this direction is chosen to be $\tau_1$. The rescaled mass matrix that enters $\chi$PT is now

$$\chi = \chi_\ell e^{i\tau_1\omega} + \epsilon\tau_3 = \chi_\ell\cos\omega\mathbb{1} \; + i\chi_\ell\sin\omega\tau_1 + \epsilon\tau_3 = \widehat{m}\mathbb{1} + i\widehat{\mu}\tau_1 + \epsilon\tau_3\,, \quad (2.28)$$

and is no longer hermitian. Here we have defined

$$\widehat{m} \equiv 2B_0 m = \chi_\ell\cos\omega \;\text{ and }\; \widehat{\mu} \equiv 2B_0\mu = \chi_\ell\sin\omega \quad (2.29)$$

following Ref. [57].

---

[8]In Ref. [23], which studies twisted-mass non-degenerate fermions, the twist is chosen in the $\tau_3$ direction. This leads to a complex fermion determinant, which is avoided in practice by perturbing at linear order around the isospin-symmetric theory. Because the twist is in the $\tau_3$ direction, our present results do not apply to these simulations. We will discuss the generalization to $\tau_3$ twist (along with the inclusion of electromagnetism) in Chapter 3 and 4.

To determine the effective chiral theory for twisted-mass lattice QCD the first step is to determine the additional operators in the Symanzik Lagrangian that are induced by twisting. As in the untwisted case, the form of the allowed operators can be obtained from the analysis of Ref. [65], which includes both twist and non-degeneracy. In fact, since $\widehat{\mu}^2$ is smaller than $\epsilon^2$ in our power-counting, the inclusion of twist does not change the result for the untwisted case, namely that the lowest order new operator is $\sim a\epsilon^2$ and of higher order than we are working. Thus at LO the extension $\chi$PT to include twist and discretization errors is accomplished by simply using the twisted $\chi$ of Eq. (2.28) in the potential $\mathcal{V}_{a^2,\ell_7}$ of Eq. (2.18).

Using our standard parametrization of $\langle\Sigma\rangle$ this gives

$$-\frac{\mathcal{V}_{a^2,\ell_7}}{f^2} = \widehat{m}\cos\theta + \widehat{\mu} n_1 \sin\theta + c_\ell \epsilon^2 n_3^2 \sin^2\theta + w' \cos^2\theta\,. \tag{2.30}$$

We focus in this section on the case of maximal twist, $\widehat{m} = 0$, where simple analytic results can be obtained. Even with this simplification, we note that there is competition between terms in three directions in $\Sigma$: the twist direction $n_1$, the non-degeneracy direction $n_3$, and the identity direction ($w'$ term). Thus we can expect a more complicated phase structure than for untwisted Wilson fermions. Furthermore, since non-degenerate twisted-mass quarks completely break the continuous SU(2) flavor symmetry, we expect, in general, that all three pion masses will differ.

We find the phase diagrams shown in Fig. 2.7. Note that we are now plotting the average mass along the vertical axis and the difference horizontally. We do this because $\widehat{\mu}$ and $\epsilon$ are proportional to parameters that enter the twisted-mass lattice action. To compare to the earlier plots, one should rotate those of Fig. 2.7 by 45° in a clockwise direction. We see that, at maximal twist, it is the Aoki scenario which is preferred, in the sense that the CP-violating phase does not move closer to the physical point. Indeed, the phase diagram in this scenario is identical to that in the continuum, Fig. 2.3, with the replacement $\chi_\ell \to \widehat{\mu}$. In the first-order scenario, by contrast, there is an additional phase (colored green in Fig. 2.7b) which brings lattice artifacts closer to the physical point. Thus the relative merits of the two scenarios are interchanged compared to the untwisted case.

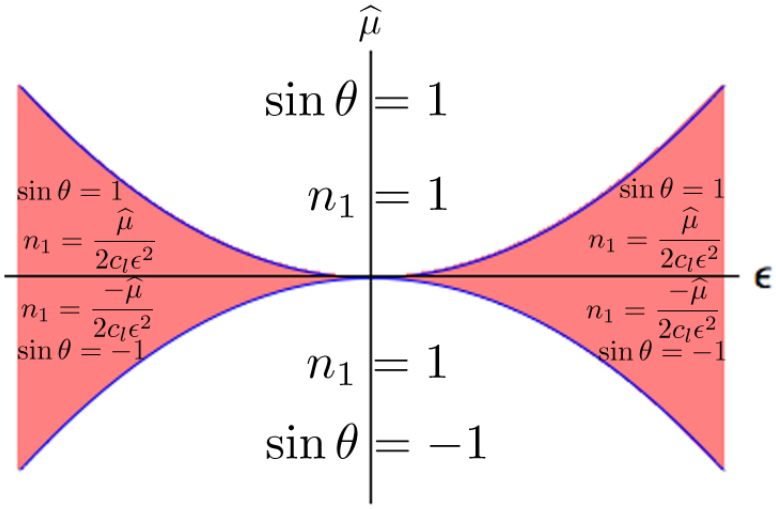


(a) Aoki scenario or continuum ($w' \leq 0$)

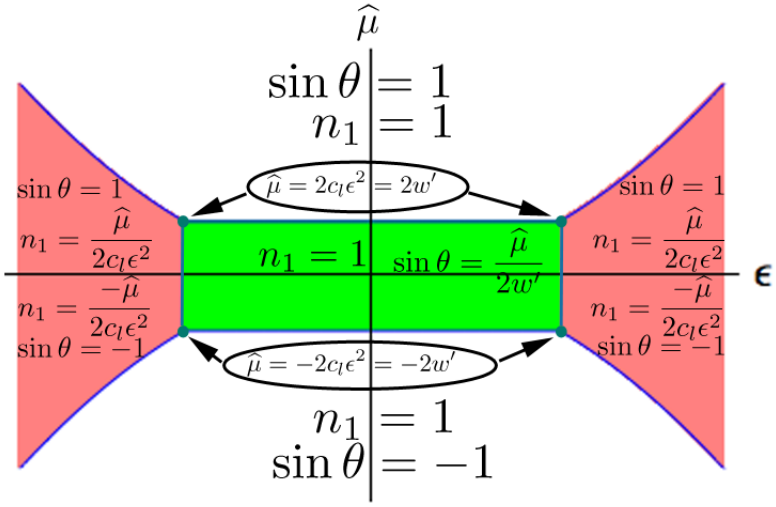


(b) First-order scenario ($w' > 0$)

Figure 2.7: Phase diagrams at maximum twist ($\widehat{m} = 0$).

To understand the phase diagrams we first recall the result for the degenerate case, $\epsilon = 0$, which has been studied in Refs. [45, 52, 57]. These works find, for large $|\widehat{\mu}|$, that the condensate is aligned with the twist, i.e. $n_1 = 1$ and $\sin\theta = \text{sign}(\widehat{\mu})$. This is as in the continuum. In the Aoki scenario ($w' < 0$), this alignment holds for all $\widehat{\mu}$, and there is a

first-order transition at $\widehat{\mu} = 0$ where $\sin\theta$ changes sign. In the first-order scenario ($w' > 0$), there are second-order transitions at the two points $\widehat{\mu} = \pm 2w'$, at which one of the pion masses vanishes. For $|\widehat{\mu}| < 2w'$ the condensate smoothly rotates within the group manifold with $\sin\theta = \widehat{\mu}/(2w')$. These features are reproduced by our results along the vertical axes in Fig. 2.7.

We now explain how these results are generalized to $\epsilon \neq 0$. We first observe that we can set $n_2 = 0$. This is because, for any choice of $n_1$, the $c_\ell$ term in Eq. (2.30) (with $c_\ell > 0$) will be minimized when $n_3^2$ is maximized, i.e. with $n_3^2 = 1 - n_1^2$. Thus there are only two independent variables, $\theta$ and $n_1$. Since $n_1$ satisfies $|n_1| \leq 1$, we parametrize it as $n_1 = \cos\varphi_1$. Since $\langle\Sigma\rangle$ is invariant when $\theta$ and $\vec{n}$ change sign, we need only consider $n_1 \geq 0$, i.e. $0 \leq \varphi_1 \leq \pi/2$. The stationary points are obtained from simultaneously solving

$$\frac{\partial \mathcal{V}_{a^2,\ell_7}}{\partial\theta} \propto \cos\theta \left[\widehat{\mu}\cos\varphi_1 + 2\sin\theta(\sin^2\varphi_1 c_\ell\epsilon^2 - w')\right] = 0\,, \tag{2.31}$$

$$\frac{\partial \mathcal{V}_{a^2,\ell_7}}{\partial\varphi_1} \propto \sin\theta\sin\varphi_1 \left[\widehat{\mu} - 2\sin\theta\cos\varphi_1 c_\ell\epsilon^2\right] = 0\,. \tag{2.32}$$

The solutions are

1. $\cos\theta = 0$ (so that $\sin\theta = \pm 1$) together with $\sin\varphi_1 = 0$ (so that $n_1 = 1$). In these cases $\mathcal{V}_{a^2,\ell_7}/f^2 = \mp\widehat{\mu}$, so that the solution with the lowest energy is that with $\sin\theta = \mathrm{sign}(\widehat{\mu})$, giving $\mathcal{V}_{a^2,\ell_7}/f^2 = -|\widehat{\mu}|$.

2. $\sin\theta = \mathrm{sign}(\widehat{\mu})$ and $n_1 = \cos\varphi_1 = |\widehat{\mu}|/(2c_\ell\epsilon^2)$ so that $\mathcal{V}_{a^2,\ell_7}/f^2 = -\widehat{\mu}^2/(4c_\ell\epsilon^2) - c_\ell\epsilon^2$. This is only valid when $n_1 \leq 1$, i.e. $|\widehat{\mu}| \leq 2c_\ell\epsilon^2$. There are two degenerate solutions, with $n_3 = \pm\sin\varphi_1$.

3. $\sin\theta = \widehat{\mu}/(2w')$ and $\varphi_1 = 0$ (implying $n_1 = 1$) so that $\mathcal{V}_{a^2,\ell_7}/f^2 = -\widehat{\mu}^2/(4w') - w'$. This is only valid when $|\widehat{\mu}| \leq 2w'$. There are two degenerate solutions, with opposite signs of $\cos\theta$.

4. $\cos\theta = \pm 1$ and $\widehat{\mu}n_1 = 0$, so that $\mathcal{V}_{a^2,\ell_7}/f^2 = -w'$. This never has lower energy than the third solution and can be ignored.

The first solution is the continuum one discussed above. The second has lower energy than the first where it is valid, and goes over to the CP-violating phase when $w' = 0$. The third solution is relevant only for $w' > 0$, in which case it has the lowest energy when $c_\ell \epsilon^2 < w'$. The condensate in this phase is independent of $\epsilon$. These considerations lead to the phase diagrams shown in Fig. 2.7. The potential is continuous throughout the phase planes, as is the condensate except at the junction between the central (green colored) phase and the CP-violating phase in Fig. 2.7b. Thus we expect the transitions to be of second order.

We calculate pion masses using the parametrization

$$\Sigma = \exp(i\theta\hat{n}\cdot\vec{\tau}/2)\exp(i\vec{\pi}\cdot\vec{\tau}/f)\exp(i\theta\hat{n}\cdot\vec{\tau}/2)\,, \qquad [\langle\Sigma\rangle = \exp(i\theta\hat{n}\cdot\vec{\tau})]\ . \tag{2.33}$$

Here we are using an axial transformation to rotate from the twisted basis to the physical basis, which ensures, in the continuum, that the pion fields have physical flavors [58]. In the continuum-like phase (uncolored in the figures), which lies in the regions $|\widehat{\mu}| \geq \max(2c_\ell\epsilon^2, 2w')$, we find

$$m_{\pi_1}^2 = |\widehat{\mu}| - 2w'\,, \qquad m_{\pi_2}^2 = |\widehat{\mu}|\,, \qquad m_{\pi_3}^2 = |\widehat{\mu}| - 2c_\ell\epsilon^2\,. \tag{2.34}$$

These results are consistent with those of Ref. [46], where a $\chi$PT calculation in this phase is carried out using the different power-counting $m \gtrsim a$. Various aspects of these results are noteworthy. First, all three masses differ. This is expected since flavor symmetry is completely broken. Second, the charged pions are not mass eigenstates; instead, the eigenstates are $\pi_{1,2}$ and the neutral pion. These two points were also noted in Ref. [46]. Third, one of the pion masses vanishes at each of the phase boundaries: $m_{\pi_3}$ at the boundary with the CP-violating (pink colored) phase, and $m_{\pi_1}$ at the boundary with the central (green colored) phase in the first-order scenario.[9] This is expected since these are continuous transitions at which a $Z_2$ symmetry is broken ($\theta \to -\theta$ for the "green phase" and $n_3 \to -n_3$ for the CP-

[9]In the degenerate case ($\epsilon = 0$) Refs. [45, 52, 57] find that it is $m_{\pi_3}$ which vanishes at $|\widehat{\mu}| = 2w'$, rather than $m_{\pi_1}$. This difference arises because we twist in the $\tau_1$ direction rather than the $\tau_3$ direction used in Refs. [45, 52, 57].

violating phase). Finally, in the first-order scenario, there are four tricritical points at which *both* $m_{\pi_3}$ and $m_{\pi_1}$ vanish. These occur where all three phases meet, i.e. at $|\widehat{\mu}| = 2c_\ell\epsilon^2 = 2w'$.

In the central (green) phase we find

$$m^2_{\pi_1} = 2w' - \frac{\widehat{\mu}^2}{2w'}\,, \qquad m^2_{\pi_2} = 2w'\,, \qquad m^2_{\pi_3} = 2w' - 2c_\ell\epsilon^2\,. \tag{2.35}$$

Thus $m_{\pi_2}$ and $m_{\pi_3}$ are independent of $\widehat{\mu}$ within this phase. These results agree with those in the normal phase, Eq. (2.34), at the boundaries. They also show that $m_{\pi_3}$ vanishes at the borders with the CP-violating (pink) phases ($c_\ell\epsilon^2 = w'$).

In the CP-violating phase there is mixing between $\pi_1$ and $\pi_3$, with the mass eigenvectors being

$$\tilde{\pi}_1 = n_1\pi_1 + n_3\pi_3 \;\text{ and }\; \tilde{\pi}_3 = -n_3\pi_1 + n_1\pi_3\,, \tag{2.36}$$

where we recall that $n_1 = \widehat{\mu}/(2c_\ell\epsilon^2)$ and $n_3 = \sqrt{1-n_1^2}$. The masses are

$$m^2_{\tilde{\pi}_1} = 2c_\ell\epsilon^2 - 2w'\,, \qquad m^2_{\pi_2} = 2c_\ell\epsilon^2\,, \qquad m^2_{\tilde{\pi}_3} = 2c_\ell\epsilon^2 - \frac{\widehat{\mu}^2}{2c_\ell\epsilon^2}\,. \tag{2.37}$$

Note that $m_{\tilde{\pi}_1}$ and $m_{\pi_2}$ are independent of $\widehat{\mu}$, while the $\tilde{\pi}_3$ mass vanishes along the boundaries with the standard phases. The latter result is consistent with the results above because, on these boundaries $|n_1| = 1$ and so $\tilde{\pi}_3 = \pm\pi_3$.

A puzzling feature of these results is what happens at the boundaries between the central (green) and CP-violating (pink) phases. According to Eq. (2.35) it is the mass of $\pi_3$ which vanishes there, while Eq. (2.37) has the mass of $\tilde{\pi}_1$ vanishing. These appear to be different particles. This is related to a second puzzle, namely that the condensate is discontinuous across the boundary (which lies at $w' = c_\ell\epsilon^2$):

$$\langle\Sigma\rangle^{\text{Boundary}}_{\text{Green}} = i\frac{\widehat{\mu}}{2w'}\tau_1 \pm \sqrt{1-\frac{\widehat{\mu}^2}{4w'^2}}\mathbb{1} \;\text{ vs. }\; \langle\Sigma\rangle^{\text{Boundary}}_{\text{Pink}} = i\frac{\widehat{\mu}}{2w'}\tau_1 \pm i\sqrt{1-\frac{\widehat{\mu}^2}{4w'^2}}\tau_3\,. \tag{2.38}$$

Here the $\pm$ signs correspond to the two choices of vacuum state on each side. This situation can be understood by noting that, at the boundary, the vacuum manifold expands to a line which includes all four values of the condensate given in Eq. (2.38):

$$\langle\Sigma\rangle = i\frac{\widehat{\mu}}{2w'}\tau_1 + \sqrt{1-\frac{\widehat{\mu}^2}{4w'^2}}(\cos\phi + i\tau_3\sin\phi)\,, \tag{2.39}$$

where $\phi$ is arbitrary. The presence of this flat direction is the reason that one pion is massless, since there is no breaking of a $Z_2$ symmetry to explain the masslessness. The orientation of the flat direction, which is the direction of the massless pion, depends on the position along this vacuum manifold, and thus is different on the two sides of the transition. In this way to two puzzles above are simultaneously explained.

Results for pion masses are plotted in Fig. 2.8. We choose the same parameters for the plots as for the untwisted case, Fig. 2.6, so as to allow a clear comparison. The figures illustrate the discussion given above.

### *2.6 Arbitrary Twist*

In this section we give a brief discussion of the phase diagram at arbitrary twist. This allows us to understand how the phase diagrams presented above for untwisted and maximally-twisted quarks are related to one another. We focus on the phase diagram, and in particular, the position of the critical manifold where one or more pions are massless.

For arbitrary twist, the potential is given in Eq. (2.30). As before, minimization leads to $n_2 = 0$, so the potential depends only on $\theta$ and $\varphi_1$ (defined by $\cos\varphi_1 = n_1$). The equations for stationary points are

$$-\widehat{m}\sin\theta + \cos\theta\left[\widehat{\mu}\cos\varphi_1 + 2\sin\theta(c_\ell\epsilon^2\sin^2\varphi_1 - w')\right] = 0\,, \tag{2.40}$$

and Eq. (2.32). We focus on the case when both $\widehat{m}$ and $\widehat{\mu}$ are non-zero, since the special cases when one of these vanish have been discussed above.

When $|\widehat{\mu}|, |\widehat{m}| \gg c_\ell\epsilon^2, |w'|$ the solution which minimizes the potential has

$$n_1 = \cos\varphi_1 = 1, \quad n_3 = \sin\varphi_1, \quad \tan\theta \approx \frac{\widehat{\mu}}{\widehat{m}}\,. \tag{2.41}$$

The last equation becomes an equality in the continuum limit, and simply describes how the condensate twists to compensate the twist in the mass. Discretization errors (here proportional to $w'$) lead to a small deviation in $\theta$ from this continuum result. We do not quote the analytic form as it is not illuminating. In fact, the result for $\theta$ turns out to

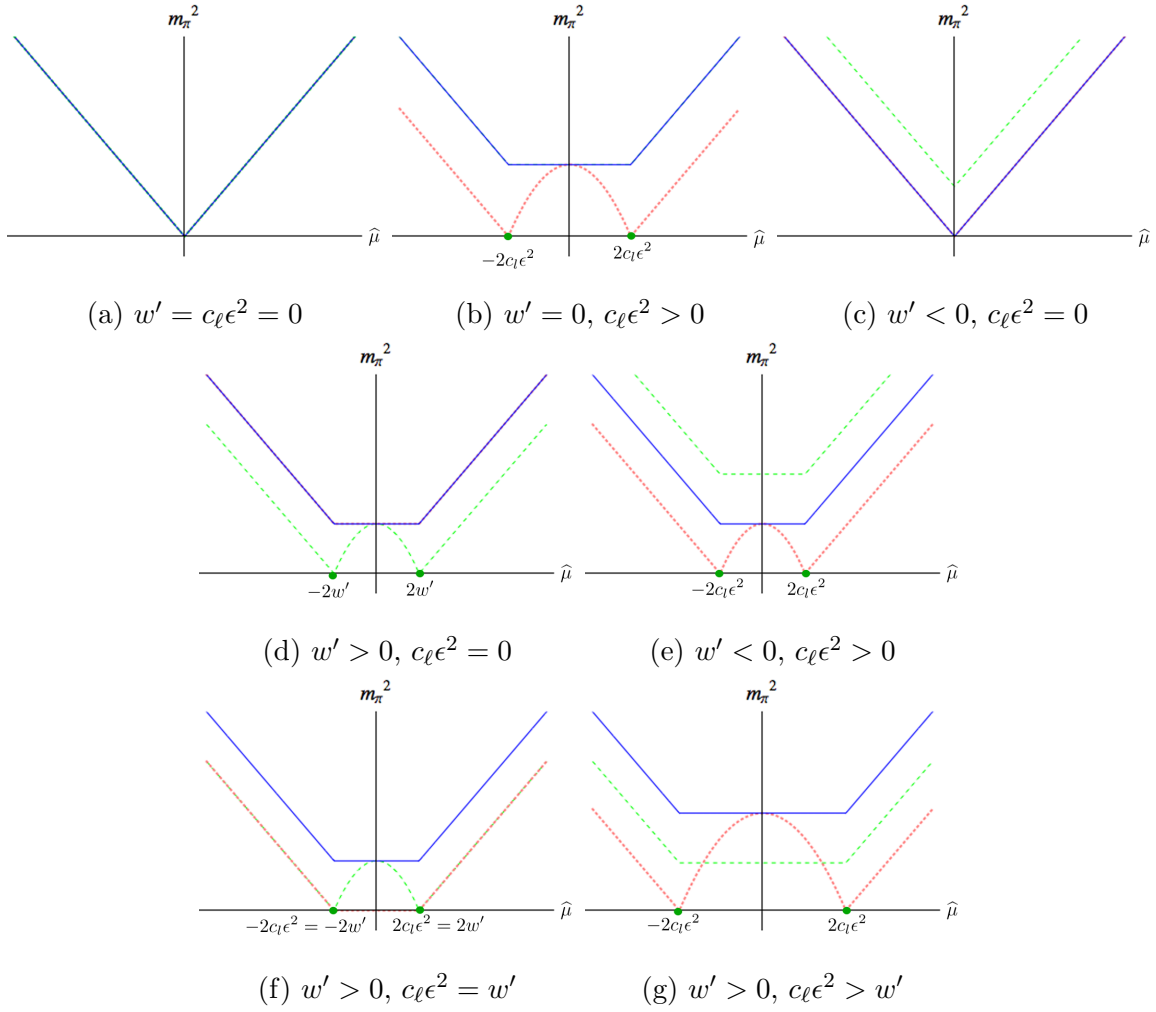


(a) $w' = c_\ell\epsilon^2 = 0$ (b) $w' = 0$, $c_\ell\epsilon^2 > 0$ (c) $w' < 0$, $c_\ell\epsilon^2 = 0$

(d) $w' > 0$, $c_\ell\epsilon^2 = 0$ (e) $w' < 0$, $c_\ell\epsilon^2 > 0$

(f) $w' > 0$, $c_\ell\epsilon^2 = w'$ (g) $w' > 0$, $c_\ell\epsilon^2 > w'$

Figure 2.8: Pion masses for maximally twisted fermions including the effects of both discretization ($w' \neq 0$) and non-degeneracy ($\epsilon \neq 0$). $m^2_{\pi_2}$ is shown by solid (blue) lines, $m^2_{\pi_3}$ (and $m^2_{\tilde{\pi}_3}$) by dotted (red) lines and $m^2_{\pi_1}$ (and $m^2_{\tilde{\pi}_1}$) by dashed (green) lines. Not all lines are visible in some figures due to degeneracies. Mixing of pions occurs only within the CP-violating phase in Figs. (e) and (g). Explicit expressions for masses and mixing are given in the text. Vertical scales differ between the figures.

be independent of the non-degeneracy $\epsilon$, so the results for the condensate given for the degenerate theory in Refs. [45, 52, 57] remain valid in this phase. This phase is the extension

of the "uncolored" phases in Figs. 2.5 and 2.7 to arbitrary twist. At a general position in this phase, the mass eigenstates are $\pi_1$, $\pi_2$ and $\pi_3$ [using the parametrization of Eq. (2.33)] and all have different masses.

As $\epsilon^2$ increases, we expect, based on the results of the previous two sections, that we will enter a phase which is connected to the CP-violating (pink) phases found above. This should have a condensate having components in both $n_1$ and $n_3$ directions, and $\theta$ taking non-extremal values. Indeed, if $\sin\theta$ and $\sin\varphi_1$ are both non-zero, Eq. (2.32) is solved by

$$\sin\theta\cos\varphi_1 = \frac{\widehat{\mu}}{2c_\ell\epsilon^2}\,. \tag{2.42}$$

This requires that $c_\ell\epsilon^2 \geq |\widehat{\mu}|$. Inserting this in Eq. (2.40) then yields

$$\cos\theta = \frac{\widehat{m}}{2(c_\ell\epsilon^2 - w')}\,, \tag{2.43}$$

which is valid if $2(c_\ell\epsilon^2 - w') \leq \widehat{m}$. The solution given by Eqs. (2.42) and (2.43) turns out to give the absolute minimum of the potential where it is valid. Its boundary with the continuum-like phase occurs when $|\cos\varphi_1| = 1$, and is thus described by

$$\left(\frac{\widehat{m}}{2(c_\ell\epsilon^2 - w')}\right)^2 + \left(\frac{\widehat{\mu}}{2c_\ell\epsilon^2}\right)^2 = 1\,. \tag{2.44}$$

For fixed $\epsilon$, this is an ellipse in the $\widehat{m}$, $\widehat{\mu}$ plane. One pion ($\pi_3$) is massless along this critical surface.

Within the CP-violating phase all pions are massive, with the mass eigenstates being $\pi_2$ and a mixture of $\pi_1$ and $\pi_3$. The general expressions for these masses are uninformative, and we quote only the results along the boundary of this phase. Here, in addition to the massless $\pi_3$ we find

$$m^2_{\pi_1} = 2c_\ell\epsilon^2 - \frac{2w'\widehat{\mu}^2}{(2c_\ell\epsilon^2)^2} \qquad\qquad m^2_{\pi_2} = 2c_\ell\epsilon^2\,. \tag{2.45}$$

The only other critical lines are those we found at maximal twist, namely at $\widehat{m} = 0$, $\widehat{\mu} = 2w'$ and $c_\ell\epsilon^2 \leq w'$.

The position of the critical manifold resulting from these considerations is shown in Fig. 2.9 for both scenarios and in the continuum. The CP-violating phases lie within the (distorted) cone-shaped regions. The contour plots show how the circular contours of the continuum are distorted by discretization effects into ellipses. We note that, in the first-order scenario shown in Fig. 2.9c, if one passes through any point in the rectangular region in the $(\widehat{m}, \epsilon)$ plane between the two critical lines there is a first-order transition at which the condensate changes discontinuously.

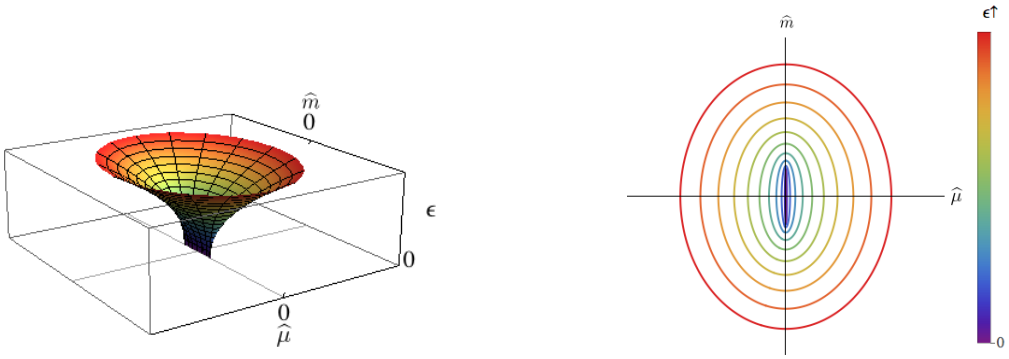


(a) Aoki scenario ($w' < 0$)

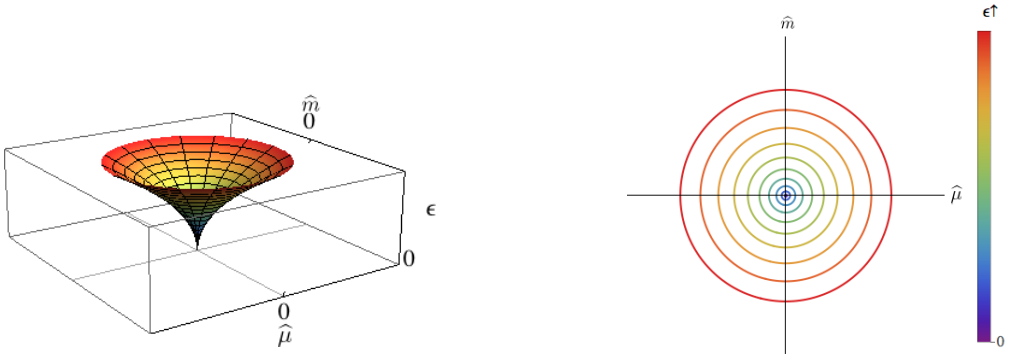


(b) Continuum ($w' = 0$)

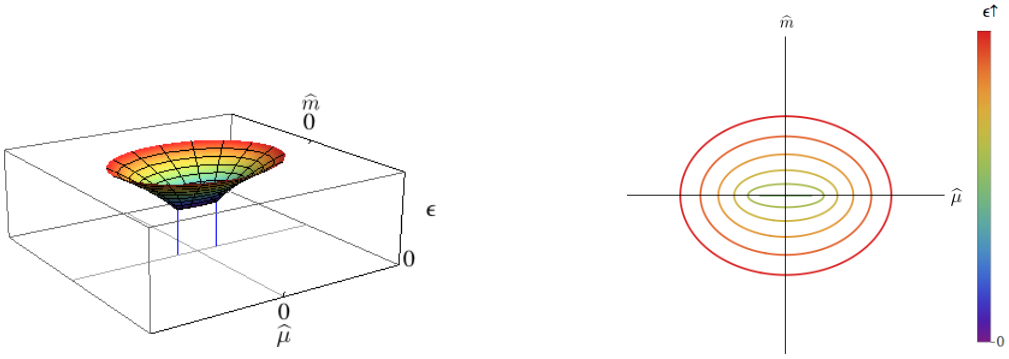


(c) First-order scenario ($w' > 0$)

Figure 2.9: Location of the critical manifold for arbitrary twist. Results are shown only for $\epsilon > 0$ since the phase diagrams are symmetric under reflection in the $\epsilon = 0$ plane. The left panels show 3-d plots, the right panels contour plots. For $w' > 0$, the contour plots do not include the two critical lines which reach down to the $\epsilon = 0$ plane. The scale used for $\widehat{m}$ and $\widehat{\mu}$ is the same, while that for $\epsilon$ is arbitrary. See text for the equations describing the critical manifold.

### *2.7 Higher order*

In this section we consider the effect on the previous results of the inclusion of the next highest order terms in our power counting, i.e. those scaling as $a^3 \sim ma$. At this order we can still determine the vacuum using the classical potential of the chiral theory. The $\mathcal{O}(ma)$ term in this potential is standard, see, e.g. Ref. [50]. The $\mathcal{O}(a^3)$ terms have been discussed for $\epsilon = 0$ in Ref. [53]; the results carry over unchanged to $\epsilon \neq 0$ since the first additional term involving $\epsilon$ scales as $a\epsilon^2$ and is of higher order in our power-counting. The relevant additional terms entering the potential are

$$\mathcal{V}_{a^3} = -\frac{wf^2}{32W_0 a}\,\mathrm{tr}(\chi^\dagger\Sigma + \Sigma^\dagger\chi)\,\mathrm{tr}(A^\dagger\Sigma + \Sigma^\dagger A) - \frac{w_3 f^2}{(8W_0 a)^3}\left[\mathrm{tr}(A^\dagger\Sigma + \Sigma^\dagger A)\right]^3 , \qquad (2.46)$$

where $w$ and $w_3$ are new LECs. There is also a term proportional to $\mathrm{tr}(A^\dagger A)\,\mathrm{tr}(A^\dagger\Sigma + \Sigma^\dagger A)$, but this can removed by (yet another) redefinition of $\chi$. Inserting our standard parametrization $\langle\Sigma\rangle = \exp(i\theta\vec{n}\cdot\vec{\tau})$, and combining the results with that from the LO potential, we obtain

$$-\frac{\mathcal{V}_{a^2,\ell_7,a^3}}{f^2} = (\widehat{m}\cos\theta + \widehat{\mu} n_1 \sin\theta)(1 + w\cos\theta) + c_\ell \epsilon^2 n_3^2 \sin^2\theta + w'\cos^2\theta + w_3\cos^3\theta\,. \quad (2.47)$$

The new LECs should satisfy $|w| \ll 1$ and $|w_3| \ll |w'|, |c_\ell\epsilon^2|$ in order to be consistent with our power counting.

We begin by considering the untwisted theory, $\widehat{\mu} = 0$, where the phase diagram and pion masses can be determined analytically. In this case $\widehat{m} = \chi_\ell$. As previously, the potential is minimized with $n_3 = 1$, so that

$$-\frac{\mathcal{V}_{a^2,\ell_7,a^3}}{f^2} \longrightarrow \chi_\ell\cos\theta(1 + w\cos\theta) + c_\ell\epsilon^2\sin^2\theta + w'\cos^2\theta + w_3\cos^3\theta\,. \qquad (2.48)$$

The stationary points satisfy

$$\sin\theta\left[\chi_\ell - 2(\chi_\ell w - c_\ell\epsilon^2 + w')\cos\theta + 3w_3\cos^2\theta\right] = 0\,, \qquad (2.49)$$

which is solved by $\sin\theta = 0$ (i.e. giving the usual continuum solutions with $\cos\theta = \pm 1$) and by the solutions to the quadratic function of $\cos\theta$ in parentheses. The latter will lead to CP-violating vacua.

To simplify the discussion we consider the impact of the new terms separately. We first set $w_3 = 0$. Then we can take $w > 0$ without loss of generality, since simultaneously changing $w \to -w$, $\theta \to \theta + \pi$ and $\chi_\ell \to -\chi_\ell$ leaves the potential unaffected. As the $w$ contribution to Eq. (2.49) leaves the function in parentheses linear in $\cos\theta$, the analysis is little changed from that at LO (see Sec. 2.4). We find that the CP-violating solution,

$$\cos\theta = \frac{\chi_\ell}{2(c_\ell\epsilon^2 - w' - \chi_\ell w)}\,, \tag{2.50}$$

minimizes the potential where it is valid, i.e. wherever $|\cos\theta| < 1$. The endpoints of this phase give second-order transitions occurring at masses

$$\chi_\ell = \pm\frac{2(c_\ell\epsilon^2 - w')}{1 \pm 2w}\,. \tag{2.51}$$

Thus the phase boundaries are no longer symmetric with respect to $\chi_\ell = 0$. As in the LO case, if $w' > 0$ and $c_\ell\epsilon^2 < w'$, the transition becomes first order (with the $w$ term having no impact since the transition occurs at $\chi_\ell = 0$). The resultant phase diagrams are shown in Fig. 2.10.

We have also calculated the pion masses. In the CP-conserving phases the results are

$$m_{\pi^0}^2 = |\chi_\ell|(1 + \mathrm{sign}(\chi_\ell)2w) - 2(c_\ell\epsilon^2 - w')\,, \tag{2.52}$$

$$m_{\pi^\pm}^2 = m_{\pi^0}^2 + 2c_\ell\epsilon^2\,. \tag{2.53}$$

The only change from the LO results, Eqs. (2.23) and (2.24), is that the slope with respect to $\chi_\ell$ is no longer symmetric when $\chi_\ell$ changes sign. In the CP-violating phases we find

$$m_{\pi^0}^2 = 2(c_\ell\epsilon^2 - w' - \chi_\ell w)\sin^2\theta \quad \text{and} \quad m_{\pi^\pm}^2 = 2c_\ell\epsilon^2\,, \tag{2.54}$$

where again only the former result is changed. The resulting pion masses are shown in Fig. 2.11, and show clearly the above-mentioned asymmetry.

We now consider the impact of the $w_3$ term, setting $w = 0$. Again, without loss of generality, we can assume $w_3 > 0$. The CP-violating stationary points are now obtained from Eq. (2.49) by solving a quadratic equation, leading to the solutions

$$\cos\theta_\pm = \frac{(c_\ell\epsilon^2 - w') \pm \sqrt{(c_\ell\epsilon^2 - w')^2 - 3\chi_\ell w_3}}{3w_3}\,. \tag{2.55}$$

It is straightforward to see from the properties of a cubic that, since $w_3 > 0$, only the $\theta_-$ solution can lead to a minimum of the potential. Whether it does lead to a minimum is a more subtle question than in the LO analysis.

We begin by discussing the limit of small $|w_3|$. Specifically, if we assume $|c_\ell \epsilon^2 - w'| \sim |\chi_\ell| \gg |w_3|$, the square root in Eq. (2.55) can be expanded in powers of $w_3$. It is then straightforward to show that one recovers the LO results aside from small corrections proportional to $|w_3/(c_\ell \epsilon^2 - w')|$. In particular, if $c_\ell \epsilon^2 - w' > 0$ there is a CP-violating phase ending in second-order transitions to continuum-like phases, while if $c_\ell \epsilon^2 - w' < 0$ there is a first-order transition.

The positions of these transitions are, however, shifted slightly by the $w_3$ term. The boundaries of the CP-violating phase occur when $\cos\theta_- = \pm 1$ which gives

$$\chi_\ell = \pm 2(c_\ell \epsilon^2 - w') - 3w_3 \,, \tag{2.56}$$

without any $\mathcal{O}(w_3^2)$ corrections. In words, the boundaries are simply offset from the LO result, Eq. (2.21), by $-3w_3$. In the first-order scenario, the transition occurs at the value of $\chi_\ell$ such that the potentials at $\cos\theta = \pm 1$ agree. This happens when

$$\chi_\ell = -w_3 \,, \tag{2.57}$$

so that the first-order transition line is offset from the LO result $\chi_\ell = 0$ by $-w_3$ (again, without any higher-order corrections).

More interesting changes occur when $|c_\ell \epsilon^2 - w'| \sim |w_3|$. Note that this does not require that $w_3$ be large, but rather that there is a cancellation between the $c_\ell \epsilon^2$ and $w'$ terms. Here we encounter a phenomenon first noted at $\epsilon = 0$ in Ref. [53]: one can have a *first-order* transition from the continuum-like phase into the CP-violating phase, followed by a second-order transition to the other continuum-like phase. This occurs when the local minimum at $\theta_-$ (with $|\cos\theta_-| < 1$ and $\cos\theta_-$ real) has the same potential as that at $\cos\theta = 1$. Then, as $\chi_\ell$ is reduced, $\theta$ jumps from $\theta = 0$ to $\theta_-$. This is possible with a cubic potential, but not with a quadratic. Solving

$$\mathcal{V}_{a^2,\ell_7,a^3}(\theta_-) = \mathcal{V}_{a^2,\ell_7,a^3}(0) \tag{2.58}$$

leads to the following equation for the first-order boundary

$$\chi_\ell = \frac{(w' - c_\ell\epsilon^2 - 3w_3)(w' - c_\ell\epsilon^2 + w_3)}{4w_3}\,. \tag{2.59}$$

As one moves along this boundary $\cos\theta_-$ varies. The boundary ends when either $\cos\theta_- = 1$, so there is no jump in $\theta$, and the transition becomes second-order, or when $\cos\theta_- = -1$, so there is only a first-order transition without the subsequent CP-violating phase. Combining Eqs. (2.55) and (2.59) we find that the transition becomes second-order at

$$\chi_\ell = c_\ell\epsilon^2 - w' = 3w_3\,, \tag{2.60}$$

while it becomes first-order at

$$\chi_\ell = c_\ell\epsilon^2 - w' = -w_3\,. \tag{2.61}$$

The first of these equations can be satisfied if $w' > -3w_3$, and so reaches from the first-order scenario ($w' > 0$) into a small region of the Aoki scenario. The second requires $w' > w_3$ and thus occurs only in the first-order scenario.

These results lead to the phase diagrams shown in Fig. 2.12. We see that the changes due to the $w_3$ term are more substantive than those due to the $w$ term.

We show the corresponding pion masses in Figs. 2.13-2.15; for the sake of brevity we do not quote the analytic forms. Fig. 2.13 shows two "slices" through the phase diagram of Fig. 2.12a. These should be compared to the LO results in Figs. 2.5c and 2.5e, respectively.

In Fig. 2.14 we show two slices through the phase diagram of Fig. 2.12b. The first, at $\epsilon = 0$, shows the first-order transition, at which all pion masses are discontinuous. The charged pions become massless in the CP-violating/Aoki phase, while the neutral pion is massive. In the second slice, for which $\epsilon$ satisfies $0 < c_\ell\epsilon^2 < w' + 3w_3$, the discontinuities remain, but all pions are massive in the CP-violating phase (except at the lower boundary where the neutral pion mass vanishes). Once $c_\ell\epsilon^2 \geq w' + 3w_3$, the pion masses behave as in Fig. 2.13b.

In Fig. 2.15 we show four slices through the phase diagram of Fig. 2.12c. The first (at $\epsilon = 0$) shows how the $w_3$ term leads to a discontinuity in the pion masses at the first-order

transition, unlike at LO. This was first observed in Ref. [53]. For non-zero $\epsilon$, the charged and neutral pions are no longer degenerate, and both have a discontinuity. When one reaches $c_\ell \epsilon^2 = w' - w_3$, the neutral pion becomes massless at the transition point, as shown in the second slice. This is the beginning of the CP-violating phase. As $\epsilon^2$ increases further, one has both first and second-order transitions, as shown in the third slice. The final slice shows the value of $\epsilon^2$ at which the first-order transition turns into a second-order transition. For larger values of $\epsilon^2$ the pion masses behaves as in Fig. 2.13b.

The higher-order analysis in the twisted case is more complicated. Maximal twist no longer occurs, in general, at $\widehat{m} = 0$, so one is forced to do the analysis for both $\widehat{m}$ and $\widehat{\mu}$ non-vanishing. In practice, this requires numerical minimization of the potential. The resulting phase diagram and pion masses for $\epsilon = 0$ have been discussed in detail in Ref. [53]. The addition of isospin-breaking leads both to small quantitative changes, and to qualitative changes in small regions of the phase plane. We restrict ourselves here to showing how the NLO terms impact the critical manifold (on which at least one pion is massless). The Aoki and first-order scenarios are shown, respectively, in Figs. 2.16 and 2.17.

The main effect is a distortion of the elliptical cross sections of the critical manifold. In addition, the two vertical critical lines in the first-order scenario are shifted slightly in position. The most significant qualitative change is the appearance of a hole in the manifold when $w' > w_3 > 0$, which is (barely) visible above the $\widehat{\mu} = 0$ axis in the right panel of Fig. 2.17c. This occurs because of the extended first-order transition region seen in the untwisted phase diagram of Fig. 2.12c.

We end this section by addressing the question of whether higher-order effects move unphysical phases closer to the point with physical masses. The answer depends on the sign of $w$ and $w_3$. For untwisted fermions, the results of Figs. 2.10-2.17, show that positive $w$ and $w_3$ move unphysical phases away from the physical point. Conversely, negative values of these LECs would move the phases closer. For twisted-mass fermions the answer is more complicated, depending on the choice of twist angle.

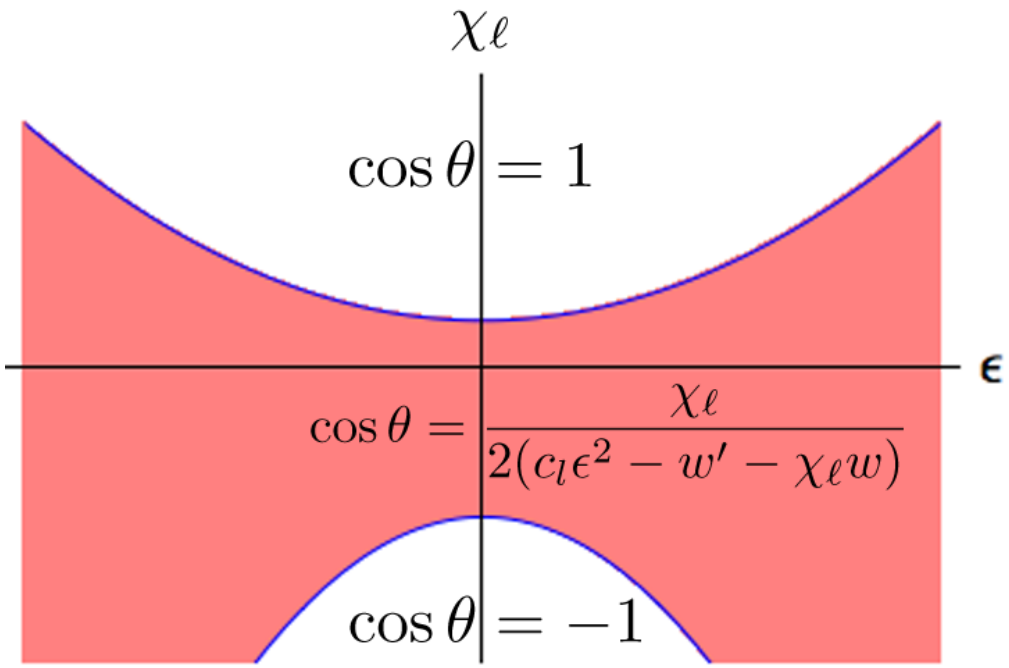


(a) Aoki Scenario ($w' < 0$)

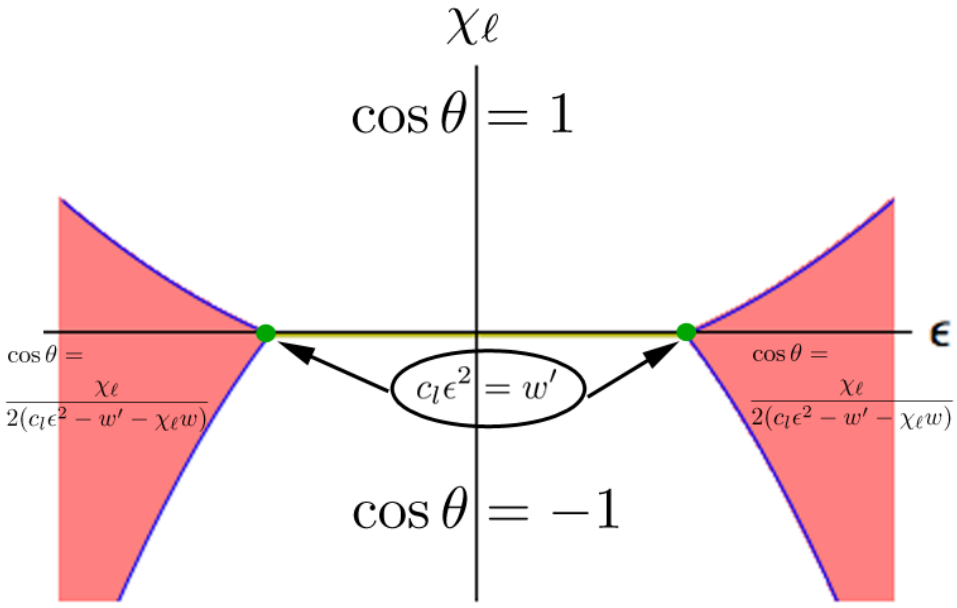


(b) First-Order Scenario ($w' > 0$)

Figure 2.10: Phase diagrams for untwisted Wilson quarks including the NLO $\mathcal{O}(ma)$ term proportional to $w$. Compare to LO results in Fig. 2.5.

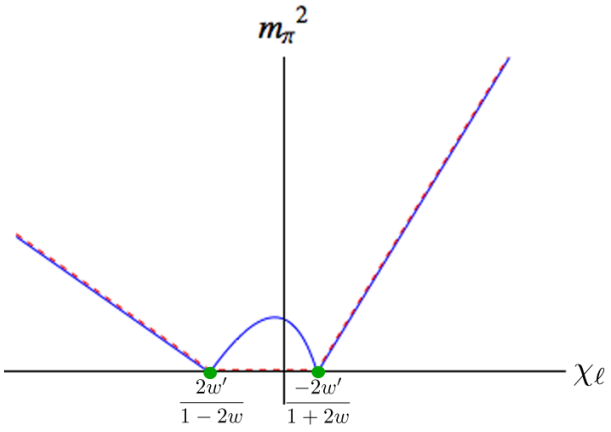


(a) $w' < 0$, $c_\ell \epsilon^2 = 0$, $w > 0$

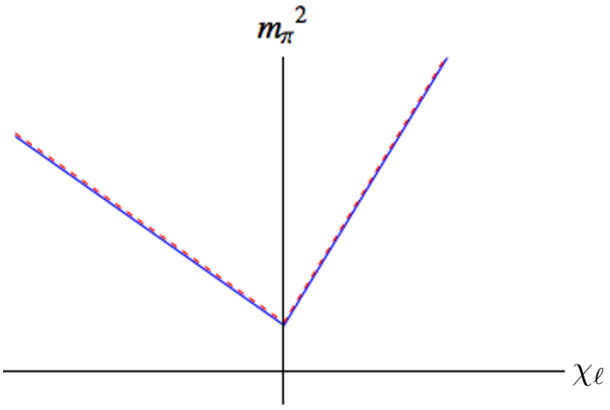


(b) $w' > 0$, $c_\ell \epsilon^2 = 0$, $w > 0$

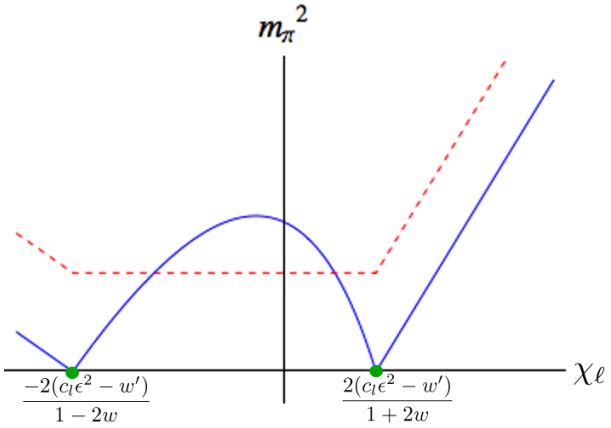


(c) $w' < 0$, $c_\ell \epsilon^2 > 0$, $w > 0$

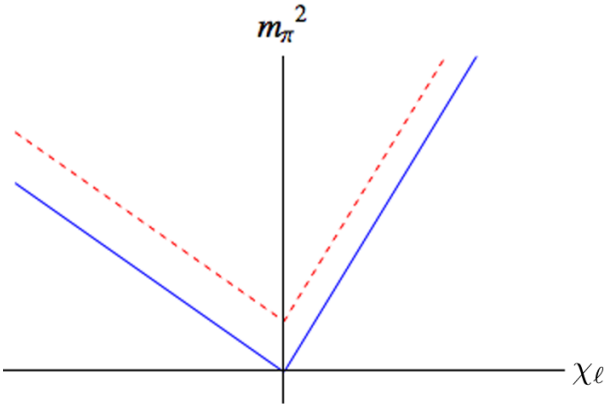


(d) $c_\ell \epsilon^2 = w' > 0$, $w > 0$

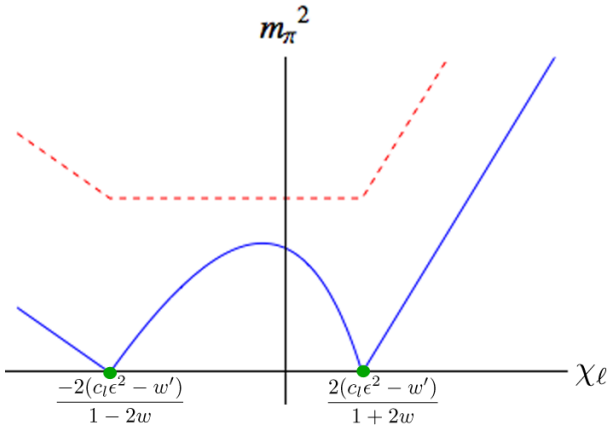


(e) $c_\ell \epsilon^2 > w' > 0$, $w > 0$

Figure 2.11: Pion masses for untwisted Wilson fermions including the effects of the NLO $w$ term with $w > 0$ (but with $w_3 = 0$). The figures should be compared to the LO results in Figs. 2.6(c-g), respectively. See Fig. 2.6 also for notation.

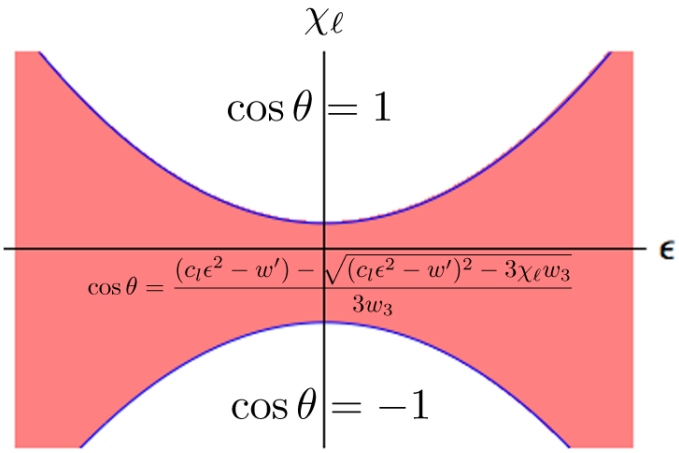


(a) Aoki scenario with $w' < -3w_3 < 0$

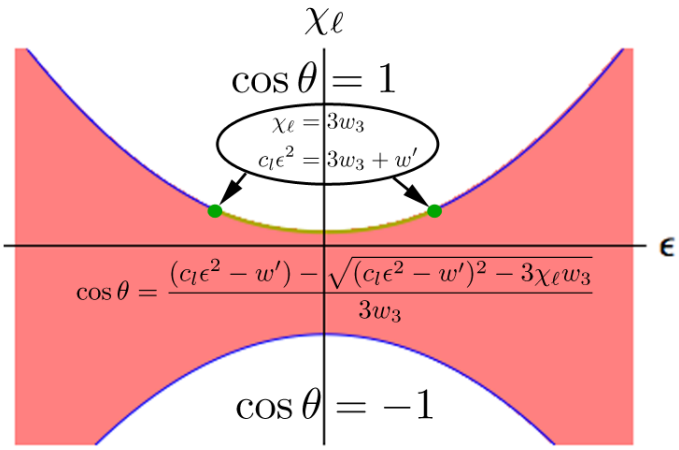


(b) Aoki or first-order scenario with $-3w_3 < w' < w_3$ (and $w_3 > 0$)

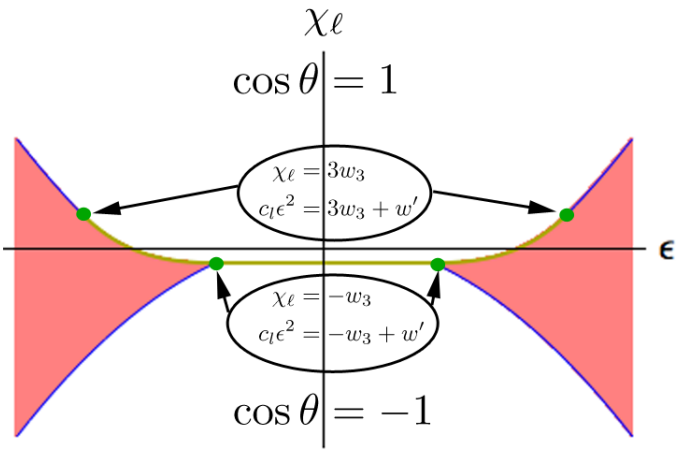


(c) First-order scenario with $w' > w_3 > 0$; $\cos\theta$ in pink region is as is in (a) and (b)

Figure 2.12: Phase diagrams for untwisted Wilson fermions including the NLO $\mathcal{O}(a^3)$ term proportional to $w_3$. Compare to LO results in Fig. 2.5.

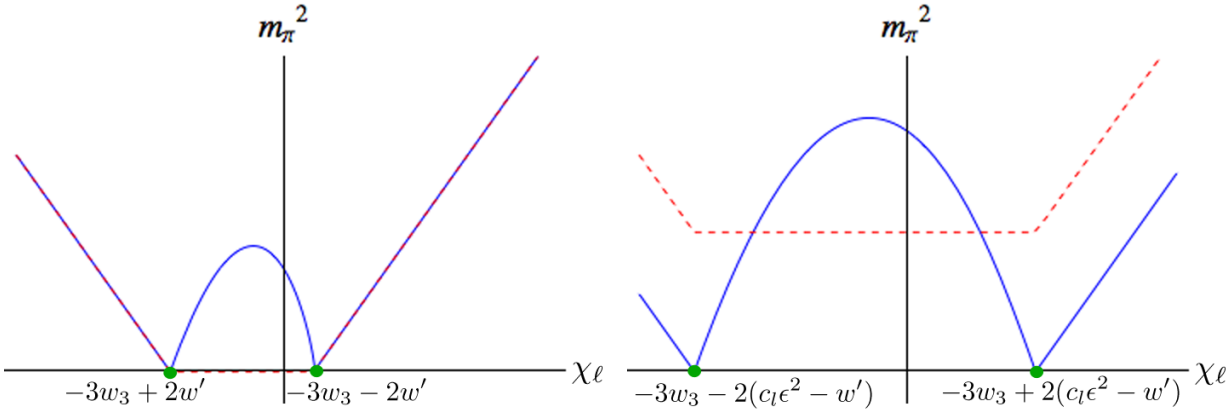


(a) $c_\ell\epsilon^2 = 0$, $-w' < -3w_3 < 0$ (b) $c_\ell\epsilon^2 > 0$, $-w' < -3w_3 < 0$

Figure 2.13: NLO pion masses for untwisted Wilson fermions with $w_3 > 0$ and $w = 0$. Results are for the Aoki scenario with $w' < -3w_3 < 0$, corresponding to the phase diagram of Fig. 2.12a. Notation as in Fig. 2.6.

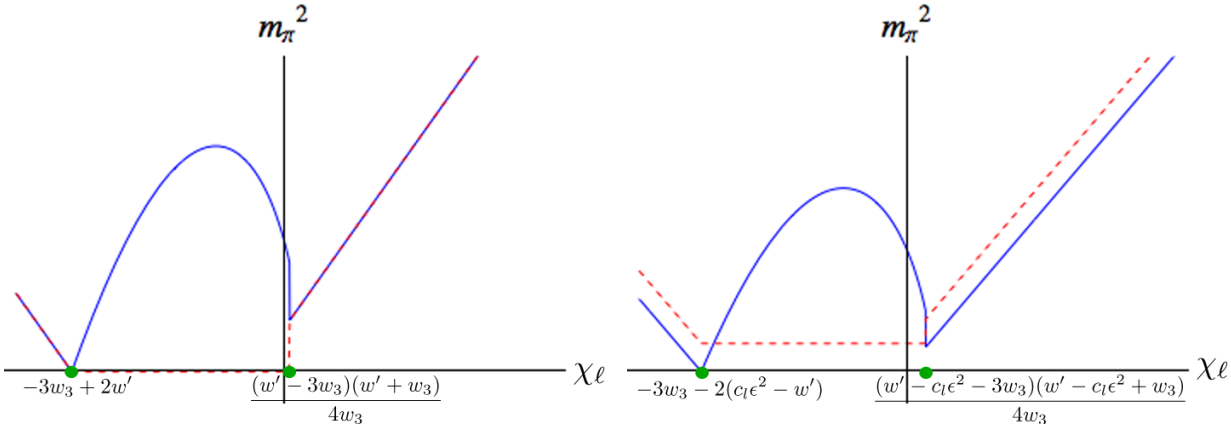


(a) $c_\ell\epsilon^2 = 0$, $-3w_3 < w' < w_3$ (b) $c_\ell\epsilon^2 \geq w' + 3w_3$, $-3w_3 < w' < w_3$

Figure 2.14: Examples of NLO pion masses for untwisted Wilson fermions with $w_3 > 0$ and $w = 0$. Results are for $-3w_3 < w' < w_3$, corresponding to the phase diagram of Fig. 2.12b.

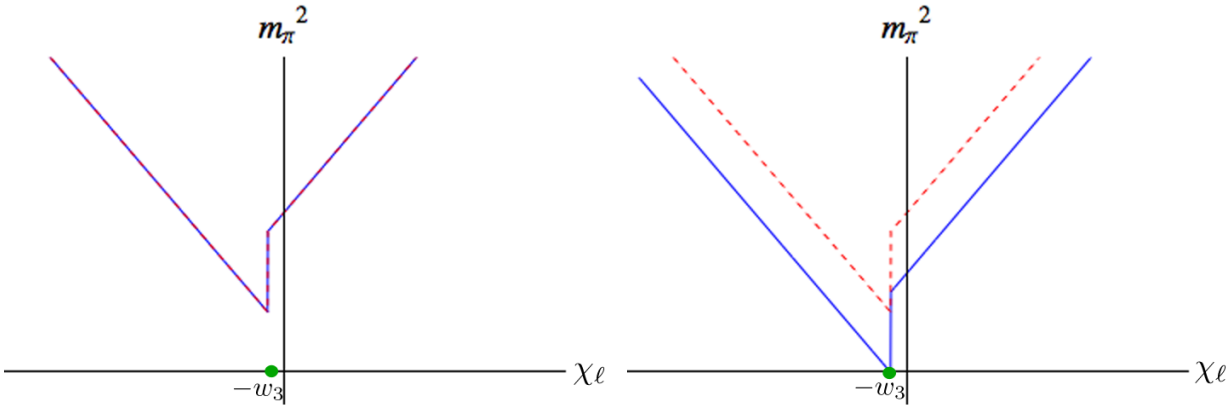


(a) $c_\ell\epsilon^2 = 0$, $w' > w_3 > 0$




(b) $c_\ell\epsilon^2 = w' - w_3$, $w' > w_3 > 0$

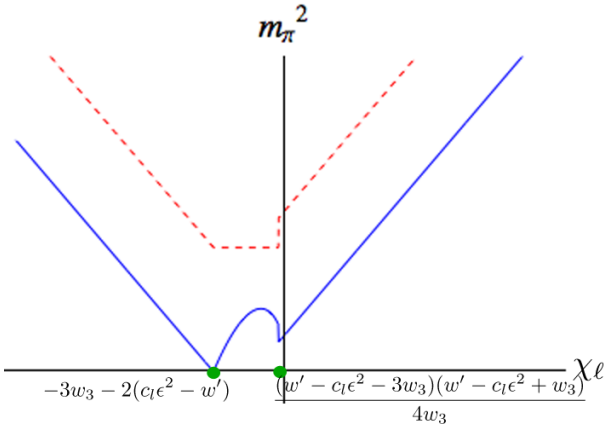


(c) $w' - w_3 < c_\ell\epsilon^2 < w' + 3w_3$, $w' > w_3 > 0$

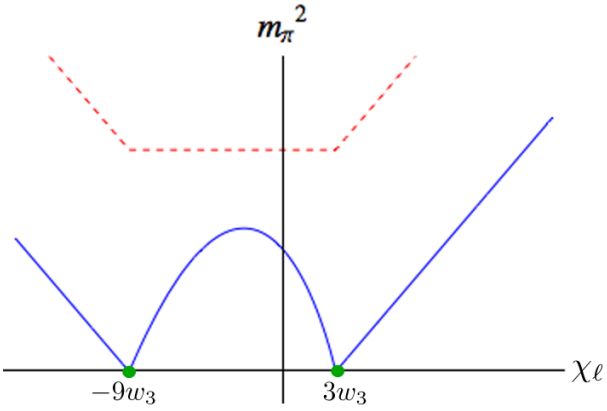


(d) $c_\ell\epsilon^2 = w' + 3w_3$, $w' > w_3 > 0$

Figure 2.15: NLO pion masses for untwisted Wilson fermions with $w_3 > 0$ and $w = 0$. Results are for the first-order scenario with $w' > w_3$, corresponding to the phase diagram of Fig. 2.12c.

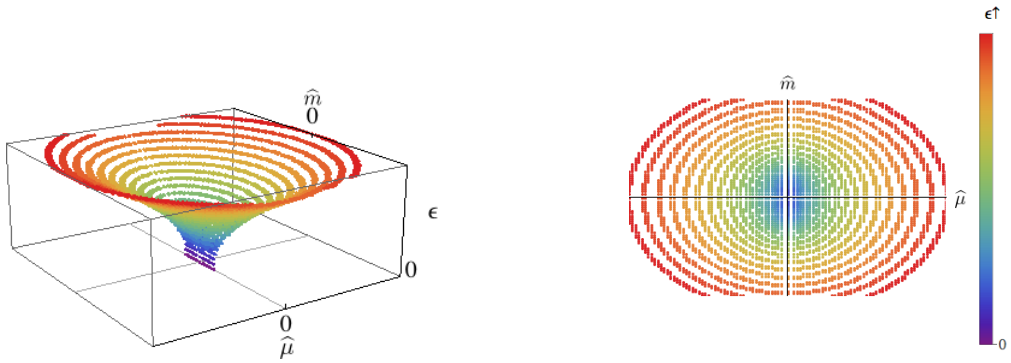


(a) $w_3 = w = 0$

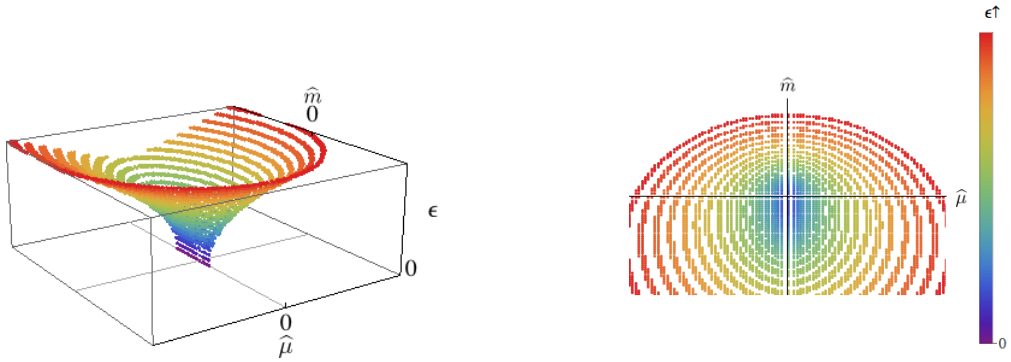


(b) $w_3 = 0$, $w > 0$

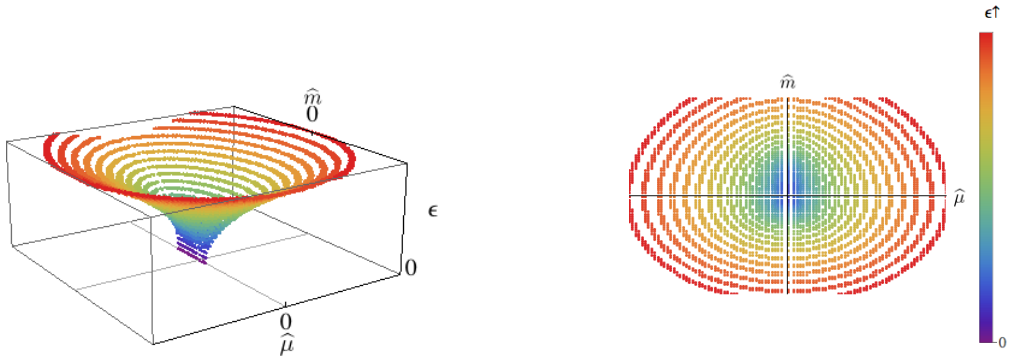


(c) $w' < -3w_3 < 0$, $w = 0$

Figure 2.16: Location of the critical manifold in the Aoki scenario ($w' < 0$) including NLO terms. Notation as in Fig. 2.9.

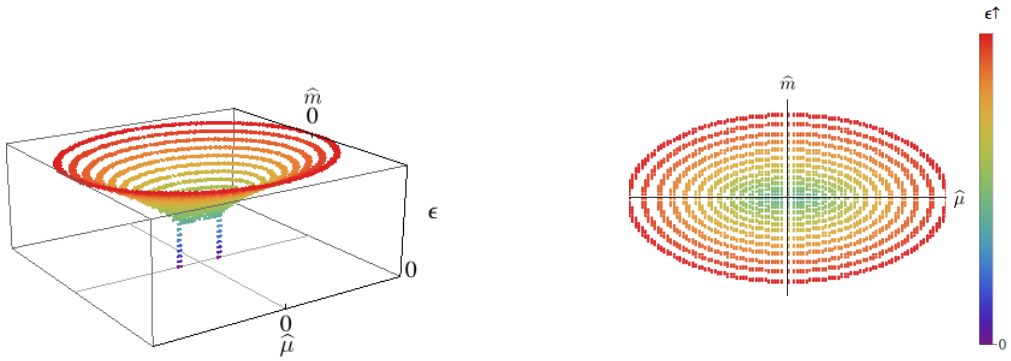


(a) $w_3 = w = 0$

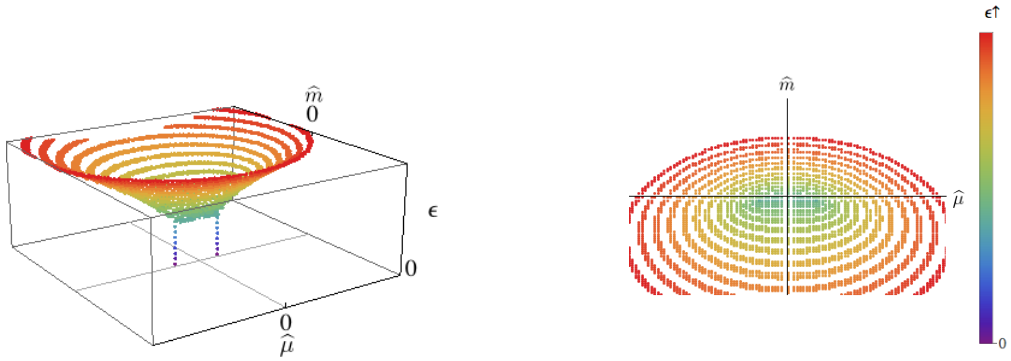


(b) $w_3 = 0$, $w > 0$

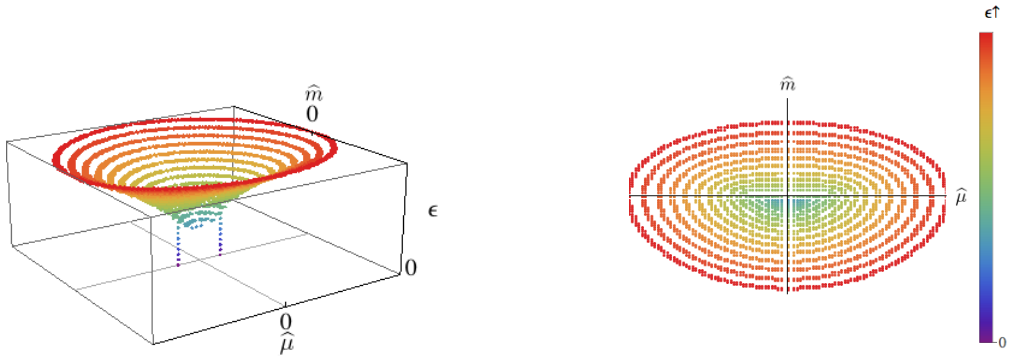


(c) $w' > w_3 > 0$, $w = 0$

Figure 2.17: Location of the critical manifold in the first-order scenario ($w' > 0$) including NLO terms. Notation as in Fig. 2.9.

### *2.8 Conclusions*

In this work we have studied how using non-degenerate up and down quarks changes the phase structure caused by competition between quark mass and discretization effects. We draw two main conclusions. First, the continuum CP-violating phase is continuously connected to the Aoki phase induced by discretization effects. Second, discretization effects can move the theory with physical quark masses closer to, or even into, unphysical phases. Whether this happens depends both on the twist angle and on the details of the discretization (the latter impacting the values of the LECs $w'$, etc.). Our overall message is that a complicated phase structure lies in the vicinity of the physical point and simulations should be careful to avoid unphysical phases.

For twisted mass fermions our results for pion masses extend those of Ref. [46] into the Aoki regime ($m \sim a^2$). In the continuum-like phase, with both twisting and non-degeneracy, the eigenstates are $\pi_1$, $\pi_2$ and $\pi_3$, with all three pions having different masses. Our formulae may be of use in removing the discretization effects from masses determined in simulations, although we stress again that $\mathcal{O}(m^2)$ terms dropped in our power counting may be important if precision fitting is required.

One shortcoming of this work is that it does not include electromagnetic effects. In the pion sector, these lead to isospin breaking that is generically larger than that from quark non-degeneracy, and can also impact the phase structure.[10] We will discuss the impact of electromagnetism in Chapter 3 and 4.building upon the recent analysis of Ref. [34].

### *Acknowledgments*

We thank Mario Kieberg and Jac Verbaarschot for discussions and comments. This work was facilitated through the use of advanced computational, storage, and networking infrastructure provided by the Hyak supercomputer system at the University of Washington. This

[10] Another generalization that one can consider is the inclusion of an isospin chemical potential. This has been discussed recently for degenerate quarks in Ref. [42].

work was supported in part by the United States Department of Energy grants DE-FG02-96ER40956 and DE-SC0011637.

# Chapter 3

# IMPACT OF ELECTROMAGNETISM ON PHASE STRUCTURE FOR WILSON AND TWISTED-MASS FERMIONS INCLUDING ISOSPIN BREAKING [1]

## *3.1 Introduction*

The phase diagram of lattice QCD (LQCD) can contain unphysical transitions and unwanted phases due to discretization effects. A well known example is the Aoki phase that can be present with Wilson-like fermions [3].[2] Unphysical phases occur when the effects of physical light quark masses are comparable to those induced by discretization, specifically $m \sim a^2\Lambda_{\rm QCD}^3$, with $a$ the lattice spacing. This can be shown by extending chiral perturbation theory ($\chi$PT) to include the effects of discretization [56]. Understanding the phase structure is necessary so that LQCD simulations can avoid working close to unphysical phases, so as to avoid distortion of results and critical slowing down.

In Ch. 2, we extended the analysis of the phase diagram to the case of nondegenerate up and down quarks for Wilson-like and twisted-mass fermions. This was prompted by the recent incorporation of mass splittings into simulations of LQCD.[3] We found a fairly complicated phase structure, in which, for example, the Aoki phase was continuously connected to Dashen's CP-violating phase [19, 16].

A drawback of our analysis was that it did not include the other major source of isospin breaking in QCD, namely electromagnetism. For most hadron properties, electromagnetic effects are comparable to those of the mass nondegeneracy $\epsilon_q = (m_u - m_d)/2$. For example, in

---

[1] This chapter is adapted with minimal changes from Ref. [39]

[2] "Wilson-like" refers to both unimproved and improved versions of Wilson fermions. The choice will not matter in this work.

[3] For recent reviews of such simulations see Refs. [49, 64].

the neutron-proton mass difference these two effects lead to contributions of approximately $-1$ MeV and 2.5 MeV, respectively.[4] Furthermore, the recent LQCD simulations alluded to above have included both mass nondegeneracy and electromagnetism. Thus, to be directly applicable to such simulations, we must extend our analysis to include electromagnetism. This is the purpose of the present note.

We work in Wilson or twisted-mass $\chi$PT (both of which we refer to as W$\chi$PT for the sake of brevity) using a power-counting to be explained in Sec. 3.2. At the order we work, it turns out that the inclusion of electromagnetism can be accomplished in most cases simply by shifting low-energy coefficients (LECs) in the results without electromagnetism. Thus we can take over many results from Ch. 2 without further work.

One new issue concerns the simultaneous inclusion of electromagnetism and quark nondegeneracy with twisted-mass fermions. The approach we used in the absence of electromagnetism in Ch. 2 (following Ref. [29]) was to apply the twist in a different direction in isospin space ($\tau_1$) from that in which the masses are split ($\tau_3$). This leads to a real quark determinant, and is the method used to simulate the $s$ and $c$ quarks using twisted-mass fermions (see, e.g., Ref. [15]). This does not, however, generalize to include electromagnetism in a gauge-invariant way. Here, instead, we follow Ref. [23], and twist in the $\tau_3$ direction. When doing simulations, this has the disadvantage of leading to a complex quark determinant,[5] but there are no barriers to studying the theory with $\chi$PT.

The remainder of chapter is organized as follows. We begin in Sec. 3.2 with a brief discussion of our power-counting scheme and a summary of relevant results from Ch. 2. We then explain, in Sec. 3.3, how electromagnetism changes the results of Ch. 2 for the case of Wilson-like fermions. Section 3.4 describes how to simultaneously include isospin breaking, electromagnetism and twist, while Sec. 3.5 gives our corresponding results for the phase diagram, focusing mainly on the case of maximal twist. We conclude in Sec. 3.6.

---

[4]These results are from the recent LQCD calculation of Ref. [14], and use the convention of that work for the separation of electromagnetic and $\epsilon_q$ effects.

[5]This is avoided in Refs. [22, 23] by expanding about the theory with degenerate quarks and no electromagnetism.

Two technical issues are discussed in appendices. The first concerns the renormalization factors needed to relate lattice masses to the continuum masses that appear in $\chi$PT. This issue is subtle because singlet and nonsinglet masses renormalize differently. This point was not discussed in Ch. 2, and we address it in Appendix A.1, except that we do not include all the effects introduced by electromagnetism.

The second appendix concerns the need for charge-dependent critical masses in the presence of electromagnetism. These must be determined nonperturbatively, and various methods for doing so have been used in the literature. One of these methods, proposed in Ref. [23], can be implemented using partially quenched (PQ) $\chi$PT, and thus checked. This is done in App. A.2. We find that the method only provides one constraint on the up and down critical masses and must be supplemented by an additional condition in order to determine both.

Appendix A.2 requires results from a $\chi$PT analysis of a theory with twisted nondegenerate charged quarks at nonzero lattice spacing *and at nonvanishing* $\theta_{\rm QCD}$. We provide such an analysis in Chapter 4.

### *3.2 Power-counting and summary of previous work*

In order to study the low-energy properties of LQCD, we must decide on the relative importance of the competing effects. The power counting that we adopt is

$$m \sim p^2 \sim a^2 \sim \alpha_{\rm EM} > \epsilon_q^2 > ma \sim a^3 \sim a\alpha_{\rm EM} \ldots , \tag{3.1}$$

where $m$ represents either $m_u$ or $m_d$. This is the power counting adopted in Ch. 2, except that electromagnetic effects are now included. This scheme only makes sense if discretization errors linear in $a$ are absent, either because the action is improved or because the $O(a)$ terms can be absorbed into a shift in the quark masses (as is the case in W$\chi$PT [56]).

The explanation for the choice of leading order (LO) terms in this power-counting is as follows. Present simulations have $1/a \approx 3$ GeV, and using this together with $\Lambda_{\rm QCD} \approx 300$ MeV we find $a\Lambda_{\rm QCD} \approx 0.1$. Thus second order discretization effects are of relative size $(a\Lambda_{\rm QCD})^2 \approx 0.01$. This is comparable to $\alpha_{\rm EM}$, $m_u/\Lambda_{\rm QCD}$ and $m_d/\Lambda_{\rm QCD}$ (given that

$m_u \approx 2.5$ MeV and $m_d \approx 5$ MeV [4, 47]). The results for the neutron-proton mass difference described in the Introduction are consistent with this power-counting (using the fact that $m_u - m_d \sim m_u \sim m_d$).

The choice of $\epsilon_q^2$ as the dominant subleading contribution is less obvious, and is discussed in some detail in Ch. 2. The essence of the argument is that, while the $\epsilon_q^2$ terms are not necessarily numerically larger than generic $m^2$ terms, they give the leading contribution from quark mass differences to isospin breaking in the low-energy effective theory. For example, these contributions give rise to the CP-violating phase in the continuum analysis.[6]

In this note we keep only terms up to and including those proportional to $\epsilon_q^2$, so that we have the leading order term of each type. We refer to this as working at LO$^+$ indicating that it goes slightly beyond keeping only LO terms.

We now collect the relevant results from Ch. 2 concerning the phase diagram of Wilson-like fermions in the presence of nondegeneracy. We work entirely in SU(2) W$\chi$PT, in which the chiral field is $\Sigma \in \mathrm{SU}(2)$. The LO$^+$ chiral Lagrangian for Wilson-like fermions (whether improved or not) is

$$\mathcal{L}_\chi = \frac{f^2}{4} \operatorname{tr}\left[\partial_\mu \Sigma \partial_\mu \Sigma^\dagger\right] + \mathcal{V}_\chi \tag{3.2}$$

$$\mathcal{V}_\chi = -\frac{f^2}{4} \operatorname{tr}(\chi^\dagger \Sigma + \Sigma^\dagger \chi) - W'[\operatorname{tr}(\hat{A}^\dagger \Sigma + \Sigma^\dagger \hat{A})]^2 + \frac{\ell_7}{16}[\operatorname{tr}(\chi^\dagger \Sigma - \Sigma^\dagger \chi)]^2 , \tag{3.3}$$

where $\hat{A} = 2W_0 a \mathbb{1}$ is the spurion field used to introduce lattice artifacts. This Lagrangian contains several LECs: $f \approx 92$ MeV and $B_0$ from LO continuum $\chi$PT, $W_0$ and $W'$ introduced by disretization errors, and $\ell_7$. The latter, though of next-to-leading order (NLO) in standard continuum power-counting, leads to contributions proportional to $\epsilon_q^2$ and thus we keep it in our LO+ calculation. $\ell_7$ is not renormalized at one-loop order, and matching with SU(3) $\chi$PT leads to the estimate [31]

$$\ell_7 = \frac{f^2}{8 B_0 m_s} , \tag{3.4}$$

[6] A further justification for this choice, also discussed in Ch. 2, is that in SU(3) $\chi$PT such terms are of LO, since they are proportional to $(m_u - m_d)^2/m_s$.

indicating that $\ell_7$ is positive.

The final ingredient in Eq. (4.2) is $\chi = 2B_0 M$, which contains the mass matrix $M = \mathrm{diag}(m_u, m_d)$, with $m_{u,d}$ renormalized masses in a mass-independent scheme. Since $\mathcal{L}_\chi$ is supposed to represent the long-distance physics of a lattice simulation close to the chiral and continuum limits, to use it we need to know the relationship between bare lattice masses and the renormalized masses. This relationship is nontrivial when using nondegenerate quarks, and is discussed in Appendix A.1. This point was overlooked in Ch. 2.

To determine the vacuum of the theory, we must minimize the potential $\mathcal{V}_\chi$. Writing $\langle \Sigma \rangle = e^{i\theta \hat{n}\cdot\vec{\tau}}$, the potential becomes

$$\mathcal{V}_\chi = -f^2 \left( \widehat{m}_q \cos\theta + c_\ell \hat{\epsilon}_q^2 n_3^2 \sin^2\theta + w' \cos^2\theta \right) , \tag{3.5}$$

where

$$\widehat{m}_q = B_0(m_u + m_d),\ \hat{\epsilon}_q = 2B_0\epsilon_q, \tag{3.6}$$

$$c_\ell = \frac{\ell_7}{f^2},\ w' = \frac{64 W' W_0^2 a^2}{f^2}. \tag{3.7}$$

Assuming $c_\ell > 0$ [based on the estimate (3.4)], the resulting phase diagrams are shown in Fig. 3.1. The unshaded phases are continuum-like with $|\cos\theta| = 1$. The shaded (pink) phases violate CP with

$$|n_3| = 1, \quad \cos\theta = \frac{\widehat{m}_q}{2(c_\ell \hat{\epsilon}_q^2 - w')}. \tag{3.8}$$

The boundaries between continuum-like and CP-violating phases lie along the lines $|\widehat{m}_q| = 2(c_\ell \hat{\epsilon}_q^2 - w')$, and are second order transitions. The boundary between the two continuum-like phases with opposite $\cos\theta$ is a first order transition. Within the continuum-like phases the pion masses are

$$m_{\pi^0}^2 = |\widehat{m}_q| - 2(c_\ell \hat{\epsilon}_q^2 - w') , \quad m_{\pi^\pm}^2 = |\widehat{m}_q| + 2w' , \tag{3.9}$$

while within the CP-violating phase

$$m_{\pi^0}^2 = 2(c_\ell \hat{\epsilon}_q^2 - w') \sin^2\theta , \quad m_{\pi^\pm}^2 = 2 c_\ell \hat{\epsilon}_q^2 . \tag{3.10}$$

The neutral pion mass vanishes along the second order transition lines. Plots of these masses are given in Ch. 2.

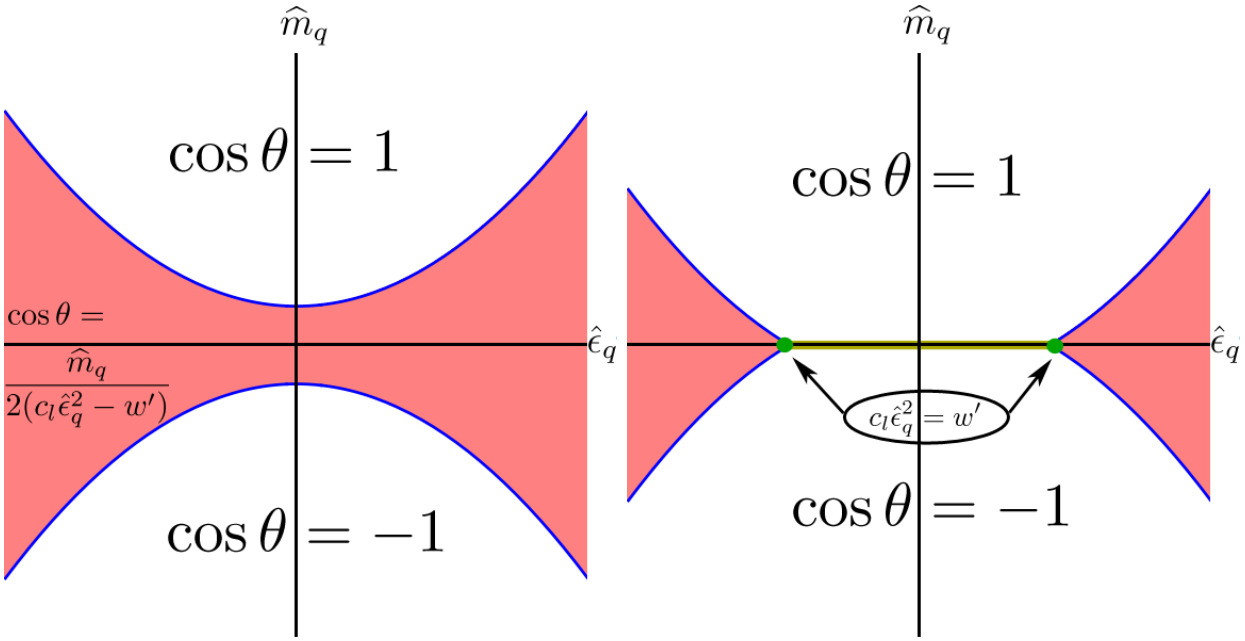


(a) Aoki scenario ($w' < 0$). (b) First-order scenario ($w' > 0$).

Figure 3.1: Phase diagrams adapted from Fig. 2.5 including effects of both discretization and nondegenerate quarks. CP is violated in the (pink) shaded regions. The (blue) lines at the boundaries of the shade regions are second-order transitions (where the neutral pion mass vanishes), while the (yellow) line along the $\epsilon_q$ axis joining the two shaded regions in (4.2b) is a line of first order transitions. The analytic expression given for the shaded region in (4.2a) holds also for that in (4.2b). As discussed below in Sec. 3.3.2, these phase diagrams apply also in the presence of electromagnetism.

### *3.3 Charged, nondegenerate Wilson quarks*

We now add electromagnetism, so that we are considering Wilson fermions with charged, nondegenerate quarks. Precisely how electromagnetism is added at the lattice level is not relevant; all we need to know is that electromagnetic gauge invariance is maintained by coupling to exact vector currents of the lattice theory. We work here only at LO in $\alpha_{\rm EM}$, which in terms of Feynman diagrams means keeping only those with a single photon propagator. We

also work at infinite volume, thus avoiding the complications of power-law volume dependence that occur in simulations [37, 21, 14].

### *3.3.1 Induced shifts in quark masses*

The dominant effect of electromagnetism is a charge dependent shift in the critical mass, as noted in Refs. [48, 23, 14]. Here we discuss this shift from the viewpoint of the Symanzik low-energy effective Lagrangian [62, 63]. It arises from QCD self-energy diagrams in which one of the gluons is replaced by a photon, and leads to the appearance of the operators

$$\begin{aligned}
&(a)\frac{\alpha_{\rm EM}}{a}(\sum_f e_f^2 \overline{f} f)\,, \\
&(b)\frac{\alpha_{\rm EM}}{a}(\sum_{f'} e_{f'}) \sum_f e_f \overline{f} f\,, \\
&(c)\frac{\alpha_{\rm EM}}{a}\sum_{f'}(e_{f'}^2) \sum_f \overline{f} f\,,
\end{aligned} \tag{3.11}$$

where $f = u, d$, $e_u = 2/3$ and $e_d = -1/3$. Examples of the corresponding Feynman diagrams are shown in Fig. 3.2

These operators are allowed because electromagnetism breaks isospin, while Wilson fermions violate chiral symmetries. Their contributions are smaller than those of the $\sum_f \bar{f} f/a$ operator that leads to the dominant shift in the critical mass. However, because $\alpha_{\rm EM} \sim a^2 \sim m$ in our power-counting, $\alpha_{\rm EM}/a$ effects are proportional to $a \sim m^{1/2}$, and thus dominate over physical quark masses. They must therefore be removed by appropriate tuning of the bare masses. Since the combined effect of the three operators is independent $\mathcal{O}(\alpha_{\rm EM}/a)$ shifts in $m_u$ and $m_d$, removing these shifts requires independent tuning of the $u$ and $d$ critical masses.

Different methods for doing this tuning have been used in the literature. The most straightforward, used in Ref. [14], is to determine the bare quark masses directly by enforcing that an appropriate subset of hadron masses agree with their experimental values (keeping all isospin breaking effects). This avoids the need to directly determine the critical masses, but is the most challenging numerically. An alternative approach, proposed in Ref. [23],

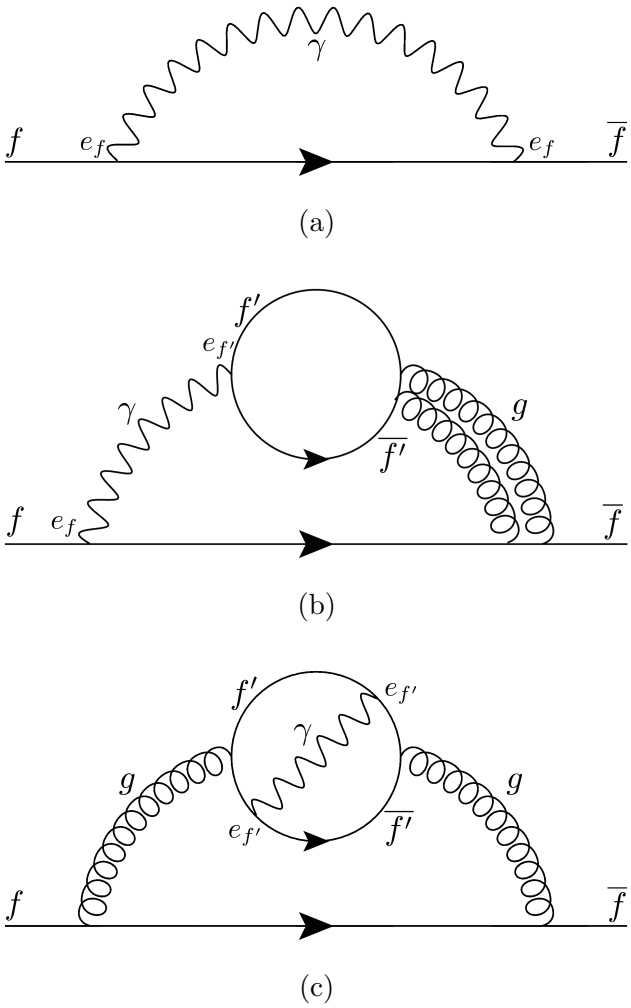


Figure 3.2: Examples of LO contributions from electromagnetism to quark self-energies. Diagrams with additional gluons and quark loops are not shown. These three types of diagram lead, respectively, to the three operators listed in Eq. 3.11. Only the first operator is present in the "electroquenched" approximation.

makes use of a partially-quenched extension of the theory. In Appendix A.2 we check this method by showing how it can be implemented in $\chi$PT. We find that it cannot determine both critical masses, but instead only provides a single constraint between them. We then introduce an additional tuning criterion which, together with that of Ref. [23], does allow both critical masses to be determined.

For the rest of the main text, we assume that the charge-dependent critical masses have been determined in some manner, such that $\mathcal{O}(\alpha_{\rm EM}/a)$ self-energy effects can be ignored. This leaves electromagnetic corrections proportional to $\alpha_{\rm EM}$, which we must keep in our power counting, as well as higher-order effects proportional to $\alpha_{\rm EM} \times m$ etc., which we can ignore.

Examples of the latter effects are the bilinears

$$\alpha_{\rm EM} \sum_f e_f^2 m_f \bar{f} f \quad \text{and} \quad \alpha_{\rm EM} \sum_f e_f^2 \bar{f} \not{D} f \,. \tag{3.12}$$

These arise as $\mathcal{O}(am)$ corrections to the operators of Eq. (3.11), and are also present directly in the continuum theory. We stress that, in the Symanzik Lagrangian, one has no dimensionful parameters other than $m$ and $1/a$, so bilinears proportional to $\alpha_{\rm EM}\Lambda_{\rm QCD}$ are not allowed. Factors of $\Lambda_{\rm QCD}$ arise when we move from the Symanzik Lagrangian to $\chi$PT.

The only effect of electromagnetism that is simply proportional to $\alpha_{\rm EM}$—and thus of LO in our power counting—is that arising from one photon exchange between electromagnetic currents. This is a continuum effect, long studied in $\chi$PT. It leads to he following additional term in the chiral potential [35, 26]:[7]

$$\mathcal{V}_{\rm EM} = -\frac{f^2}{4} c_{\rm EM} \,\mathrm{tr}(\Sigma \tau_3 \Sigma^\dagger \tau_3) \,. \tag{3.13}$$

Here $c_{\rm EM}$ is an unknown coefficient proportional to $\alpha_{\rm EM}$. All that is known about $c_{\rm EM}$ is that it is positive [66].

[7] Contributions from the isoscalar part of the photon coupling lead to the same form but with one or both $\tau_3$'s replaced by identity matrices. In either case the contribution reduces to an uninteresting constant, and is thus not included in $\mathcal{V}_{\rm EM}$.

### *3.3.2 Phase diagram and pion masses*

The competition between electromagnetic effects and discretization errors for two *degenerate* Wilson fermions has been previously analyzed in Ref. [34]. Here we add in the effects of nondegeneracy. This turns out to be very simple. Using the SU(2) identity

$$4\,\mathrm{tr}(\Sigma\tau_3\Sigma^\dagger\tau_3) = \left[\mathrm{tr}(\Sigma{+}\Sigma^\dagger)\right]^2 - \left[\mathrm{tr}([\Sigma{-}\Sigma^\dagger]\tau_3)\right]^2 - 8, \tag{3.14}$$

together with

$$\chi = \widehat{m}_q \mathbb{1} + \hat{\epsilon}_q \tau_3\,, \tag{3.15}$$

we find that $\mathcal{V}_{\rm EM}$ can be absorbed into $\mathcal{V}_\chi$ [given in Eqs. (4.2) and (3.5)] by changing the existing constants as

$$w' \longrightarrow w' + c_{\rm EM}\,, \quad \text{and} \quad c_\ell \hat{\epsilon}_q^2 \longrightarrow c_\ell \hat{\epsilon}_q^2 + c_{\rm EM}\,. \tag{3.16}$$

This allows us to determine the phase diagram and pion masses directly from the results presented in the previous section.[8]

We first observe that, at the order we work, the phase diagram is *unchanged by the inclusion of EM*—the results in Fig. 3.1 still hold. This can be seen from the form of the potential in Eq. (3.5), which, since $|n_3| = 1$, depends only on $c_\ell \hat{\epsilon}_q^2 - w'$. This combination is, however, unaffected by the shifts of Eq. (3.16) and so the phase boundaries and values of $\theta$ throughout the phase plane are also unchanged.

Similarly, from Eqs. (3.9) and (3.10) we see that the neutral pion masses are unchanged throughout the phase plane. In particular, the second-order phase boundaries are (as expected) lines along which the neutral pion is massless.

The only change caused by electromagnetism is to the charged pion masses, which are increased by the same amount throughout the phase plane:

$$m_{\pi^\pm}^2 \longrightarrow m_{\pi^\pm}^2 + 2c_{\rm EM}\,. \tag{3.17}$$

[8] For $\hat{\epsilon}_q = 0$ our results are in complete agreement with those of Ref. [34].

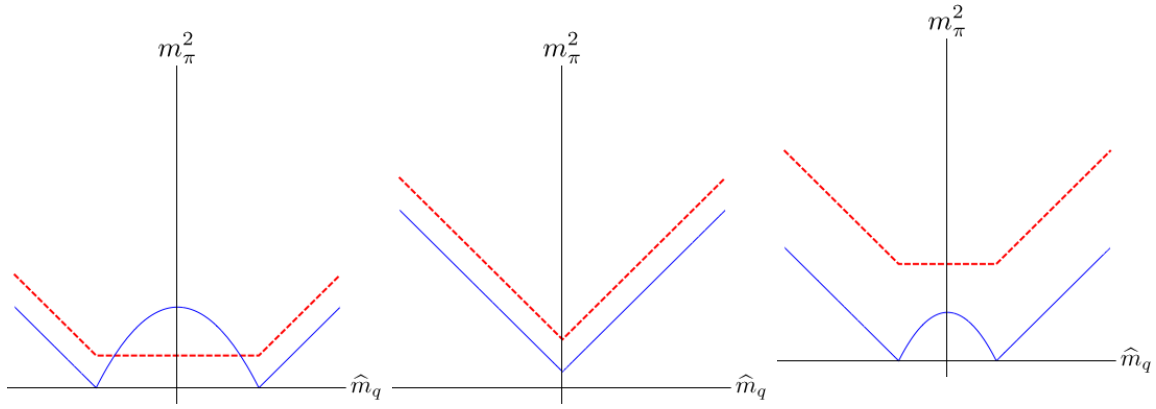


(a) Aoki scenario with $w' < -c_{\mathrm{EM}}$

(b) First-order scenario with $w' > c_\ell \hat{\epsilon}_q^2$

(c) First-order or Aoki scenario with $-c_{\mathrm{EM}} < w' < c_\ell \hat{\epsilon}_q^2$

Figure 3.3: Pion masses for nondegenerate untwisted Wilson fermions including electromagnetism. The three possible behaviors along vertical slices through phase diagrams of Fig. 3.1 are shown. Solid (blue) lines show $m_{\pi^0}^2$, while dashed (red) lines show $m_{\pi^\pm}^2$. Expressions for masses are given in the text.

One implication is that, for $\hat{\epsilon}_q = 0$, the charged pions are no longer massless within the Aoki phase (if present). This is because they are no longer Goldstone bosons, as the flavor symmetry is explicitly broken by electromagnetism. Also, as noted in Ref. [34], the charged pion can be lighter than the neutral one inside the CP-violating phases. This is not inconsistent with Witten's identity [66] because the latter did not account for discretization effects. Plots of the pion masses are shown in Fig. 3.3.

It is perhaps surprising that electromagnetism, which contributes at LO in our power-counting, has no effect on the phase diagram, whereas the subleading contributions proportional to $\hat{\epsilon}_q^2$ have a significant impact. We can understand this by noting that the CP-violating phase is characterized by a neutral pion condensate, which remains uncoupled to the photon until higher order in $\chi$PT (where form factors enter).

The implications of these results for practical simulations (such as those of Ref. [14])

are unchanged from the discussion in Ch. 2. In particular, for the Aoki scenario ($w' < 0$) discretization effects move the CP-violating phase closer to the physical point than for degenerate quarks, so one must beware of simulating too close to this transition.

### *3.4 Nondegeneracy, electromagnetism and twist*

When using twisted-mass fermions one must decide on the relative orientation in isospin space both of the twist and the isospin-breaking induced by quark mass differences and electromagnetism. In the absence of electromagnetism, the standard choice is to align these two effects in orthogonal directions. For example, one usually takes $\tau_3$ for isospin-breaking, as in the continuum, while twisting in the $\tau_1$ direction.[9] This is the choice used in simulations of the strange-charm sector using twisted-mass fermions [8]. It ensures that the fermion determinant is real, and (subject to some conditions) positive [29]. This was the choice whose phase structure we determined using W$\chi$PT in Ch. 2.

This approach does not, however, allow for the inclusion of electromagnetism. One problem is apparent already in the continuum limit, where the twisted-mass quark action is (in the "twisted" basis) [30]

$$\overline{\psi}(\not{D} + m_q c_\omega + i\gamma_5\tau_1 m_q s_\omega + \epsilon_q\tau_3)\psi\,. \tag{3.18}$$

Here $\not{D}$ is the gluonic covariant derivative, $m_q$ is the average quark mass, and $\omega$ the twist angle with $c_\omega = \cos\omega$ and $s_\omega = \sin\omega$. This action is not invariant under flavor rotations in the $\tau_3$ direction, so there is no conserved vector current to which the photon can couple. In other words, there is no global flavor transformation available to gauge.

To avoid this problem, we recall that twisting is, in the continuum, simply a nonanomalous change of variables that does not effect physical quantities. Thus we should start with the standard action including electromagnetism

$$\overline{\psi}(\not{D} - ie\not{A}Q + m_q + \epsilon_q\tau_3)\psi\,, \tag{3.19}$$

[9] Any linear combination of $\tau_1$ and $\tau_2$ is equivalent; $\tau_1$ is the standard choice.

with $A_\mu$ the photon field coupling via the charge matrix

$$Q = \frac{1}{6}\mathbb{1} + \frac{1}{2}\tau_3\,, \tag{3.20}$$

and then perform a chiral twist

$$\psi \longrightarrow e^{i\omega\gamma_5\tau_1/2}\psi, \quad \overline{\psi} \longrightarrow \overline{\psi}e^{i\omega\gamma_5\tau_1/2}\,. \tag{3.21}$$

This leads to the quark action of Eq. (3.18) with the addition of the photon coupling

$$\overline{\psi}\not{A}\left[\frac{1}{6}\mathbb{1} + \frac{1}{2}(c_\omega\tau_3 - s_\omega\tau_2\gamma_5)\right]\psi\,. \tag{3.22}$$

Thus the photon couples to a linear combination of vector currents and to an axial current in the $\tau_2$ direction. In the continuum, this combination is conserved [given the twisted mass matrix of Eq. (3.18)] and the action remains gauge invariant.

We conclude that the correct fermion action to discretize is the sum of Eqs. (3.18) and (3.22). This, however, is not possible in a gauge invariant way using Wilson's lattice derivative (except for $s_\omega = 0$). The Wilson term breaks all axial symmetries, so the $\tau_2\gamma_5$ part of the photon coupling is to a lattice current that is not conserved.

To avoid this problem, and obtain a discretized twisted theory that maintains gauge invariance, one needs to twist in a direction that leaves the photon coupling to a conserved current. The only choice is to twist in the $\tau_3$ direction. Then the twisted form of the continuum Lagrangian is

$$\overline{\psi}(\not{D} - ie\not{A}Q + m_q c_\omega + \tau_3\epsilon_q c_\omega + i\gamma_5\tau_3 m_q s_\omega + i\gamma_5\epsilon_q s_\omega)\psi\,. \tag{3.23}$$

This is discretized by adding the standard Wilson term. Since the photon is coupled to vector currents that are exact symmetries of both the Wilson term and the full mass matrix, gauge invariance is retained.

This form of the twisted isospin-violating action (with $\omega = \pi/2$) is used in the recent work of Refs. [22, 23]. It has one major practical disadvantage—the quark determinant is complex for nonzero twist. This is true for nondegenerate masses alone, as explained in Ref. [65].

Adding electromagnetism only makes the problem worse, since at the least it induces further nondegeneracy in the masses. Because the action is complex, direct simulation with present fermion algorithms is challenging. This problem is avoided in Refs. [22, 23] by doing a perturbative expansion in powers of $\epsilon_q$ and $\alpha_{\rm EM}$. The expectation values are then evaluated in the theory with no isospin breaking, for which the fermion determinant with twisting is real and positive.

In the following section we study the phase diagram of the theory with the discretized form of the Lagrangian (4.5). To our knowledge, this form of the twisted theory has not previously been studied in W$\chi$PT either with nondegeneracy alone or with electromagnetism.

### *3.5 $\chi$PT for charged, nondegenerate quarks with a $\tau_3$ twist*

The conclusion of the previous section is that the twisted-mass theory whose phase diagram is of interest is that with lattice fermion Lagrangian

$$\overline{\psi}_L \left[ D_W + m_0 + \tau_3 \epsilon_0 + i\gamma_5 \tau_3 \mu_0 + i\gamma_5 \eta_0 \right] \psi_L \,. \tag{3.24}$$

$\psi_L$ is a lattice fermion field and $D_W$ the lattice Dirac operator including the Wilson term (and possibly improved). $D_W$ is coupled to both gluons and photons, with the latter coupling to the $\tau_3$ vector current. The action differs from that considered (implicitly) in Sec. 3.3 only by the addition of the two mass parameters $\mu_0$ and $\eta_0$.

The four bare mass parameters in (3.24) are related in the continuum limit to the renormalized up and down masses, the twist angle (which is a redundant parameter) and the QCD theta angle, $\theta_{\rm QCD}$. The aim is to tune the bare parameters so that the dimension 4 part of the quark contribution to the Symanzik effective Lagrangian is given by Eq. (4.5) with the desired physical quark masses, for some choice of $\omega$. As for untwisted Wilson fermions the dominant effect of electromagnetism is to cause separate $\mathcal{O}(\alpha_{\rm EM}/a)$ shifts in the (untwisted) up and down masses. These shifts depend on twisted masses only at quadratic order, so that, to the order we work, they are identical to those for Wilson fermions. They can be determined by the methods discussed in Sec. 3.3.1 and Appendix A.2. They are equivalent

to independent shifts in $m_0$ and $\epsilon_0$.

After the additive shift in $m_0$ and $\epsilon_0$, all four masses in (3.24) must be multiplicatively renormalized in order to be related to the continuum masses in Eq. (4.5). As discussed in Appendix A.1, this requires different renormalization factors for all four masses. We assume here that these renormalizations have been carried out, so that the dimension four term in the Symanzik effective Lagrangian is given by Eq. (4.5) and described by the three parameters $m_q$, $\epsilon_q$ and $\omega$.

We stress that this tuning and renormalization must be carried out with sufficient accuracy. If not, instead of Eq. (4.5), one ends up with a similar form having *different* twist angles for the $m_q$ and $\epsilon_q$ parts. The parity-odd parts can then only be removed by a combined flavor nonsinglet and flavor singlet twist. Since the latter is anomalous, this corresponds to a theory with nondegenerate quark masses, electromagnetism, a twist angle *and* a nonvanishing $\theta_{\rm QCD}$. In other words, the theory not only has the unphysical parity violation due to twisting (which can be rotated away in the continuum limit) but also the physical parity violation induced by $\theta_{\rm QCD}$. Indeed, to analyze the tuning in $\chi$PT one needs to include a nonvanishing $\theta_{\rm QCD}$, an analysis we carry out in Chapter 4.

Assuming that the dimension-four quark Lagrangian is Eq. (4.5), we next investigate which higher-dimension operators are introduced into the Symanzik Lagrangian by twisting. Those operators present for Wilson fermions remain, but, as discussed in Sec. 3.3, are all of higher order than we consider. The dominant operators introduced by twisting will violate parity, because they are linear in the parity-violating mass terms $\mu_0$ and $\eta_0$. Examples of the new operators are[10]

$$a\eta_0 G_{\mu\nu}\widetilde{G}_{\mu\nu}\,,\ a\eta_0\overline{\psi}\widetilde{G}_{\mu\nu}\sigma_{\mu\nu}\psi\,,\ \text{and}\ a\mu_0\overline{\psi}\tau_3\widetilde{G}_{\mu\nu}\sigma_{\mu\nu}\psi\,. \tag{3.25}$$

Since we generically treat $am$ terms as being beyond LO$^+$ [see Eq. (3.1)], we should be able to ignore these operators. However, because $\eta_0 \sim \epsilon_q$ and we are treating $\epsilon_q$ as somewhat

[10]The first of these corresponds to an induced value of $\theta_{\rm QCD}$ proportional to $a\eta_0$. This is one way of seeing that the lattice action (3.24) leads to a complex fermion determinant.

enhanced, one might be concerned about dropping $a\eta_0$ terms. In fact, the $a\eta_0$ operators in (3.25), when matched into $\chi$PT, pick up an additional factor of $m$ or $p^2$, and thus are unambiguously suppressed. The reason for the extra factors is that the LO representation of a flavor-singlet pseudoscalar in $\chi$PT, $\mathrm{tr}(\Sigma - \Sigma^\dagger)$, vanishes identically. For the induced $\theta_{\mathrm{QCD}}$ term, one can also see this result by noting that it can be rotated into the isosinglet mass term, leading to a contribution proportional to $m\theta_{\mathrm{QCD}} \sim a\epsilon m$.

Proceeding in this fashion, we find that all other new operators induced by the parity-breaking masses are beyond $\mathrm{LO}^+$ in our power counting. Thus, once the requisite tuning has been done, the $\mathrm{LO}^+$ chiral effective theory for $\tau_3$ twisted fermions with isospin breaking is given by the same result as for Wilson fermions, i.e.

$$\frac{f^2}{4}\,\mathrm{tr}\left[\partial_\mu \Sigma \partial_\mu \Sigma^\dagger\right] + \mathcal{V}_\chi + \mathcal{V}_{\mathrm{EM}} \tag{3.26}$$

[see Eqs. (4.2) and (4.4)], except that the quark mass matrix is now twisted

$$\chi = (\widehat{m}_q + \hat{\epsilon}_q \tau_3) e^{i\omega\tau_3}\,. \tag{3.27}$$

We analyze the phase structure of this chiral theory in the next two subsections.

### *3.5.1 Phase diagram and pion masses at maximal $\tau_3$ twist*

We begin working at maximal $\tau_3$ twist, which is the choice used in Refs. [22, 23]. In this case

$$\chi = i\widehat{m}_q \tau_3 + i\hat{\epsilon}_q\,, \tag{3.28}$$

and the chiral potential becomes

$$-\frac{\mathcal{V}_{\chi+\mathrm{EM}}}{f^2} = \widehat{m}_q n_3 \sin\theta - (c_\ell \hat{\epsilon}_q^2 + w')\sin^2\theta + c_{\mathrm{EM}}(\cos^2\theta + n_3^2 \sin^2\theta)\,, \tag{3.29}$$

up to an irrelevant constant. Since $c_{\mathrm{EM}} > 0$, the right-hand side is maximized always with $|n_3| = 1$, and we see that the $c_{\mathrm{EM}}$ term becomes a constant. Thus, once again, electromagnetism has no impact on the phase diagram. We also see that the effect of nondegeneracy

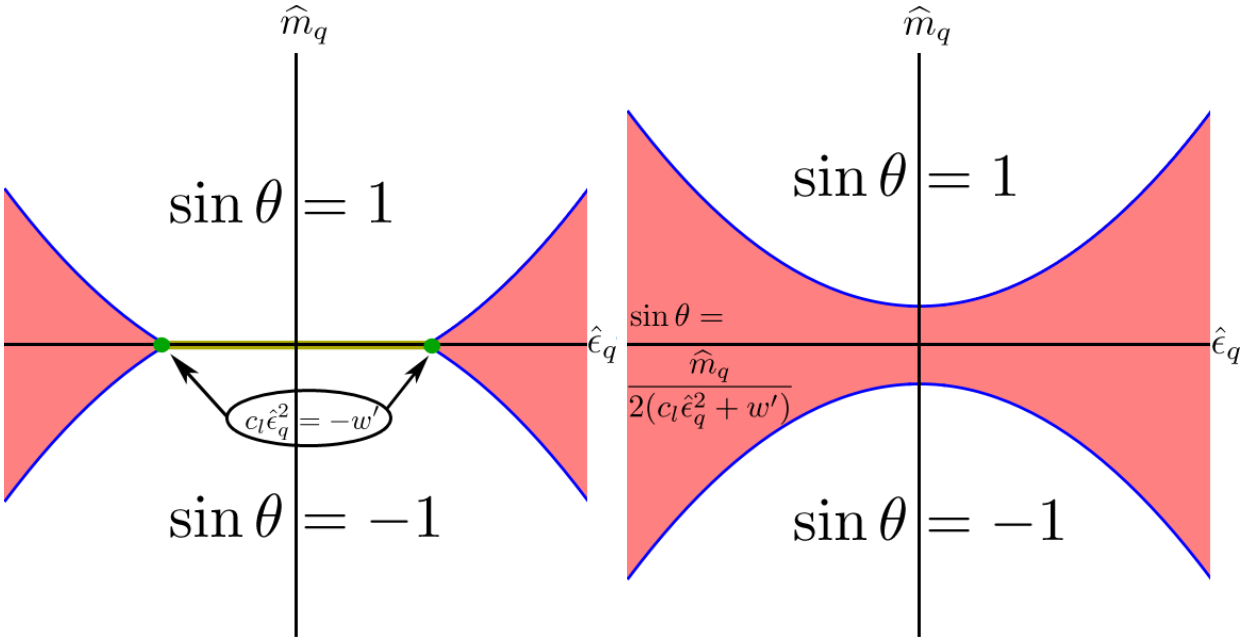


(a) Aoki scenario ($w' < 0$). (b) First-order scenario ($w' > 0$).

Figure 3.4: Phase diagrams including effects of discretization and nondegeneracy for maximally $\tau_3$-twisted quarks. Electromagnetism has no impact on the phase diagram. Notation as in Fig. 3.1. The neutral pion is massless along the second-order phase boundary between shaded (CP-violating) and unshaded phases.

can be deduced from the results for the degenerate case (studied in Refs. [45, 52, 57]) simply by shifting $w'$.

The resulting phase diagrams are shown in Fig. 3.4. Comparing to the untwisted results of Fig. 3.1, we see that the role of the Aoki and first-order scenarios has interchanged. Without loss of generality, we can take $n_3 = 1$ throughout the phase plane. Then, in the continuum-like (unshaded) phases we have $\sin\theta = \text{sign}(\widehat{m}_q)$, corresponding to the condensate aligning or antialigning with the applied twist. Second order transitions occur at $|\widehat{m}_q| = 2(w' + c_\ell\hat{\epsilon}_q^2)$. For smaller values of $|\widehat{m}_q|$ the condensate angle is $\sin\theta = \widehat{m}_q/(2[w' + c_\ell\hat{\epsilon}_q^2])$, with two degenerate minima having opposite signs of $\cos\theta$. If one switches to the "physical basis" in which the

twist is put on the Wilson term, then one finds that this phase violates CP, just as in the Wilson case.

These results differ significantly from the phase structure for nondegenerate quarks with a maximal $\tau_1$ twist, shown in Fig. 2.7. In particular, an additional phase found for $w' > 0$ with a $\tau_1$ twist is absent here. We stress again that only the theory with a $\tau_3$ twist, i.e. that discussed here, can incorporate electromagnetism.

For the pion masses we find the following results. Within the continuum-like phases we have

$$m_{\pi^0}^2 = |\widehat{m}_q| - 2(c_\ell \hat{\epsilon}_q^2 + w')\,, \quad m_{\pi^\pm}^2 = |\widehat{m}_q| + 2c_{\rm EM}\,, \tag{3.30}$$

while within the CP-violating phase

$$m_{\pi^0}^2 = 2(c_\ell \hat{\epsilon}_q^2 + w')\cos^2\theta\,, \quad m_{\pi^\pm}^2 = 2(c_\ell \hat{\epsilon}_q^2 + w' + c_{\rm EM})\,. \tag{3.31}$$

As expected, only the charged pion masses are affected by electromagnetism. Plots of these results along vertical slices through the phase diagram are shown in Fig. 3.5.

It is interesting to compare to the results with untwisted fermions, which are given in Eqs. (3.9) and (3.10) together with the shift (3.17) of $m_{\pi^\pm}^2$ by $2c_{\rm EM}$ induced by electromagnetism. We see that the neutral pion mass differs only by the change of sign of $w'$ (which also implies the interchange $\sin\theta \leftrightarrow \cos\theta$). This means that the results in the two scenarios interchange exactly. For the charged pion masses, apart from the interchange of scenarios there are also overall shifts proportional to $w'$.

The implications of these results for present simulations are as follows. If one could simulate the theory directly (somehow dealing with the fact that the action is complex) then one would need to avoid working in or near the CP-violating phase. This is now more difficult in the first-order scenario than the Aoki scenario—opposite to the situation with untwisted Wilson fermions. This qualitative result is the same as for $\tau_1$ twisting (without electromagnetism), although the area taken up by unphysical phases is larger in that case. As noted above, actual simulations done to date at maximal twist use perturbation theory in $\hat{\epsilon}_q$ and $\alpha_{\rm EM}$, and so evaluate all expectation values in the theory with $\hat{\epsilon}_q = \alpha_{\rm EM} = 0$.

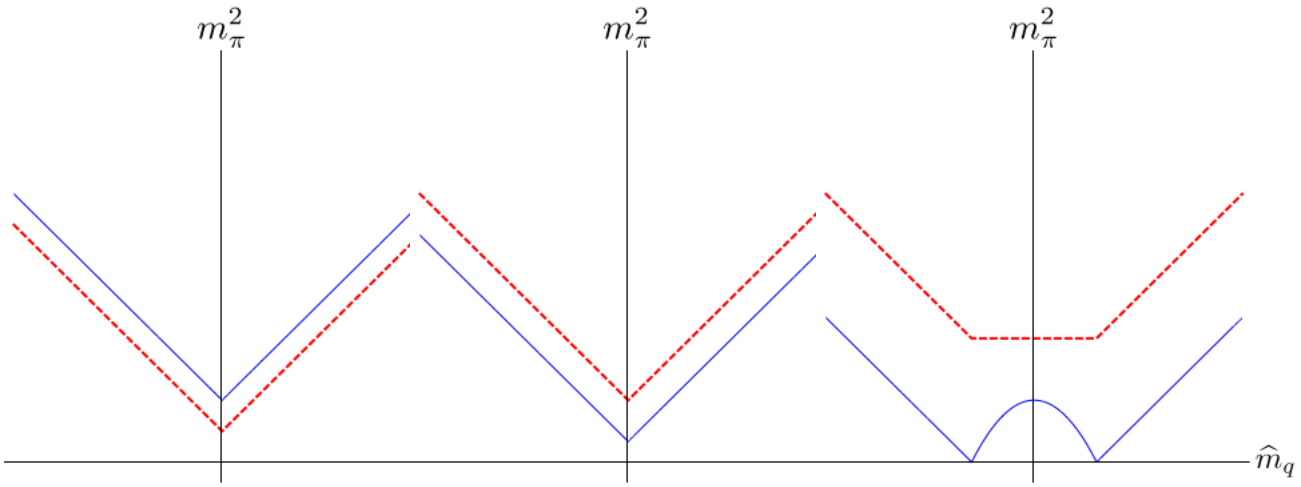


(a) Aoki scenario with $c_\ell \hat{\epsilon}_q^2 + w' < -c_{\rm EM} < 0$

(b) Aoki scenario with $-c_{\rm EM} < c_\ell \hat{\epsilon}_q^2 + w' < 0$

(c) Aoki or first-order scenario with $c_\ell \hat{\epsilon}_q^2 + w' > 0$

Figure 3.5: Pion masses for nondegenerate maximally $\tau_3$-twisted fermions including electromagnetism. The three possible behaviors along vertical slices through phase diagrams of Fig. 3.4 are shown. Solid (blue) lines show $m_{\pi^0}^2$, while dashed (red) lines show $m_{\pi^\pm}^2$. Expressions for masses are given in the text.

Clearly, if $w' > 0$, these simulations must be careful to have $\hat{m}_q$ large enough to avoid the CP-violating phase.[11]

### *3.5.2 Nonmaximal $\tau_3$ twist*

We have also investigated the phase structure for general $\tau_3$ twist, i.e. nonvanishing and nonmaximal. One motivation for doing so is that twisted-mass simulations cannot achieve exactly maximal twist; another is to see how the phase diagrams of Fig. 3.1 change into those of Fig. 3.4.

Expressions are simplified if we define $\theta$ relative to a twist $\omega$, i.e. if we use

$$\langle \Sigma \rangle = e^{i\omega\tau_3/2} e^{i\theta\hat{n}\cdot\vec{\tau}} e^{i\omega\tau_3/2} \,. \tag{3.32}$$

Then we find (dropping constants)[12]

$$\begin{aligned} -\frac{\mathcal{V}}{f^2} &= \widehat{m}_q \cos\theta + c_\ell \hat{\epsilon}_q^2 n_3^2 \sin^2\theta + w'(\cos\theta\cos\omega - n_3 \sin\theta \sin\omega)^2 \\ &\quad + c_{\rm EM}(\cos^2\theta + n_3^2 \sin^2\theta) \,. \end{aligned} \tag{3.33}$$

This is not amenable to simple analytic extremization, and we have used a mix of analytic and numerical methods. One can show analytically that the minima always occur at $|n_3| = 1$. This implies that, once again, the electromagnetism does not play a role in determining the phase structure.

The sign of $n_3$ can always be absorbed into $\theta$, so we can again choose $n_3 = 1$ without loss of generality. The potential can then be written (up to $\theta$-independent terms) as

$$-\frac{\mathcal{V}}{f^2}\bigg|_{n_3=1} = \widehat{m}_q \cos\theta + \cos^2\theta \left[-c_\ell \hat{\epsilon}_q^2 + w' \cos(2\omega)\right] - \frac{w'}{2} \sin(2\theta)\sin(2\omega) \,. \tag{3.34}$$

---

[11] In addition, if these simulations are done close to the onset of the CP-violating phase, one would expect the expansion in $\hat{\epsilon}_q$ to be poorly convergent. This is probably not a problem for the method of Ref. [30], however, since they take the continuum limit of the term linear in $\hat{\epsilon}_q$, and in this limit $w' = 0$ and the lattice artifacts discussed here vanish.

[12] At $\omega = \pi/2$ this should agree with Eq. (3.29), and it does once the different definitions of $\theta$ and $\hat{n}$ are taken into account.

A numerical investigation of this potential finds that, for nonextremal $\omega$, and for all nonzero $w'$, there is a first-order transition as $\widehat{m}_q$ passes through zero, irrespective of the value of $\hat{\epsilon}_q$. At this transition $\theta$ jumps from $\pi/2-\delta$ to $\pi/2+\delta$, with $\delta \neq 0$ depending on the parameters. Thus, unlike at the extremal points $\omega = 0, \pi/2$, there are no second-order transition lines. Correspondingly, there are no values of the parameters for which any of the pion masses vanish. This is very different from the theory with a $\tau_1$ twist, where in Ch. 2 we found a two-dimensional critical sheet in $\widehat{m}_q, \hat{\epsilon}_q, \omega$ space.

The absence of critical lines at nonextremal twist can be understood in terms of symmetries. For $\omega = 0$ and $\pi/2$, the potential has a $\theta \to -\theta$ symmetry, and this $Z_2$ symmetry is broken by the condensate in the CP-violating phase, leading to a massless pion at the transition. For nonextremal twist, however, the potential of Eq. (3.33) has no such symmetry. Lacking this symmetry, one expects, and finds, only first-order transitions.

### *3.6 Conclusions*

This work completes our study of how isospin breaking impacts the phase structure of Wilson-like and twisted-mass fermions. The main results are the phase diagrams presented in Figs. 3.1 and 3.4, together with the corresponding pion masses. These results show how the combination of discretization errors and nondegeneracy can bring unphysical phases closer to (or further away) from the physical point.

The inclusion of electromagnetism into the analysis turns out to be very straightforward, aside from the need to introduce independent up and down critical masses. Electromagnetism has no impact on the phase diagrams at leading order, because the condensates in the CP-violating phases involve neutral pions. The only impact is to uniformly increase the charged pion masses.

We have investigated within W$\chi$PT the conditions used in Ref. [23] to determine the two critical masses in the presence of electromagnetism. We find that, unless one makes the electroquenched approximation, the two conditions are in fact not independent. To determine both critical masses one needs an additional condition, and we have presented one

possibility in Appendix A.2. Our condition requires simulating at nonzero (though small) $\theta_{\mathrm{QCD}}$, and thus will be difficult to implement in practice, but provides an existence proof that an alternative condition exists.

Our analysis has been carried out in infinite volume. For the finite volumes used in lattice simulations one might be concerned about significant finite-volume effects on the electromagnetic contributions. The impact on the results presented here, however, should be minimal. The phase diagram will remain unaffected by electromagnetism, while the shifts in critical masses are dominated by ultraviolet momenta, themselves insensitive to the volume. The only significant effect will be on electromagnetic mass shifts, with $c_{\mathrm{EM}}$ picking up an effective power-law volume dependence [37, 21, 14, 9].

### *Acknowledgments*

This work was supported in part by the United States Department of Energy grant DE-SC0011637.

# Chapter 4

# PHASE STRUCTURE WITH NONZERO $\Theta_{\rm QCD}$ AND TWISTED MASS FERMIONS [1]

## *4.1 Introduction*

In chapters 2 and 3 we determined the phase structure of two-flavor lattice QCD with Wilson and twisted-mass fermions at nonvanishing lattice spacing in the presence of the two physical sources of isospin breaking: nondegenerate up and down quarks and electromagnetism. These results are relevant for present simulations because $\mathcal{O}(a^2)$ discretization effects are of comparable size to those from isospin breaking (Here $a$ is the lattice spacing). Discretization effects can thus significantly distort the chiral condensate and lead to unphysical phase transitions.

In particular, the CP-violating phase found by Dashen in the continuum [19] can be enlarged by discretization effects, and for large enough $a$ can include the point with physical quark masses.

In Ch. 3 we found that the inclusion of electromagnetism along with twisting requires one to consider, at an intermediate stage, a lattice theory that has, in addition to isospin breaking, a nonvanishing value of $\Theta_{\rm QCD}$. We repeat the explanation of this result below. The purpose of the present note is to study the properties of this extended theory, providing results that are used in Ch. 3 to tune to the physical value, $\Theta_{\rm QCD} = 0$. We also present some results not needed in Ch. 3 so as to provide a complete picture of the parameter dependence of the phase structure.

Our analysis is carried out using SU(2) chiral perturbation theory ($\chi$PT ). Previous work has considered this theory at nonvanishing $\Theta_{\rm QCD}$ in the continuum. In particular, Refs. [61]

[1] This chapter is adapted with minimal changes from Ref. [40]

and [16] have studied the theory at $\Theta_{\rm QCD} = \pi$, elucidating the Dashen phase. In addition, Refs. [43] and [2] considered this and related theories for arbitrary $\Theta_{\rm QCD}$ in the small-volume regime, where one can use the methods of random matrix theory. In all these theories they find a Dashen phase. What our study adds to this previous work is the inclusion of the effects of working at nonvanishing lattice spacing.

We begin by recalling the essential features of SU(2) $\chi$PT including discretization effects, nondegenerate quarks, and electromagnetism, in the power counting we use in chapters 2 and 3. In this power counting, effects proportional the average light quark mass, $m_q = (m_u+m_d)/2$, are assumed comparable to those quadratic in lattice spacing,[2] and to those proportional to $\alpha_{\rm EM}$, *i.e.*, $m_q \sim a^2 \sim \alpha_{\rm EM}$. We also include in the leading-order Lagrangian the dominant term introduced by nondegeneracy, which is proportional to $\epsilon_q^2$, where $\epsilon_q = (m_u-m_d)/2$. We work to leading order in this combined power counting, so that loop effects need not be considered. Ignoring electromagnetism for now, the Lagrangian is then

$$\mathcal{L}_\chi = \frac{f^2}{4}\,\mathrm{tr}\left[\partial_\mu \Sigma \partial_\mu \Sigma^\dagger\right] + \mathcal{V}_\chi \tag{4.1}$$

$$\begin{aligned}\mathcal{V}_\chi = &-\frac{f^2}{4}\,\mathrm{tr}(\chi^\dagger\Sigma + \Sigma^\dagger\chi) - W'[\mathrm{tr}(\hat{A}^\dagger\Sigma + \Sigma^\dagger\hat{A})]^2 \\ &+ \frac{\ell_7}{16}[\mathrm{tr}(\chi^\dagger\Sigma - \Sigma^\dagger\chi)]^2\,.\end{aligned} \tag{4.2}$$

Here $\Sigma \in \mathrm{SU}(2)$ is the chiral field, $f \approx 92$ MeV and $B_0$ are the continuum leading order low energy coefficients (LECs), and $\hat{A} = 2W_0 a \mathbb{1}$ is a spurion field, with $W_0$ and $W'$ LECs introduced by discretization errors. The quark mass matrix, $M$, is contained in the convenient quantity $\chi = 2B_0 M$.[3] Matching physical quantities in continuum SU(2) and SU(3) $\chi$PT one finds

$$\ell_7 = \frac{f^2}{8B_0 m_s} \tag{4.3}$$

[2]Terms linear in $a$, if present, can, in the pion sector, be absorbed into an additive shift in the quark mass, so that the leading discretization effects relevant for the phase structure are proportional to $a^2$ [56].

[3]The detailed relationship of the masses in $M$ to the bare lattice quark masses is explained in Appendix A.1. We also note that $M$ contains only the LR projection of the full mass matrix.

where $m_s$ is the strange quark mass [31]. Thus we know that $\ell_7$ is positive.

In the continuum, the leading term induced in the chiral potential by electromagnetism is that due to one-photon exchange between electromagnetic currents [35, 26]

$$\mathcal{V}_{\rm EM} = -\frac{f^2}{4} c_{\rm EM} \, {\rm tr}(\Sigma \tau_3 \Sigma^\dagger \tau_3), \tag{4.4}$$

where $c_{\rm EM}$ is proportional to $\alpha_{\rm EM}$ and is known to be positive [66]. Electromagnetism also contributes to mass renormalization, but this is implicitly included by our use of renormalized masses in the quark mass matrix $M$. Although the quark masses depend on the renormalization scheme chosen, this dependence is canceled by that of the prefactor $B_0$, so that the product $\chi$ is independent of renormalization scheme and scale.

On the lattice, with Wilson or twisted-mass fermions, the inclusion of electromagnetism leads to additional issues. The first of these concerns the direction of the twist. Quark nondegeneracy picks out the $\tau_3$ direction in isospin space. In the absence of electromagnetism, one can twist in an orthogonal direction, e.g. $\tau_1$, and this choice leads to a real lattice fermion determinant [29]. However, such a twist leads leads to an electromagnetic current that includes an axial component when written in terms of bare quarks. This current cannot be coupled in a gauge-invariant way to the electromagnetic field in a lattice theory since it is not conserved as shown in Ch. 3.

To include both electromagnetism and nondegeneracy on the lattice, one is thus forced to twist in the $\tau_3$ direction [22, 23]. This, however, leads to a complex lattice fermion determinant [65], making the theory challenging to simulate.[4] An intuitive way of understanding why the action is complex is to note that, in the continuum, when the twist angle is $\omega$, the fermion mass term is given by

$$\overline{\psi}(m_q c_\omega + \tau_3 \epsilon_q c_\omega + i\gamma_5 \tau_3 m_q s_\omega + i\gamma_5 \epsilon_q s_\omega)\psi \,, \tag{4.5}$$

where $\psi$ is an isodoublet, $c_\omega = \cos\omega$, and $s_\omega = \sin\omega$. By construction, in the continuum a nonsinglet axial rotation (*i.e.*, a twist) can return the mass matrix to its standard form

[4] This is avoided in Refs. [22] and [23] by working to linear order in perturbation theory about the isospin symmetric theory.

$m_q + \tau_3 \epsilon_q$. However, on the lattice, such a rotation is not a symmetry. Crudely speaking, the lattice theory with mass matrix (4.5) corresponds to a continuum theory in which the coefficients of the four terms are differently renormalized. In such a theory the mass terms involving $\gamma_5$ cannot both be rotated away, and thus the theory has a nonzero $\Theta_{\rm QCD}$. As is well known, this leads to a complex fermion determinant. The only redeeming feature is that, if one could tune the lattice quark mass matrix such that it took the form of Eq. (4.5) in the continuum limit, then the imaginary part of the fermion determinant would vanish in this limit.

The situation is not this simple, however, because of the second issue induced by the inclusion of electromagnetism in the lattice theory. This is the presence of independent additive renormalizations of the up and down bare untwisted quark masses proportional to $\alpha_{\rm EM}/a$. Since in our power counting $m \sim a^2 \sim \alpha_{\rm EM}$, these renormalizations dominate over the leading order terms described above and collected in Eqs. (4.2) and (4.4). They must be tuned away by applying nonperturbative conditions to determine, independently, the two critical masses.[5] One of the results of Ch. 3 was a demonstration that the tuning method used in Ref. [23] does not work in general.[6] The method provided only a single condition, while two are needed. The key point for present purposes is that, with the untwisted parts of the quark masses "detuned", the theory one is studying has, even in the continuum limit, a nonvanishing value of $\Theta_{\rm QCD}$. Thus, to come up with a second condition that will set $\Theta_{\rm QCD} = 0$ (in the continuum limit) one must understand the properties of the detuned theory. This is the purpose of the present analysis.

To understand why detuning leads to nonzero $\Theta_{\rm QCD}$, it is instructive to write out the

---

[5]There is, in addition, the standard additive renormalization proportional to $1/a$ (times powers of $\alpha_s$) that is common to both quarks. The nonperturbative conditions that remove the $\alpha_{\rm EM}/a$ shifts will also remove the larger $1/a$ shifts. The point here is that the smaller (but still divergent) electromagnetic renormalizations imply the need for two conditions, rather than one.

[6]The method, based on introducing unphysical valence quarks, works only in the electroquenched approximation, in which sea quarks are kept neutral and degenerate. It fails once the sea quarks are charged. The second method proposed in Ref. [23], and the method used in Ref. [14], do not suffer from the same problem, because they tune using physical quantities.

renormalized mass matrix $M$ in a detuned, twisted theory. It is convenient to work with $\chi$ rather than $M$, since this is what enters the chiral Lagrangian. The form is

$$\chi = \begin{pmatrix} \widehat{m}_u^W + i\widehat{\mu}_u & 0 \\ 0 & \widehat{m}_d^W - i\widehat{\mu}_d \end{pmatrix} \tag{4.6}$$

where the "hat" on a mass indicates multiplication by $2B_0$. In particular, $\widehat{m}_u^W = 2B_0 m_u^W$, with $m_u^W$ the renormalized untwisted or "Wilson" part of the up-quark mass, while $\widehat{\mu}_u = 2B_0\mu_u$, with $\mu_u$ the twisted part of the up-quark mass. Similar notation holds for the down-quark masses. The superscript $W$ distinguishes the untwisted masses from the full physical masses, which are given, for example, by $m_u^2 = (m_u^W)^2 + \mu_u^2$. The two twisted masses in (4.6) have opposite overall signs because twisting involves $\tau_3$. In this notation, tuning the untwisted parts of both masses to their critical values means tuning both $\widehat{m}_u^W$ and $\widehat{m}_d^W$ to zero. As long as $\mu_u$ and $\mu_d$ have opposite signs this corresponds to tuning to maximal twist.

We can rewrite the mass matrix of Eq. (4.6) in terms of the average physical quark mass $m_q$ and the nondegeneracy $\epsilon_q$:

$$\chi = \begin{pmatrix} (\widehat{m}_q + \hat{\epsilon}_q)e^{i(\varphi+\omega)} & 0 \\ 0 & (\widehat{m}_q - \hat{\epsilon}_q)e^{i(\varphi-\omega)} \end{pmatrix} . \tag{4.7}$$

Here $\widehat{m}_q = 2B_0 m_q$, $\hat{\epsilon}_q = 2B_0\epsilon_q$,

$$\tan(\varphi+\omega) = \frac{\widehat{\mu}_u}{\widehat{m}_u^W} \quad \text{and} \quad \tan(\varphi-\omega) = -\frac{\widehat{\mu}_d}{\widehat{m}_d^W} . \tag{4.8}$$

We observe from Eq. (4.7) that $\omega$ is the twist angle, while $\varphi$, being the overall phase of the mass matrix, is proportional to $\Theta_{\rm QCD}$:

$$\varphi = \frac{\Theta_{\rm QCD}}{2} . \tag{4.9}$$

Thus having a general, detuned mass matrix corresponds to working at nonzero $\Theta_{\rm QCD}$. Tuning to the critical values of the untwisted quark masses corresponds to setting $\omega = \pi/2$ and $\varphi = 0$, *i.e.*, tuning to maximal twist with vanishing $\Theta_{\rm QCD}$.

In summary, the dominant effect of including electromagnetism in a theory with Wilson or twisted-mass fermions is mass renormalization. For nonvanishing twist, this implies that one must work at nonvanishing $\Theta_{\rm QCD}$ in order to tune to $\Theta_{\rm QCD} = 0$. While this will be challenging for simulations, it is straightforward to study this theory in $\chi$PT. Working at leading order in our power counting, one has simply to find the minima of the potential that is composed of the terms given in Eqs. (4.2) and (4.4).

When determining the expectation value of the chiral field, it is convenient to parametrize it relative to the twist it would obtain were $\varphi = a = 0$:

$$\langle \Sigma \rangle = e^{i\omega\tau_3/2} e^{i\theta \hat{n}\cdot\vec{\tau}} e^{i\omega\tau_3/2} \tag{4.10}$$

The full potential $\mathcal{V} = \mathcal{V}_\chi + \mathcal{V}_{\rm EM}$ then becomes

$$\begin{aligned} -\frac{\mathcal{V}}{f^2} = {} & \widehat{m}_q \cos\theta\cos\varphi + n_3\hat{\epsilon}_q \sin\theta\sin\varphi + c_\ell \left(n_3\hat{\epsilon}_q \sin\theta\cos\varphi - \widehat{m}_q\cos\theta\sin\varphi\right)^2 \\ & + w' \left(n_3\sin\theta\sin\omega - \cos\theta\cos\omega\right)^2 + c_{\rm EM}\left(n_3^2 + (1-n_3^2)\cos\theta^2\right) , \end{aligned} \tag{4.11}$$

up to an irrelevant overall constant. Here we have introduced

$$c_\ell = \frac{\ell_7}{f^2} \quad \text{and} \quad w' = \frac{64 W' W_0^2 a^2}{f^2}. \tag{4.12}$$

Given that $\ell_7$ and $c_{\rm EM}$ are both positive, the potential is always minimized with the condensate aligned in the $\tau_3$ direction, i.e. $\hat{n} = (0, 0, \pm 1)$. Without loss of generality we can set $\hat{n} = (0, 0, 1)$ and absorb any sign into $\theta$. The main task in the following is the determination of the values of $\theta$ which minimize $\mathcal{V}$ as the parameters are varied.

An immediate conclusion from this analysis is that the remaining explicit effect of electromagnetism, namely the $c_{\rm EM}$ term, is simply a constant for $n_3 = 1$. It therefore does not effect the minimization of the potential, and thus has no impact on the phase structure. Physically this is because the condensate lies in the neutral pion direction. The only effect of this term is to give an overall positive shift in the charged pion masses.[7]

[7] In light of these considerations,we drop the $c_{\rm EM}$ term in the subsequent discussion of minimization of the potential.

The remainder of this chapter is organized as follows. In Sec. 4.2 we determine the phase diagram in the $\widehat{m}_q - \hat{\epsilon}_q$ plane. We do so in stages, beginning by elucidating the symmetries of the potential (4.11), then working out the phase diagram in the continuum, next adding in discretization effects for the extremal cases where $\omega = 0$ and $\pi/2$, and finally considering the most general choices of parameters. We then return, in Sec. 4.3, to the original motivation for the present work, namely the determination of a condition such that, in the presence of electromagnetism, maximal twist at $\Theta_{\rm QCD} = 0$ can be achieved in a physical phase. We conclude in Sec. 4.4.

## *4.2 Determination of phase diagram*

### *4.2.1 Symmetries of the phase diagram*

Before entering into detailed calculations we collect some general results that follow from the form of the potential, Eq. (4.11).

First we note that, without loss of generality, we need only consider $\omega$ and $\varphi$ in the range

$$0 \leq \omega, \varphi \leq \pi/2\,, \tag{4.13}$$

as long as we consider the full $\widehat{m}_q - \hat{\epsilon}_q$ plane. This is because $\mathcal{V}$ is invariant under each of the following four transformations

$$(i)\ \{\omega \to \omega + \pi\}\,, \tag{4.14}$$

$$(ii)\ \{\omega \to -\omega,\ \theta \to -\theta,\ \hat{\epsilon}_q \to -\hat{\epsilon}_q\}\,, \tag{4.15}$$

$$(iii)\ \{\varphi \to -\varphi,\ \hat{\epsilon}_q \to -\hat{\epsilon}_q\}\,, \tag{4.16}$$

$$(iv)\ \{\varphi \to \varphi + \pi,\ \widehat{m}_q \to -\widehat{m}_q,\ \hat{\epsilon}_q \to -\hat{\epsilon}_q\}\,. \tag{4.17}$$

In the following, we refer to the endpoints of the range (4.13) as the "extremal" values of $\omega$ and $\varphi$, while values within the range are called "nonextremal".

In addition, $\mathcal{V}$ is invariant under

$$(v)\ \{\omega \to \frac{\pi}{2} - \omega,\ \varphi \to \frac{\pi}{2} - \varphi,\ \widehat{m}_q \leftrightarrow \hat{\epsilon}_q,\ \theta \to \frac{\pi}{2} - \theta\}\,. \tag{4.18}$$

This implies relations between the phase transition lines for different values of the parameters. For example, the phase diagram for $\omega = \varphi = 0$ is related to that for $\omega = \varphi = \pi/2$ by a reflection in the diagonal line $\widehat{m}_q = \hat{\epsilon}_q$.

The final invariance that plays a role in the following is

$$(vi)\ \{\omega \to \frac{\pi}{2} - \omega,\ \hat{\epsilon}_q \to -\hat{\epsilon}_q,\ w' \to -w',\ \theta \to -\theta\}\,. \tag{4.19}$$

This relates the phase diagrams with opposite signs of $w'$.

### *4.2.2 Continuum χPT with nonzero* $\Theta_{\rm QCD}$

In this section we examine the phase structure in the continuum. Without discretization effects, the twist angle is redundant and has no effect on the phase diagram. This is manifest in the basis used in Eq. (4.11), where with $w' \propto a^2 = 0$ there is no dependence on $\omega$.

We begin by recalling results for the extremal cases $\varphi = 0$ and $\pi/2$, corresponding to $\Theta_{\rm QCD} = 0$ and $\pi$. These have real and imaginary quark masses, respectively.

The physical case, $\varphi = 0$, has been described extensively in the literature [19, 17, 38]. The phase diagram is shown in Fig. 4.1(a). There is a second-order transition between the standard continuum phase and the CP-violating Dashen phase, lying along $\widehat{m}_q = \pm 2 c_\ell \hat{\epsilon}_q^2$. In the Dashen phase, the potential has two degenerate minima, both having

$$\cos\theta = \frac{\widehat{m}_q}{2 c_\ell \hat{\epsilon}_q}\,, \tag{4.20}$$

and differing in the sign of $\theta$.

The case of $\Theta_{\rm QCD} = \pi$ ($\varphi = \pi/2$) was first described by Smilga [61]. The potential has the same form as for $\varphi = 0$, except that $\widehat{m}_q$ and $\cos\theta$ are exchanged with $\hat{\epsilon}_q$ and $\sin\theta$, respectively. This implies that the phase diagram has the same form as for $\varphi = 0$, except that it is reflected in the $\widehat{m}_q = \hat{\epsilon}_q$ line, as shown in Fig. 4.1(b). This is an example of the symmetry (4.18) at work (since the change in $\omega$ is irrelevant in the continuum). There is thus a second-order transition to a Dashen-like phase along the lines $\hat{\epsilon}_q = \pm 2 c_\ell \widehat{m}_q^2$. There is again a two-fold degeneracy within this phase.

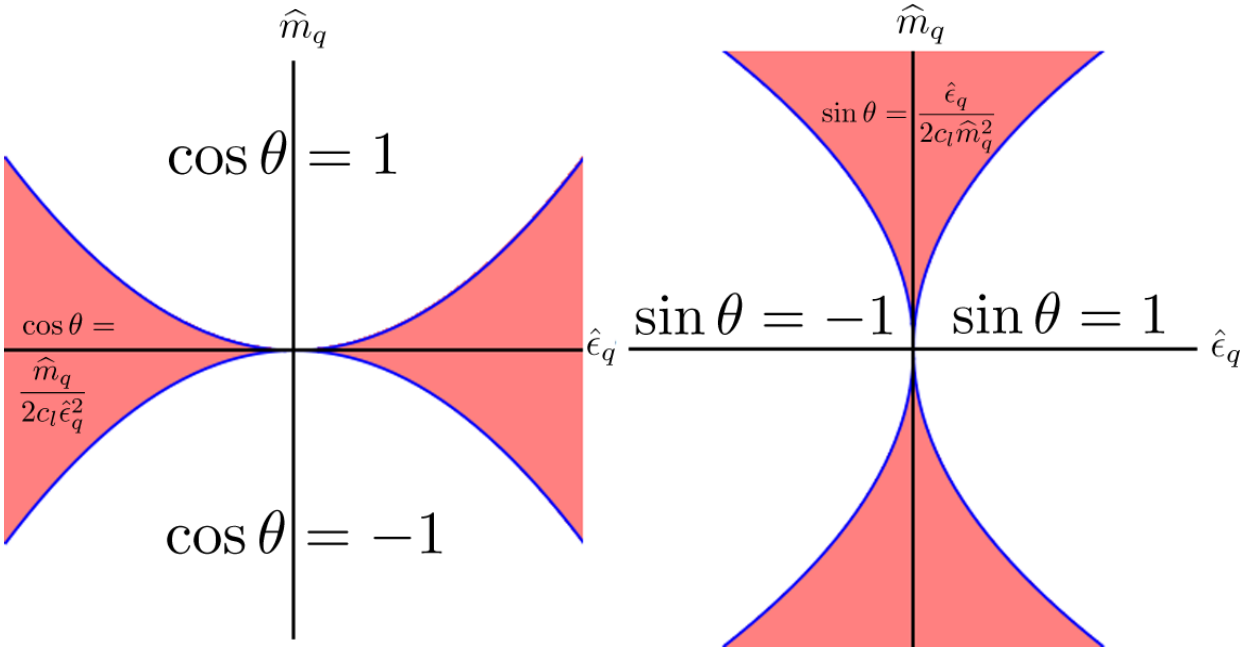


(a) $\varphi = 0$ (b) $\varphi = \pi/2$

Figure 4.1: Continuum phase diagram for (a) $\varphi = \Theta_{\rm QCD}/2 = 0$ and (b) $\varphi = \pi/2$. Shaded (pink) regions have varying values of the vacuum angle $\theta$, as indicated in the figures. Unshaded regions have constant $\theta$. The neutral pion mass vanishes along the phase transition lines.

For nonextremal $\varphi$ ($0 < \varphi < \pi/2$) the potential (4.11) cannot be minimized exactly and it is instructive to look at some simple limits.

First we drop the $\mathcal{O}(m^2)$ $c_\ell$ term. In the extremal cases this means that the width of the shaded (pink) phases shrinks to zero, so that there is a first-order transition along the entire $\widehat{m}_q = 0$ line for $\varphi = 0$ and along the $\hat{\epsilon}_q = 0$ line for $\varphi = \pi/2$. By contrast, for nonextremal $\varphi$, there are no transitions. The potential is minimized at,

$$\tan\theta = \frac{\hat{\epsilon}_q}{\widehat{m}_q}\tan\varphi\,, \tag{4.21}$$

and changes continuously as one moves through the phase diagram, except when passing through the origin.

The absence of a transition for nonextremal $\varphi$ continues to hold when the $c_\ell$ term is restored. This can be understood as due to the lack of a $Z_2$ symmetry in the potential. It is the presence of a $Z_2$ symmetry for extremal $\varphi$ (under which $\theta \to \theta + \pi$) that, when broken by the vacuum, leads to a second-order transition. The upshot is that the extremal phase diagrams of Fig. 4.1 are replaced by blank diagrams with no transitions, aside from the singular point at the origin.

To show a concrete example of this, we consider $\varphi = \pi/4$. Using the parametrization $\widehat{m}_q = r\cos\alpha$, $\hat{\epsilon}_q = r\sin\alpha$ and $r^2 = \widehat{m}_q^2 + \hat{\epsilon}_q^2$. The potential is then

$$-\frac{\mathcal{V}}{f^2} = \frac{r}{\sqrt{2}}\left[\cos(\theta-\alpha) + \kappa\cos^2(\theta+\alpha)\right]\,, \tag{4.22}$$

where $\kappa = c_\ell r/\sqrt{2}$ can be treated as small in our power counting. The minima occur when

$$0 = \sin(\theta-\alpha) + 2\kappa\sin\left[2(\theta+\alpha)\right]. \tag{4.23}$$

Expanding in powers of $\kappa$ about the leading-order solution, $\theta = \alpha$, we find

$$\theta = \alpha - 2\kappa\sin(4\alpha) + \mathcal{O}(\kappa^2)\,. \tag{4.24}$$

The presence of only a single solution indicates the absence of a Dashen-like phase. We have investigated this numerically for other values of $\varphi$ and found that there are no phase transitions for any nonextremal $\varphi$.

To see how the degeneracy of the Dashen-like phase is broken for nonextremal $\varphi$, consider the potential along the $\widehat{m}_q = 0$ axis:

$$-\frac{\mathcal{V}}{f^2} = \hat{\epsilon}_q \sin\theta \sin\varphi + c_\ell \hat{\epsilon}_q^2 \sin^2\theta \cos^2\varphi \,. \tag{4.25}$$

For $\varphi = 0$, one finds (since $c_\ell > 0$) that there are degenerate minima at $\sin\theta = \pm 1$. This corresponds to moving from the origin in Fig. 4.1(a) along the $\hat{\epsilon}_q$ axis and thus lying in the (shaded pink) Dashen phase. Turning on a nonzero $\varphi$, the potential is still extremized at $|\sin\theta| = 1$, but the two extrema are no longer degenerate

$$-\frac{\mathcal{V}(\sin\theta = \pm 1)}{f^2} = \pm\hat{\epsilon}_q \sin\varphi + c_\ell \hat{\epsilon}_q^2 \cos^2\varphi \,. \tag{4.26}$$

Thus there is a unique minimum, such that $\sin\theta = 1$ for $\hat{\epsilon}_q > 0$ and $\sin\theta = -1$ for $\hat{\epsilon}_q < 0$ (assuming a positive $\varphi$). There thus can be no Dashen-like phase.

### *4.2.3 Discretization effects at nonzero $\Theta_{\rm QCD}$ for extremal $\omega$*

We now turn on discretization errors by considering non vanishing $w'$. Just as in the continuum, the phase diagram is easiest to determine for extremal $\varphi$. The case of $\omega = \varphi = 0$ (untwisted fermions with $\Theta_{\rm QCD} = 0$) has long been studied, and it has been shown that there are two distinct scenarios depending on the sign of $w'$: the so-called Aoki scenario for $w' < 0$, and the first-order scenario for $w' > 0$ [3, 56, 38]. The resulting phase diagrams are shown in Fig. 4.2, and should be compared to the continuum diagram of Fig. 4.1(a). For $w' < 0$, the Dashen phase, in which $\theta$ is degenerate, expands vertically so as to include the origin. The CP violating phase along the $\widehat{m}_q$ axis is typically called the Aoki phase, so we call the extended CP violating region the Aoki-Dashen phase. This situation is shown in Fig. 4.2(a). For $w' > 0$, the vertical width of the continuum Dashen phase is reduced, and there is a segment of first-order transition along the $\hat{\epsilon}_q$ axis, as shown in Fig. 4.2(b). In both scenarios, within the Aoki-Dashen phases the potential is minimized by

$$\cos\theta = \frac{\widehat{m}_q}{2(c_\ell \hat{\epsilon}_q - w')} \,, \tag{4.27}$$

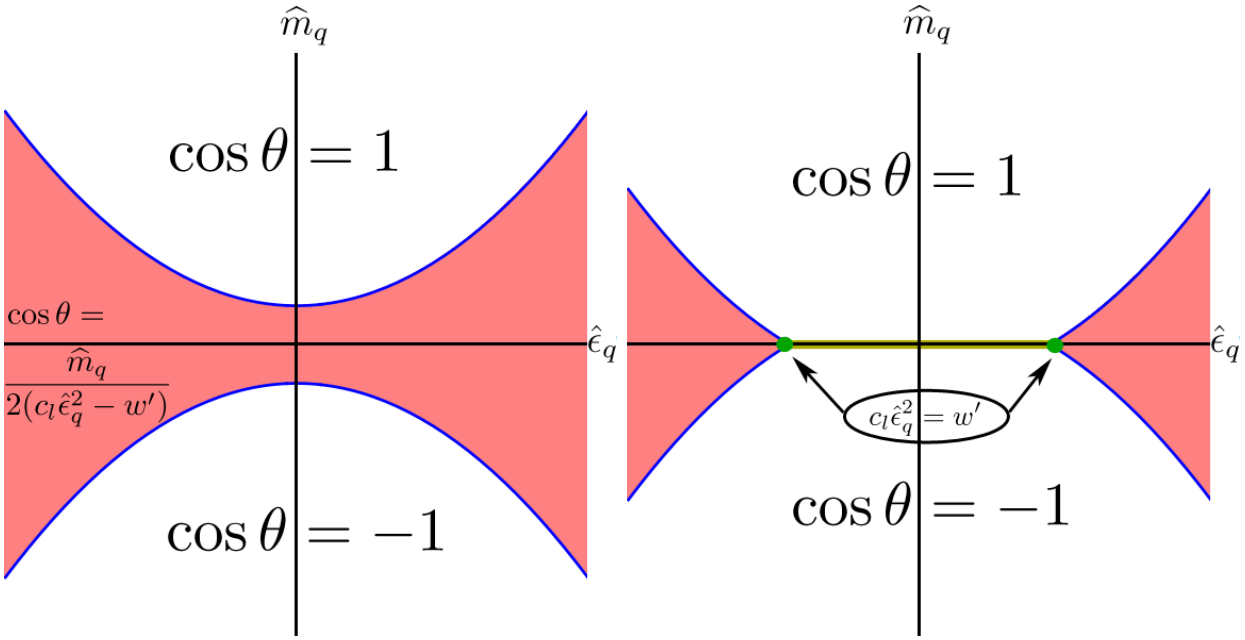


(a) $w' < 0$. (b) $w' > 0$.

Figure 4.2: Phase diagrams adapted from Fig. 2.5 including effects of discretization for $\omega = \varphi = 0$: (a) Aoki scenario ($w' < 0$) and (b) first-order scenario ($w' > 0$).. The expression for $\theta$ in the shaded (pink) region in (a) also holds in (b). The boundary of the shaded regions are second-order transition lines, along which the neutral pion mass vanishes. The (yellow) solid line running along the $\hat{\epsilon}_q$ axis between the shaded regions is a first-order transition.

so that again there are two degenerate vacua with opposite signs of $\theta$.

We next consider $\varphi = \pi/2$ while holding $\omega = 0$ (i.e. Wilson fermions at $\Theta_{\rm QCD} = \pi$). This has not been previously studied in the presence of lattice artifacts. As described above, for the continuum terms in $\mathcal{V}$, changing $\varphi$ from 0 to $\pi/2$ has the effect of interchanging $\widehat{m}_q$ and $\cos\theta$ with $\hat{\epsilon}_q$ and $\sin\theta$, respectively. Since the $w'$ term can be rewritten as $w'\cos^2\theta = w'(1-\sin^2\theta)$, the same interchanges hold for $w' \neq 0$ as long as one flips the sign of $w'$. Up to some unimportant sign flips, this is an example of the general transformation obtained by combining Eqs. (4.18) and (4.19):

$$(vii)\ \{\varphi \to \frac{\pi}{2} - \varphi,\ \widehat{m}_q \to -\hat{\epsilon}_q,\ \hat{\epsilon}_q \to \widehat{m}_q,\ w' \to -w',\ \theta \to \theta - \frac{\pi}{2}\}\,. \tag{4.28}$$

The implication is that the phase diagrams for $\varphi = \pi/2$ are obtained from those of Fig. 4.2 by rotating 90° counterclockwise, and interchanging the $w' < 0$ and $w' > 0$ scenarios. The positions of the resulting transitions are shown schematically in Fig. 4.3.

The twist angle is no longer redundant when $w' \neq 0$, entering the $w'$ term in Eq. (4.11) as $w'\cos^2(\theta+\omega)$. Thus changing $\omega$ from 0 to $\pi/2$ has the effect of flipping the sign of $w'$: $w'\cos^2(\theta+\pi/2) = w'\sin^2\theta = w'(1-\cos^2\theta)$. This is an example of the general transformation (4.19). It implies that the phase diagrams for maximal twist can be simply obtained from those without twist. The situation is summarized in Fig. 4.3.

In the remainder of this subsection we keep $\omega$ at one of the extremal values but allow $\varphi$ to take on nonextremal values. We recall that in the continuum, the phase diagram with such parameters has no phase transitions. This turns out not to be the case when $w' \neq 0$. Examples of the results we find are shown in Fig. 4.4.

We begin with $\omega = 0$ and nonextremal $\varphi$, and work in the $w' > 0$ scenario. We find that there is a first-order transition along a finite segment of the $\hat{\epsilon}_q$ axis, across which $\theta$ changes discontinuously. The length of the segment depends on $\varphi$. As $\varphi$ approaches zero [in which limit one obtains the phase diagram of Fig. 4.2(b)] the first-order segment asymptotes to precisely the first order transition line shown in Fig. 4.2(b), with end points $c_\ell \hat{\epsilon}_q^2 = \pm w'$.

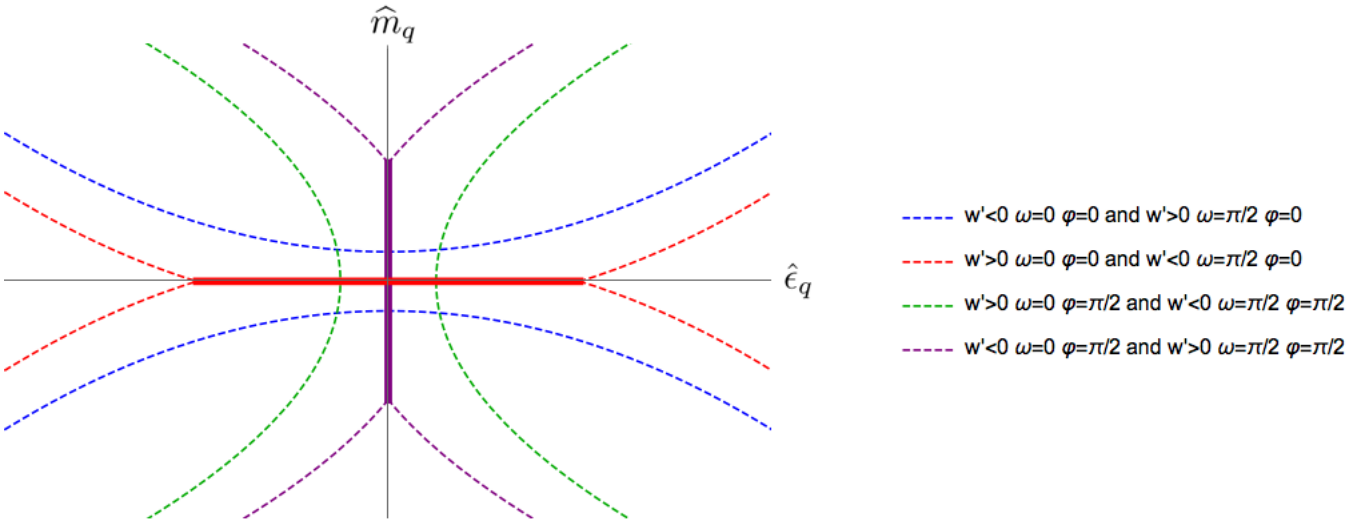


Figure 4.3: Schematic positions of phase boundaries for extremal choices of $\omega$ and $\varphi$ for both $w' < 0$ and $w' > 0$ scenarios. Dashed lines indicate second order transitions, solid lines indicate first-order transitions. Results for two of these parameter choices also appear in Fig. 4.2.

We stress again that, for non vanishing $\varphi$, there are no regions of Aoki-Dashen phase. As $\varphi$ increases, the first-order segment reduces in length, until, as $\varphi \to \pi/2$, it approaches the width of the Aoki phase that appears at $\varphi = \pi/2$, i.e. with end points $\hat{\epsilon}_q = \pm 2w'$. [Recall that the phase diagram at $\varphi = \pi/2$ is given by Fig. 4.2(a) rotated by 90°; see also Fig. 4.3.] The first-order segment at the halfway point, $\varphi = \pi/4$, is shown as the horizontal solid (red) line in Fig. 4.4.

The length of the segment can be obtained analytically for all $\varphi$. To do so, one extremizes the potential after setting $\widehat{m}_q = 0$. The global minimum lies at

$$\sin\theta = \frac{-\hat{\epsilon}_q \sin\varphi}{2(c_\ell \hat{\epsilon}_q^2 \cos^2\varphi - w')}\,, \tag{4.29}$$

with the sign of $\cos\theta$ undetermined. As one passes through the transition line (by varying $\widehat{m}_q$), $\cos\theta$ changes sign, indicating a first-order transition. Solving for the endpoints, where $\cos\theta = \pm 1$, we find

$$|\hat{\epsilon}_q| = \frac{-\sin\varphi + \sqrt{\sin^2\varphi + 16 c_\ell w' \cos^2\varphi}}{4 c_\ell \cos^2\varphi}\,. \tag{4.30}$$

This gives the results quoted above in the limits $\varphi \to 0, \pi/2$.

The corresponding results for $w' < 0$ can be obtained from those just described for $w' > 0$ using the transformation of Eq. (4.28). In words, to obtain the phase diagram for $\varphi = \varphi_0$ and $w' = w'_0 < 0$, one takes the diagram with $\varphi = \pi/2 - \varphi_0$ and $w' = |w'_0|$ and rotates it by 90° counterclockwise. This implies that the first-order transition line is now vertical.

Similarly, one can obtain results for $\omega = \pi/2$ from those at $\omega = 0$ using the transformation of Eq. (4.18). Specifically to obtain the phase diagram for $\varphi = \varphi_0$ at $\omega = \pi/2$, one takes that with $\varphi = \pi/2 - \varphi_0$ and $\omega = 0$ and reflects it in the $\widehat{m}_q = \hat{\epsilon}_q$ line. This implies that the first order line is vertical for $w' > 0$ and horizontal for $w' < 0$. An example of this result (for $w' > 0$) is shown by the vertical solid (purple) line in Fig. 4.4.

Since there are no second-order phase transitions, the pion masses are nonvanishing throughout the phase plane, with the exception of the endpoint of the first-order transitions, where the mass of the neutral pion vanishes.

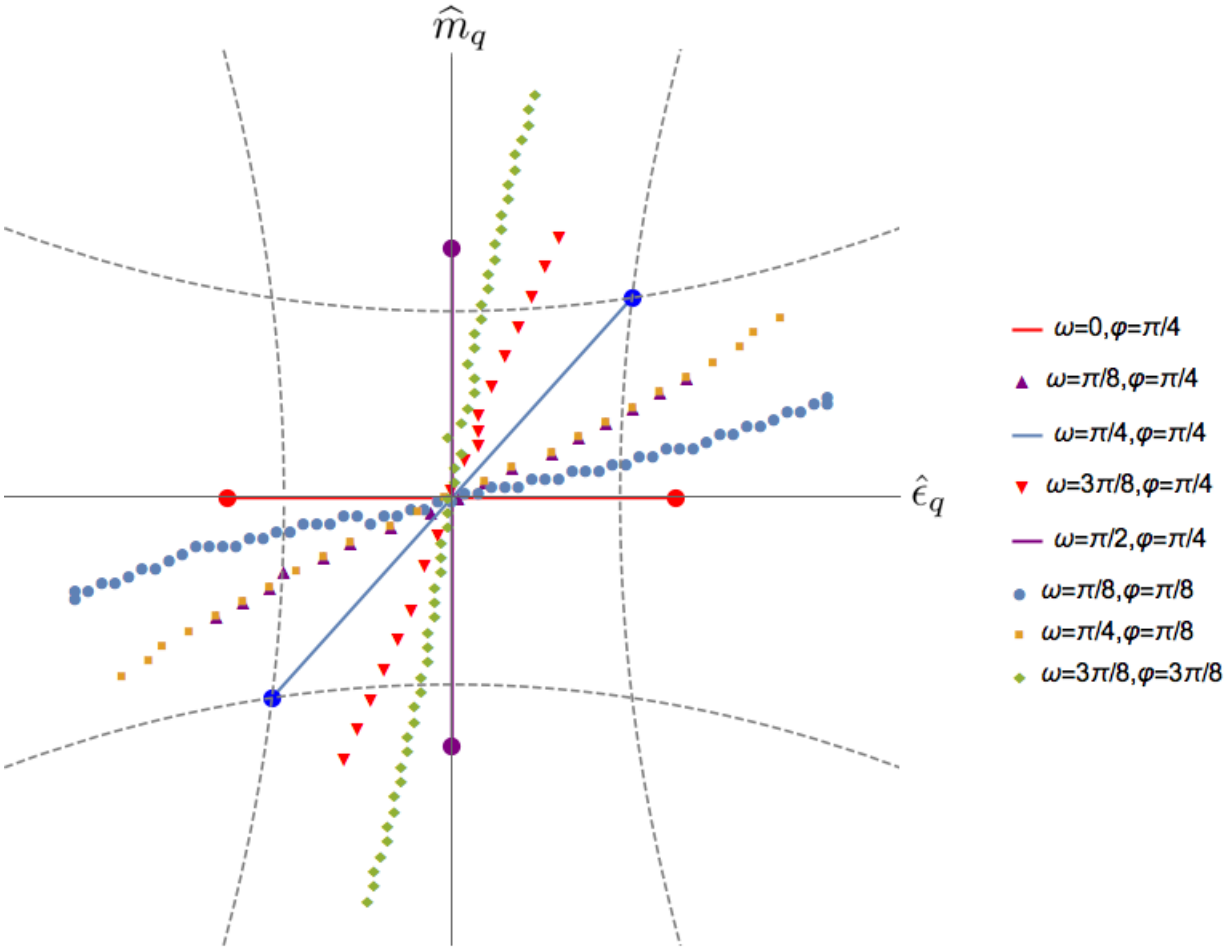


Figure 4.4: Phase diagram including discretization effects (with $w' > 0$) for several values of $\omega$ and $\varphi$. Solid lines are analytically determined first-order transition lines described in the text. Points represent the location of the numerically determined first-order transition lines. Dashed lines show the positions of the central second-order transition lines that arise at extremal values of $\omega$ and $\varphi$ as shown in Fig. 4.3. These are included to set the scale, since they depend on the values of $w'$ and $c_\ell$. Results for $w' < 0$ can be obtained from these using the transformations of Eqs. (4.19) and (4.28).

### *4.2.4 Nonextremal $\omega$ and $\varphi$*

Finally, we consider the most general choice of parameters: both $\omega$ and $\varphi$ nonextremal. Here, in most cases, we have to proceed numerically, although we can check the results analytically for the special case of $\omega = \varphi = \pi/4$.

We have found in the previous subsection that, for extremal $\omega$ but nonextremal $\varphi$ there is a first-order transition line of finite length that is oriented either horizontally or vertically. For example, Fig. 4.4 shows that for $\varphi = \pi/4$ and $w' > 0$, the transition line is horizontal at $\omega = 0$ and vertical at $\omega = \pi/2$. It is not surprising, therefore, that for intermediate values of $\omega$ there is a first order transition line of finite length at an intermediate angle that interpolates between the horizontal and vertical limits. Examples for several intermediate values of $\omega$ for $\varphi = \pi/4$, $\pi/8$ and $3\pi/8$ are shown in the figure. We observe that, aside from the special case of $\omega = \varphi = \pi/4$, the first order lines are "S-shaped" rather than straight. We also observe an example of an overlapping transition line (though of different lengths) for the parameter choices $(\omega, \varphi) = (\pi/8, \pi/4)$ and $(\pi/4, \pi/8)$. We have not understood this overlapping analytically, and do not know if it is exact. Figure 4.4 also shows an example of the application of the symmetry of Eq. (4.18), which implies that the transition lines for parameters $(\omega, \varphi) = (\pi/8, \pi/8)$ and $(3\pi/8, 3\pi/8)$ should be related by reflection in the diagonal $\widehat{m}_q = \hat{\epsilon}_q$ line.

For $\omega = \varphi = \pi/4$, we know from the symmetry of Eq. (4.18) that the transition line must be invariant under reflection in the $\widehat{m}_q = \hat{\epsilon}_q$ line. Thus it must either lie along this line or be perpendicular to it, and in both cases it must be straight. It turns out that, for $w' > 0$ it lies along the diagonal, as shown in Fig. 4.4 by the solid (blue) line. Given this information, it is straightforward to determine the end points analytically, and we find that they lie at

$$\widehat{m}_q = \hat{\epsilon}_q = \pm \frac{1 - \sqrt{1 - 16 c_\ell w'}}{4 c_l} \,. \tag{4.31}$$

We note the curious result that these points lie at the junction of the boundaries of the Aoki-Dashen phases for extremal $\omega$ and $\varphi$.

### *4.3 Maximal twist condition*

The standard technique for tuning to maximal twist in the absence of isospin breaking is to enforce the vanishing of the "PCAC mass". This determines the critical value of the untwisted component of the common quark mass. This critical value can then be used even in the presence of isospin breaking due to quark masses, i.e. when the twisted components of the up and down quark masses differ. This is no longer the case when electromagnetism is included, because, as explained in the Introduction, the critical masses for the up and down quarks differ. Setting the PCAC mass to zero is essentially a way of enforcing, in a particular correlation function, the restoration of SU(2) flavor and parity symmetries at nonzero lattice spacing. In the presence of electromagnetism, however, these symmetries are absent even in the continuum limit, so it makes no sense to enforce them. Thus one must use alternative methods to tune to maximal twist.

In Ch. 3, we analyze a method for carrying out the tuning in the presence of electromagnetism, proposed in Ref. [23], This involves partial quenching, and our analysis is somewhat involved, but the details do not matter here. Our key finding is that the method fails to tune the untwisted components of the up and down quark masses to zero, as required for maximal twist, but rather only enforces a condition on the condensate:

$$\langle \Sigma \rangle \equiv e^{i(\theta+\omega)\tau_3} = e^{i(\pi/2)\tau_3} \quad \Rightarrow \quad \theta' \equiv \theta + \omega = \pi/2\,. \tag{4.32}$$

In the first equality we are simply using the definition of the phase angle $\theta$, given in Eq. (4.10), together with the result that $\vec{n}$ points in the $\tau_3$ direction. This implies that the total $\tau_3$ rotation angle is $\theta' = \theta + \omega$, which is set by the condition of Ref. [23] to $\pi/2$.

The condition (4.32) is indeed consistent with the desired parameters, i.e. with $\omega = \pi/2$ and $\varphi = 0$. To see this we note that, for these parameters, the phase diagrams are those of Fig. 4.2 except that the $w' < 0$ and $w' > 0$ diagrams are interchanged.[8] Thus, as long as the physical masses are such that one is in the unshaded region, i.e. as long as one avoids the

[8]This result is obtained by acting with the transformation (4.19) on the $\omega = \varphi = 0$ results that are actually shown in the figure. See also also Fig. 4.3.

Aoki-Dashen phases, one has that $\cos\theta = 1$ and thus $\theta = 0$. This means that $\theta' = \omega = \pi/2$, which satisfies Eq. (4.32).

However, there is in general a one-dimensional family of solutions to Eq. (4.32), all having different values of $\omega$ and $\varphi$. One can understand this intuitively as follows. Nonvanishing values of $\omega$ and of $\varphi$ both violate parity, and thus both lead to a nonzero twist of the condensate, i.e. a nonzero value of $\theta'$. For any choice of $\varphi$, the desired value $\theta' = \pi/2$ can, in general, be obtained by a suitable value of $\omega$. Thus there is a line in the $\omega - \varphi$ plane along which the condition is satisfied. In order to tune to the desired point on this line an additional condition is needed.

It turns out to be easier to do the calculation using the parametrization of the mass matrix given in Eq. (4.6). Here we fix the twisted components of the masses $\widehat{\mu}_u$ and $\widehat{\mu}_d$ (ultimately to their physical values, namely $2B_0 m_u^{\rm phys}$ and $2B_0 m_d^{\rm phys}$, respectively) and vary the untwisted ccmponents $\widehat{m}_u^W$ and $\widehat{m}_d^W$. This corresponds to what is done in actual simulations. The condition of Eq. (4.32) then forces the theory to lie on a line in the $\widehat{m}_u^W - \widehat{m}_d^W$ plane. Our aim is to determine this line and to find an additional condition that picks out the desired point on the line, namely $\widehat{m}_u^W = \widehat{m}_d^W = 0$.

In terms of the parametrization (4.6) the potential is

$$-\frac{\mathcal{V}}{f^2} = \frac{\widehat{m}_u^W + \widehat{m}_d^W}{2}\cos\theta' + \frac{\widehat{\mu}_u + \widehat{\mu}_d}{2}\sin\theta' + c_\ell\left(\frac{\widehat{\mu}_u - \widehat{\mu}_d}{2}\cos\theta' - \frac{\widehat{m}_u^W - \widehat{m}_d^W}{2}\sin\theta'\right)^2 + w'\cos^2\theta' \,.$$

In order for an extremum of this potential to lie at $\theta' = \pi/2$, it is simple to show that the untwisted masses must satisfy

$$\frac{\widehat{m}_d^W}{\widehat{m}_u^W} = -\left(\frac{1 - c_\ell(\widehat{\mu}_u - \widehat{\mu}_d)}{1 + c_\ell(\widehat{\mu}_u - \widehat{\mu}_d)}\right) \equiv s \,, \tag{4.33}$$

*i.e.*, the theory must lie along a straight line in the $\widehat{m}_u^W - \widehat{m}_d^W$ plane with slope $s$ determined by the physical masses and $c_\ell$. We can turn this into a constraint on $\omega$ and $\varphi$ by equating the parametrizations of Eqs. (4.7) and (4.6). One finds $\widehat{m}_{u,d}^W = \widehat{\mu}_{u,d}\cot(\omega \pm \varphi)$, so that the

allowed values of $\omega$ and $\varphi$ satisfy

$$s\,\widehat{\mu}_u \cot(\omega+\varphi) = \widehat{\mu}_d \cot(\omega-\varphi)\,. \tag{4.34}$$

Lines satisfying this equality are shown in Fig. 4.5. The desired point is at $\varphi = 0$, $\omega = \pi/2$, but, as claimed above, solutions exist for all values of $\varphi$.

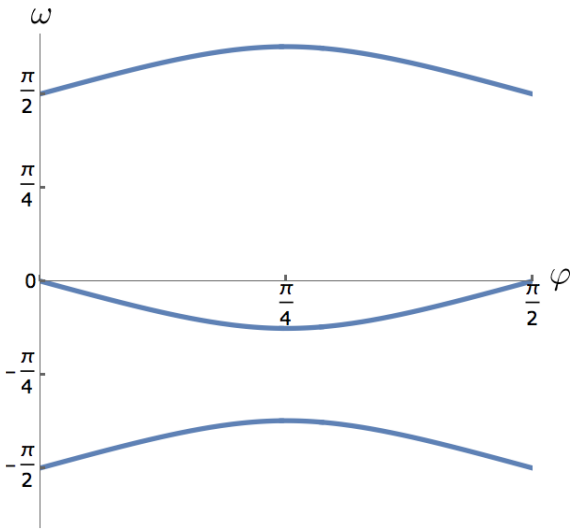


Figure 4.5: Values of $\omega$ and $\varphi$ for which $\theta' = \pi/2$, using $\widehat{\mu}_u \approx 2B_0 m_u^{\rm phys}$ and $\widehat{\mu}_d \approx 2B_0 m_d^{\rm phys}$, but with $c_\ell$ larger than the physical value so as to increase the curvature of the lines for the sake of clarity.

The above considerations assume that the extrema at $\theta' = \pi/2$ is a minimum of the potential. This can be determined by examining either the second derivative of the potential evaluated at the correct value of $s$ and $\theta' = \pi/2$ or, equivalently, by checking that the neutral pion mass is nonnegative. The neutral pion mass along the line (4.33) is

$$m_{\pi^0}^2 = \frac{\hat{\mu}_u+\hat{\mu}_d}{2} - 2c_\ell\left(\frac{\hat{\mu}_u-\hat{\mu}_d}{2}\right)^2 + 2c_\ell\left(\frac{\hat{m}_u^W-\hat{m}_d^W}{2}\right)^2 - 2w'. \tag{4.35}$$

The sum of the first two terms is positive for physical parameters (since this is just the physical neutral pion mass-squared at this order in $\chi$PT, and higher order corrections are

small). The third term is always positive and vanishes only at the point of maximal twist (as long as $s \neq 1$, which is the case for physical parameters). The last term can be negative if $w' > 0$. Thus, if $w'$ takes a large enough positive value, it can be that the point we are aiming to tune to does not lie at the minimum of the potential. This happens when the physical point lies inside the Aoki-Dashen phase.

Assuming that this does not happen, we can ask what criterion can be used to tune to maximal twist along the lines satisfying Eq. (4.32). The criterion proposed in Ch. 3 is simply to minimize the neutral pion mass, Eq. (A.24), since, as already noted, this occurs when $\hat{m}_u^W = \hat{m}_d^W = 0$. One can also minimize the charged pion mass, the expression for which is given in Ch. 3.

We close this section by making a connection with our results for the phase diagram for general $\omega$ and $\varphi$, obtained in Sec. 4.2. In particular, we imagine that we have somehow tuned close to maximal twist, but that there is a small offset. Specifically we fix $\omega = \pi/2 + \delta$ and $\varphi = \alpha\delta$ with $|\delta| \ll 1$ and $\alpha \sim \mathcal{O}(1)$. This differs from (and is less realistic than) our analysis above where we fixed the twisted up and down masses. Nevertheless, this allows a valid theoretical exercise: with $\omega$ and $\varphi$ fixed in this way, we determine the line in the $\widehat{m}_q - \hat{\epsilon}_q$ plane that satisfies the tuning condition of Eq. (4.32).

Written in terms of the variables of Eq. (4.7), the tuning condition becomes

$$s(\widehat{m}_q + \hat{\epsilon}_q)\cos(\omega + \varphi) = (\widehat{m}_q - \hat{\epsilon}_q)\cos(\omega - \varphi)\,, \tag{4.36}$$

where we recall that $s$ is given by Eq. (4.33). For our fixed values of $\omega$ and $\varphi$, this equation can be converted into a result in the $\widehat{m}_q - \hat{\epsilon}_q$ plane, using an expansion in powers of $\delta$:

$$\widehat{m}_q = -\hat{\epsilon}_q \frac{\alpha - 2c_\ell \hat{\epsilon}_q}{1 - 2\alpha c_\ell \hat{\epsilon}_q} + \mathcal{O}(\delta^2)\,. \tag{4.37}$$

Examples of this result (for both signs of $w'$) are shown in Fig. 4.6 by the (green) solid lines. As noted above, this result is only valid if the pion mass-squared of Eq. (A.24) is positive or zero. Thus the line terminates at the point where $m_{\pi^0}$ vanishes, which occurs only for $w' > 0$.

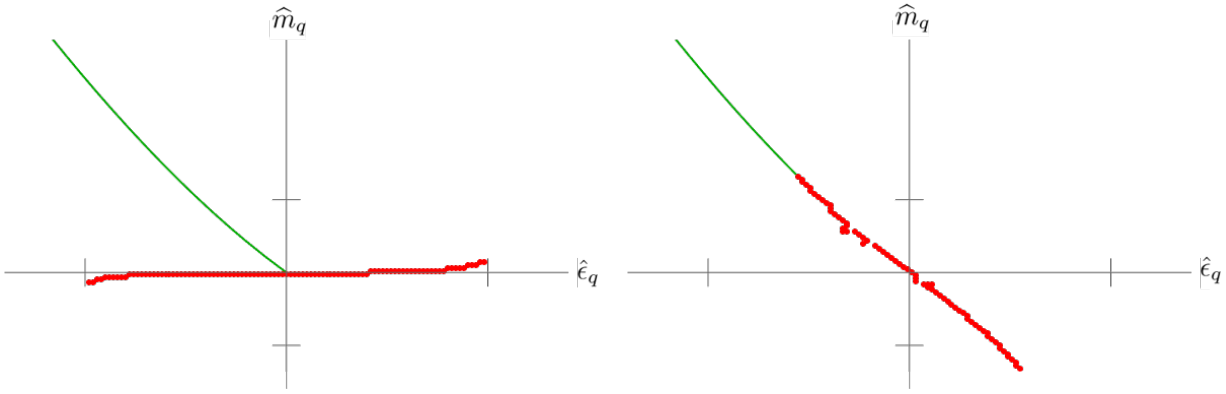


(a) (b)

Figure 4.6: Applying the tuning condition at fixed $\omega = \pi/2 + 0.1$ and $\varphi = 0.05$ for (a) $w' < 0$ and (b) $w' > 0$. The size of $c_\ell$ and $w'$ can be seen from the tick marks on the axes, which lie at $\widehat{m}_q = \pm 2w'$ and $\hat{\epsilon}_q = \pm\sqrt{|w'|\,/c_\ell}$. The solid (green) line shows the result of applying the condition (4.32) as well as requiring that $m_{\pi^0}^2 \geq 0$. (Red) points show the locations of the numerically determined first-order transition lines.

Also shown in the figures are the positions of the first-order lines, which have been determined numerically. We observe that, for $w' < 0$, the line along which Eq. (4.32) holds goes all the way to the origin, where it runs into the first-order line. By contrast, for $w' > 0$ the endpoint of the tuned line is precisely the starting point of the first-order line. This is reasonable since it is the only position in the phase diagram where a pion is massless. In any case, we see that, even for nonextremal $\omega$ and $\varphi$, where there is only a first-order transition, the condition (4.32) cannot be maintained all the way to the origin.

## *4.4 Conclusions*

In this short note, we have determined the phase structure of lattice QCD in the presence of isospin breaking and a nonvanishing value of $\Theta_{\rm QCD}$. This is, for the present, a theoretical exercise, but one that was necessary in order to understand how to tune to maximal twist

in the presence of electromagnetism, an analysis that was completed in Ch. 3.

The results are also interesting in their own right. In particular, for generic (nonextremal) values of the twist angle and $\Theta_{\mathrm{QCD}}$, the continuum theory has no phase structure, while the lattice theory has a segment of first-order transition whose length is set by $w'$ and is thus of $\mathcal{O}(a^2)$.

We have kept in our analysis only the leading order terms arising from each type of symmetry breaking. A quantitative analysis would require the inclusion of all other terms of $\mathcal{O}(m^2)$ as well as those proportional to $ma$. Based on our work in Ch. 2, however, we do not expect these terms to lead to qualitative changes in the phase diagrams.

### *4.5 Acknowledgements*

This work was supported in part by the United States Department of Energy grant DE-SC0011637.

# Chapter 5

# LATTICE INVESTIGATION OF INSTANTON EFFECTS IN QCD

## *5.1 Introduction*

While it has long been known that instantons play a role in QCD, leading effects due to a single instanton are multiplied by a factor of $e^{-8\pi^2/g^2}$. While these can be significant at low energies, where $g$ is large, perturbation theory in this regime is not trustworthy. At higher energies, where perturbation theory does apply, $g$ is small and instanton effects are exponentially suppressed. In order to understand the effects of instantons, physicists often rely on results from models such as the instanton liquid model [60]. Another approach, used in recent work [25, 24] is to study Greens functions which maximally violate chirality. In massless QCD, there are no perturbative chirality violating contributions and the only contributions come from a non-zero instanton background. These Greens functions allow an analytic window into non-perturbative physics that can be checked against lattice calculations such as those analyzed below in Sec. 5.2.

The remainder of this section will briefly summarize Ref. [25], introducing the chirality violating Greens functions and explaining how they can be understood using the operator product expansion (OPE). We will skip over many of the technical details in order to get to the Greens functions that are important in physical QCD, where $N_c = N_f = 3$, and can be measured on the lattice using publicly available configurations.

### *5.1.1 Chirality Violating Greens Functions*

To begin, consider an SU($N_c$) theory with $N_f$ light flavors, where $N_f$ is sufficiently small that the theory is asymptotically free. Generally a Dirac fermion can be decomposed into

left and right handed fields using the projectors introduced in Sec. 1.2

$$\begin{aligned} \mathbb{1}\psi &= (P_L + P_R)\psi = P_L\psi_L + P_R\psi_R, \qquad P_{L,R} = \frac{\mathbb{1} \pm \gamma_5}{2},\ (P_{L,R})^2 = \mathbb{1} \\ \overline{\psi}\mathbb{1} &= \overline{\psi}(P_L + P_R) = \overline{\psi}_R P_L + \overline{\psi}_L P_R, \qquad P_L P_R = P_R P_L = 0\ . \end{aligned} \tag{5.1}$$

Chirality preserving operators only have Wick contractions between left(right)-handed fermionic fields and left(right)-handed anti-fermionic fields for each flavor. One example is the kinetic term of the QCD Lagrangian, Eq. 1.43. Chirality violating operators can be constructed out of a quark bilinear with zero or an even number of $\gamma^\mu$s. The simplest example is $\overline{q}(x)q(x) = \overline{q}_R(x)q_L(x) + \overline{q}_L(x)q_R(x)$. Another chirality violating bilinear is the Pauli term, $\overline{q}(x)\sigma_{\mu\nu}F^{\mu\nu}(x)q(x)$, where $\sigma_{\mu\nu} = \frac{i}{2}[\gamma_\mu, \gamma_\nu]$. Using these elements, a gauge invariant Greens function that vanishes in normal perturbation theory [1] can be constructed. While these operators vanish in normal perturbation theory, they will not vanish in the one instanton background, due to instantons having chirality violating zero modes for each flavor. One such example is the follwing two point function, where $f$ is a flavor index,

$$G(x,0) = \left\langle \left( \prod_{f=1}^{A} \overline{q}_f q_f(x) \right) \left( \prod_{f=A+1}^{N_f} \overline{q}_f q_f(0) \right) \right\rangle = \langle \mathcal{O}_1(x)\mathcal{O}_2(0) \rangle\ . \tag{5.2}$$

This correlation function is singular and can be analyzed at small $x$ using the standard OPE with the form,

$$\mathcal{O}_1(x)\mathcal{O}_2(0) \approx \sum_{n=0}^{\infty} C_n(x)\tilde{\mathcal{O}}_n(0)\ . \tag{5.3}$$

The coefficents, $C_n$, in the OPE can be written as a short distance expansion as long as the theory is asymptotically free. The lowest dimension operator that contributes is the identity,

$$\mathcal{O}_1(x)\mathcal{O}_2(0) \approx C_0(x)\mathbb{1} + \text{higher dimension}\ . \tag{5.4}$$

The coefficient, $C_0(x)$, vanishes in normal perturbation and thus must be non-perturbative. As discussed in Refs. [25, 24], its leading short-distance behavior is given by perturbation

[1] Normal perturbation theory here means expanding about the $S = 0$, zero-instanton background

theory about a single instanton background. The leading behavior of $C_0$ can be estimated from dimensional analysis and the instanton factor to be

$$C_0(x) \sim (\Lambda x)^{b_0} x^{-3N_f} \tag{5.5}$$

where $b_0 = 3N_f + \frac{11}{3}(N_c - N_f)$ and $\Lambda$ is the scale of the theory. $(\Lambda x)^{b_0}$ is just the standard instanton factor, $e^{-8\pi^2/g^2}$, as seen from the 1-loop solution to the beta function

$$\frac{g^2}{4\pi} = \left(-\frac{b_0}{2\pi}\log(x\Lambda)\right)^{-1} \rightarrow (\Lambda x)^{b_0} = e^{-8\pi^2/g^2}$$

where the renormalization scale is taken to be $\mu_R = x^{-1}$. It can be seen from Eq. 5.5 that if $N_f > N_C$ there will be a singularity, if $N_f < N_C$ there will be no singularity, and in the case relevant for QCD, $N_f = N_C$ there will be a logarithmic singularity. In the case of a logarithmic singularity, a more careful analysis is required, as discussed in [25].

In order to avoid the issue of a logarithmic singularity in QCD with $N_f = N_C = 3$, it is useful to include insertions of $P_{L/R}\sigma_{\mu\nu}F^{\mu\nu}$, which, by power counting, will each bring additional singular terms proportional to $x^{-2}$. Specifically, the Greens function that we have investigated on the lattice is

$$G(x,0) = \langle \overline{u}(x) P_{L/R}\sigma_{\mu\nu}F^{\mu\nu}(x) d(x) \overline{d}(0) P_{L/R}\sigma_{\rho\sigma}F^{\rho\sigma}(0) s(0)\overline{s}P_{L/R}u(0)\rangle \ . \tag{5.6}$$

In order to maximally violate chirality, the projector $P_L$ or $P_R$ must be included explicitly. This Greens function has the OPE

$$\begin{aligned}\overline{u}P_{L/R}\sigma_{\mu\nu}F^{\mu\nu}d(x)\overline{d}P_{L/R}\sigma_{\rho\sigma}F^{\rho\sigma}s\overline{s}P_{L/R}u(0) \sim c\Lambda^9 x^{-4}(1 + k\log(x\mu))\mathbb{1} \\ + kx^{-4}\tilde{\mathcal{O}}_1(0) + \text{higher dimension}\end{aligned} \tag{5.7}$$

where $k$ is of order $(g^2/4\pi)/\pi$ and all three projectors are either $P_L$ or $P_R$. The $\log(x\mu)$ term includes non-perturbative operator mixing with the full instanton ensemble and is not calculable, but will not be more singular than the leading term. As long as $x$ is small enough, the terms proportional to $k$ should be a small effect that can either be ignored or calculated on the lattice and subtracted [24].

The coefficient $c$ in Eq. 5.7 can be calculated in the instanton background, as shown in [24]. In the $\overline{\text{MS}}$ scheme at order $g^2$, the leading term of the Greens function Eq. 5.6 is calculated to be

$$G(x,0) = -2.64\left(\frac{g^2}{4\pi}\right)^{-6}\Lambda^9 x^{-4}\ . \tag{5.8}$$

In order to move to lattice simulation, there are lessons to be taken from this calculation in regards to the required lattice spacing and quark masses. In order for the higher dimension terms in the OPE proportional to $k$ to be only a $\sim 10\%$ effect, $x \sim 0.11$fm. For the lattice, this means an ideal lattice spacing $a$ would be less than 0.11fm. As both in physical QCD and on the lattice, quarks are massive, there are perturbative contributions to the Greens function. The leading perturbative contribution to this Greens function behaves as

$$\frac{m_u m_d m_s}{(4\pi^2)^4 x^{10}}\ . \tag{5.9}$$

For reasonable quark masses, light quark (up and down) mass $m_\ell \lesssim 10$MeV and strange quark mass $m_s \sim 100$MeV, the non-perturbative contribution to the Greens function is dominant for $x \gtrsim (30\Lambda)^{-1} \sim 0.02$fm. The result of these constraints is a window $0.02\text{fm} \lesssim x \lesssim 0.11$fm that must be taken into account both when choosing a lattice spacing and when analyzing the measurement of the correlation function on the lattice.

## *5.2 Simulation details and setup*

### *5.2.1 Ensemble details and mass tuning*

For this investigation, we used 440 configurations from a publicly available ensemble provided by the MILC collaboration, described in Ref. [10]. The ensemble analyzed was generated using the asqtad improved staggered action with $2+1$ flavors. This ensemble has dimension $16^3 \times 48$, coupling constant $\beta = \frac{6}{g^2} = 6.572$, light quark mass $m_\ell a = 0.0097$, strange quark mass $m_s a = 0.0484$, and has the lattice spacing $a \approx 0.14$fm and pion mass in lattice units $m_\pi a = 0.2456$. As mentioned in Sec. 5.1 this lattice spacing is larger than ideal. $a \approx 0.14\text{fm} \approx (1.4\text{GeV})^{-1}$ corresponds leading correction of terms with a factor of $k$, seen

in Eq. 5.7, of $\sim 20\%$ [47]. Furthermore, any distance greater than $\sim 4a$ will probe scales near $\Lambda_{\mathrm{QCD}}$, where the coupling diverges, and the perturbative expansion of $C_0$ breaks down entirely. For this reason and others, the following data should considered as a first study of the Greens function in Eq. 5.8 in which several systematic errors are not yet controlled.

The calculation of the Greens functions and related quantities was done using the Wilson action. This mixed action approach makes writing code and analysis simpler but explicitly breaks chiral symmetry. This explicit breaking means that the quark masses are additively renormalized and the mass parameter $\kappa_f = (2(m_f a+4))^{-1}$ must be tuned. In this simulation, the up and down quarks are degenerate so there are two values of $\kappa$ to tune: $\kappa_\ell$, the light quark mass parameter, and $\kappa_s$, the strange quark mass parameter. Chiral perturbation theory predicts that at leading order $m_\pi^2 \propto m_q \propto 1/\kappa - 1/\kappa_{crit}$. By calculating $m_\pi^2$ at a range of values of $\kappa$, the desired $\kappa_\ell$ and $\kappa_s$, as well as the point corresponding to zero quark mass, $\kappa_{crit}$ can be determined. $\kappa_\ell$ is found by tuning to the pion mass quoted by MILC [10] $m_\pi a = 0.2456$. $\kappa_s$ is found using the $\eta_s$ method described in Ref. [20], where $\kappa$ is tuned to the mass of the fictitious $\eta_s$, which is a pion constructed using valence strange quark fields with no quark-disconnected contractions included, rather than light quarks. The mass of the $\eta_s$ was found in Ref. [20] to be $m_{\eta_s} = 685.8$MeV which in our lattice units is $m_{\eta_s} a = 0.4866$. The best fits to these meson masses were found to be $\kappa_\ell = 0.1691$ $\kappa_s = 0.1658$ with $\kappa_{crit} = 0.1703$ as seen in the plots of the zero spatial momentum pion correlator, Fig. 5.1, and of pion mass squared versus $\kappa^{-1}$, Fig. 5.2. The lattice simulation was performed using the Chroma software package, distributed by JLab [27]. The meson correlator measurements were performed and parsed using the hadspec code provided by Balint Joo in numerous tutorials. The correlators were measured using code written by myself, using Chroma and QDP++'s built-in functions.

### *5.2.2 Variance Reduction*

In measuring the operator Eq. 5.7, it would be optimal to measure it for all $16^3 \times 48$ choices of origin, while calculating each propagator as precisely as possible. This is not practical

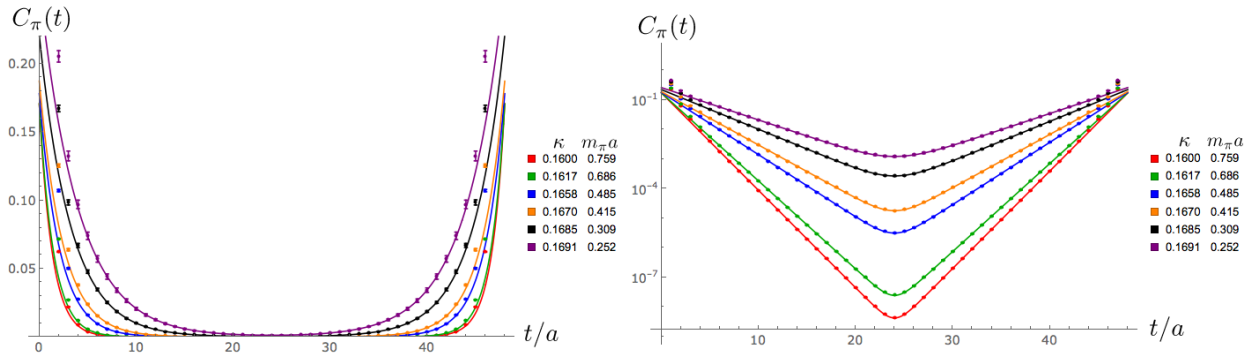


Figure 5.1: Pion correlators at zero spatial momentum for a range of values of $\kappa$, including $\kappa_\ell = 0.1691$ and $\kappa_s = 0.1658$. The right-hand plot is on a log scale.

from a computational perspective and it would also be excessive, as measurements on an overlapping space-time volume are expected to be highly correlated. In order to obtain precise measurements of the operator for each configuration, while keeping computational costs reasonable, we the variance reduction method suggested in Ref. [13].

The method in Ref. [13] works as follows. Assume there is an observable, $O$, that can accurately be measured on an ensemble of configurations to obtain an expectation value,

$$\langle O \rangle = \frac{1}{N_{conf}} \sum_{i=1}^{N_{conf}} O_i + \mathcal{O}\left(\frac{1}{\sqrt{N_{conf}}}\right) . \tag{5.10}$$

Then a secondary measurement can be constructed, $O^{appx}$, which obeys three criteria. First, it must be highly correlated with $O$,

$$r = \mathrm{Corr}(O, O^{appx}) = \frac{\langle \Delta O \Delta O^{appx} \rangle}{\sqrt{\langle (\Delta O)^2 \rangle \langle (\Delta O^{appx})^2 \rangle}} \approx 1, \quad \Delta X = X - \langle X \rangle . \tag{5.11}$$

Second, the computational cost to compute to $O^{appx}$ should be significantly less than to compute $O$. Lastly, $O^{appx}$ must be invariant (or covariant) under a lattice symmetry transformation, i.e. after transforming $O^{appx}$ by some group element $g \in G$, where G is the group of lattice symmetries: translations, rotations, etc., $\langle O^{appx} \rangle = \langle O^{appx,g} \rangle$. If these conditions

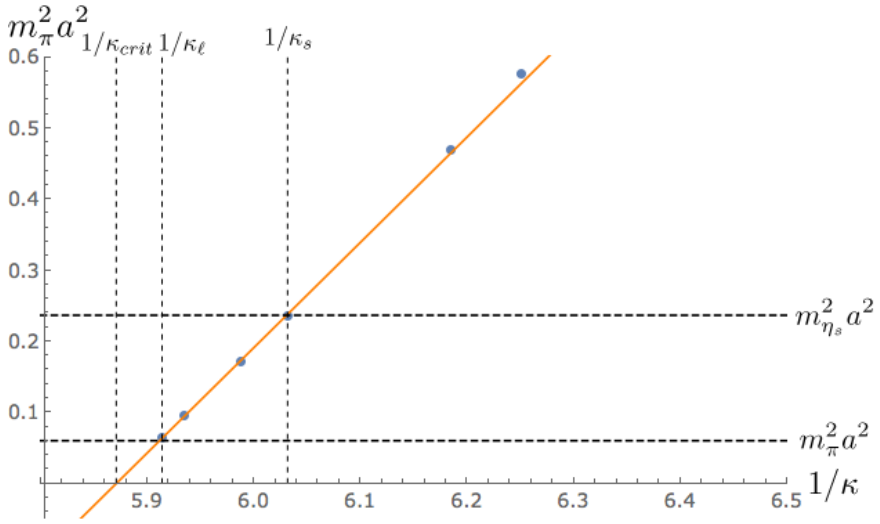


Figure 5.2: Pion mass squared versus $\kappa^{-1}$ showing $\kappa_\ell = 0.1691$, $\kappa_s = 0.1658$ and $\kappa_{crit} = 0.1703$. Error bars represent the standard error of the fit used in in determining pion masses.

hold, it is practical to measure an improved observable $O^{imp}$ which is defined as,

$$O^{imp} = O - O^{appx} + \frac{1}{N_G}\sum_{g\in G} O^{appx,g} \tag{5.12}$$

where $N_G$ is the number of group transformations used. If these conditions hold, the statistical error of $\langle O^{imp}\rangle$ is smaller than that of $\langle O^{imp}\rangle$,

$$\mathrm{err}_{\mathrm{imp}} = \mathrm{err}\sqrt{2(1-r) + \frac{1}{N_G}}\ . \tag{5.13}$$

For our simulation, we were inspired by the truncated solver method [6]. We used $O^{appx}$ which is the same operator as $O$, namely the operator in Eq. 5.7, symmetrized under parity,

$$O(x,0) = \overline{u}P_L\sigma_{\mu\nu}F^{\mu\nu}d(x)\overline{d}P_L\sigma_{\rho\sigma}F^{\rho\sigma}s\overline{s}P_Lu(0) + \overline{u}P_R\sigma_{\mu\nu}F^{\mu\nu}d(x)\overline{d}P_R\sigma_{\rho\sigma}F^{\rho\sigma}s\overline{s}P_Ru(0) \tag{5.14}$$

but allowing a much larger residual in the conjugate gradient solver when calculating the propagators for $O^{appx}$. The computationally costly measurements, $O$, were performed using

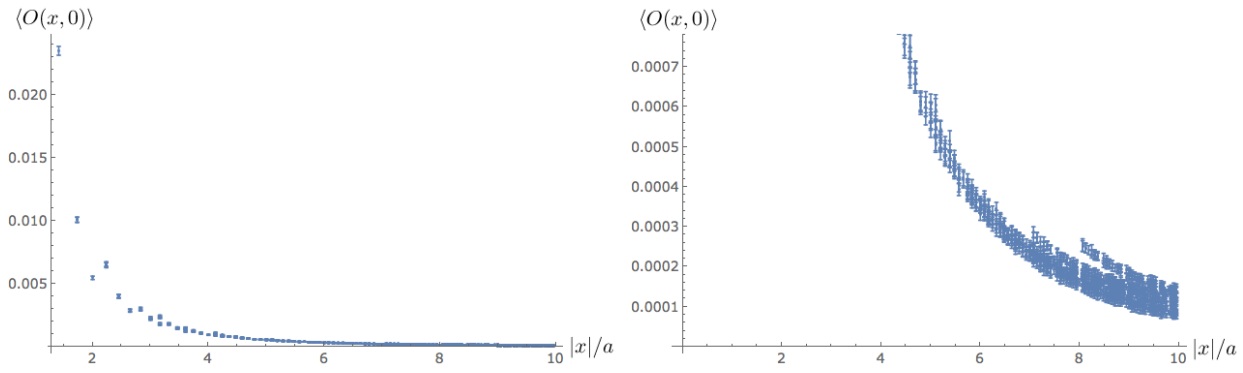


Figure 5.3: Measurement of Eq. 5.14. The right-hand plot of the correlator shows a magnified version of the same data.

a conjugate gradient residual of $10^{-12}$ whereas the computationally cheaper measurements, $O^{appx}$, used a residual of $10^{-2}$. The cheaper measurement took approximately 60 times less time to calculate. To ensure that the costly and cheap measurements were highly correlated, the correlation of the two sets of data was calculated for 3 configurations for each correlation function measured and found to have an average value of $r = 0.972$ . The symmetry transformation exploited was just that of translational symmetry on a given configuration. For each configuration, $O$ was measured with one origin, while $O^{appx}$ was measured 48 times with the origin placed at equally spaced nodes on a $2^3 \times 6$ grid.

### *5.3 Measurement of non-perturbative Greens functions*

Our preliminary measurement of the operator Eq. 5.14, seen in Fig. 5.3 did not have a good fit to the form $1/x^4$ (fit not shown). This suggests that the measurement is dominated by long distance effects. Generically $\langle O(x,0)\rangle$ is expected to have the form,

$$\langle O(x,0)\rangle = -2.64\left(\frac{g^2}{4\pi}\right)^{-6}\Lambda^9 x^{-4} + \text{ Long distance effects} + \mathcal{O}(m_u m_d m_s) \tag{5.15}$$

We expect that the long distance effects are dominated by contributions from hadronic states, specifically the scalar and psuedoscalar mesons, also known as the $a_0$ and the pion.

To see this, we expand the projectors in Eq. 5.14 to obtain four separate terms, comprising a "pion-like" operator and an "$a_0$-like" operator,

$$\begin{aligned} O =& \overline{u}P_L\sigma_{\mu\nu}F^{\mu\nu}d(x)\overline{d}P_L\sigma_{\rho\sigma}F^{\rho\sigma}s\overline{s}P_Lu(0) + \overline{u}P_R\sigma_{\mu\nu}F^{\mu\nu}d(x)\overline{d}P_R\sigma_{\rho\sigma}F^{\rho\sigma}s\overline{s}P_Ru(0) \\ =& \frac{1}{4}\left(\overline{u}\sigma_{\mu\nu}F^{\mu\nu}d(x)\overline{d}\sigma_{\rho\sigma}F^{\rho\sigma}s\overline{s}u(0) + \overline{u}\sigma_{\mu\nu}F^{\mu\nu}d(x)\overline{d}\gamma_5\sigma_{\rho\sigma}F^{\rho\sigma}s\overline{s}\gamma_5u(0)\right. \\ &+ \left.\overline{u}\gamma_5\sigma_{\mu\nu}F^{\mu\nu}d(x)\overline{d}\gamma_5\sigma_{\rho\sigma}F^{\rho\sigma}s\overline{s}u(0) + \overline{u}\gamma_5\sigma_{\mu\nu}F^{\mu\nu}d(x)\overline{d}\sigma_{\rho\sigma}F^{\rho\sigma}s\overline{s}\gamma_5u(0)\right) \\ =& \frac{1}{4}\left(O^{\pi} + O^{a_0}\right) \end{aligned} \tag{5.16}$$

$$O^{a_0} = \overline{u}\sigma_{\mu\nu}F^{\mu\nu}d(x)\overline{d}\sigma_{\rho\sigma}F^{\rho\sigma}s\overline{s}u(0) + \overline{u}\sigma_{\mu\nu}F^{\mu\nu}d(x)\overline{d}\gamma_5\sigma_{\rho\sigma}F^{\rho\sigma}s\overline{s}\gamma_5u(0) \tag{5.17}$$

$$O^{\pi} = \overline{u}\gamma_5\sigma_{\mu\nu}F^{\mu\nu}d(x)\overline{d}\gamma_5\sigma_{\rho\sigma}F^{\rho\sigma}s\overline{s}u(0) + \overline{u}\gamma_5\sigma_{\mu\nu}F^{\mu\nu}d(x)\overline{d}\sigma_{\rho\sigma}F^{\rho\sigma}s\overline{s}\gamma_5u(0)\ . \tag{5.18}$$

We propose that $O^{a_0}$ will be $a_0$-like under the assumption that the strange quark loop, $s\overline{s}$, will be dominated by the identity component in Dirac space, resulting in a measurement similar to an $a_0$ correlator, $\langle\overline{u}d(x)\overline{d}u(0)\rangle$. Similarly, we propose that $O^{\pi}$ will be pion-like, resulting in a measurement similar to a pion correlator, $\langle\overline{u}\gamma_5d(x)\overline{d}\gamma_5u(0)\rangle$. This assumption can be tested by comparing the measurement of each part of $O^{a_0}$ and $O^{\pi}$. If they are highly correlated it suggests whether or not $\gamma_5$ is inserted between $\overline{s}$ and $u$ does not have much effect on the correlator. Using this approach we will subtract the $a_0$ and pion scalar propagator from the measurement of $O^{a_0}$ and $O^{\pi}$ repectively before combining them with intent of extracting the $1/x^4$ behavior seen in Eq. 5.8.

### *5.3.1 $a_0$ Correlator*

Before fitting $O^{a_0}$ and $O^{\pi}$, it is good to know what $m_{\pi}a$ and $m_{a_0}a$ are for $\kappa_{\ell} = 0.1691$ so it can be determined whether $O^{a_0}$ and $O^{\pi}$ are $a_0$ and pion-like. $m_{\pi}$ was already determined above, as shown in Fig. 5.1, to be $m_{\pi}a = 0.252$ in lattice units. The determination of $m_{a_0}a$ is slightly more difficult. In the right-hand plot of Fig. 5.4 we see that at light masses, the $a_0$ correlator is noisy and potentially has a "bump" where the correlator has the wrong sign. A similar bump is seen for the lighter quark mass $a_0$ correlators in Ref. [44] where it is attributed to a $\eta'\pi$ ghost state due to quenching. As we are using a mixed action, with

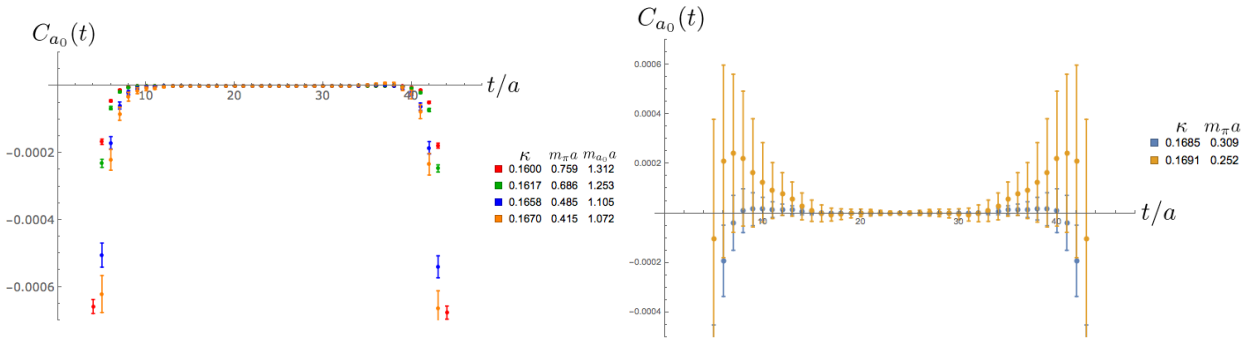


Figure 5.4: $a_0$ correlators at zero spatial momentum for a range of values of $\kappa$. The left-hand plot shows heavier values of $\kappa$, the right shows lighter values, including including $\kappa_\ell = 0.1691$.

staggered sea quarks and Wilson valence quarks, it would not be surprising if there are some artifacts related to partial quenching. To estimate $m_{a_0}a$, the correct sign points for the four smaller values of $\kappa$ were fit to an exponential, seen in Fig. 5.4 and 5.5. The square of the resulting masses were plotted against $1/\kappa$ and extrapolated to $1/\kappa_\ell = 1/0.1691$, as seen in Fig. 5.6. This resulted in an estimate of $m_{a_0}a = 0.985 \pm 0.065$ where the errors only represent the mean prediction bands of the linear fit at 68.27% confidence and do not take into account possible deviation from a linear relation between $m_{a_0}^2$ and $1/\kappa$ or systematic effects on the value of the mass at larger values of $1/\kappa$.

### *5.3.2 $O^\pi$ Correlator*

In measuring both $O^\pi$ and $O^{a_0}$, measurements at points related by lattice symmetries, reflections about each space-time direction and rotations in space, were averaged over. In order to reduce discretization effects only points which are not along the axes of the lattice, such as $(1,0,0,0), (0,5,0,0)$ are included. The measurement of the two terms which make up $O^\pi$, seen in Eq. 5.18, were found to be nearly identical. The correlation of the measurement of each term on a given configuration, averaged over all configurations is 0.9997 and were found to have the same fit parameters for all fits attempted. Initial fits of the tail of the

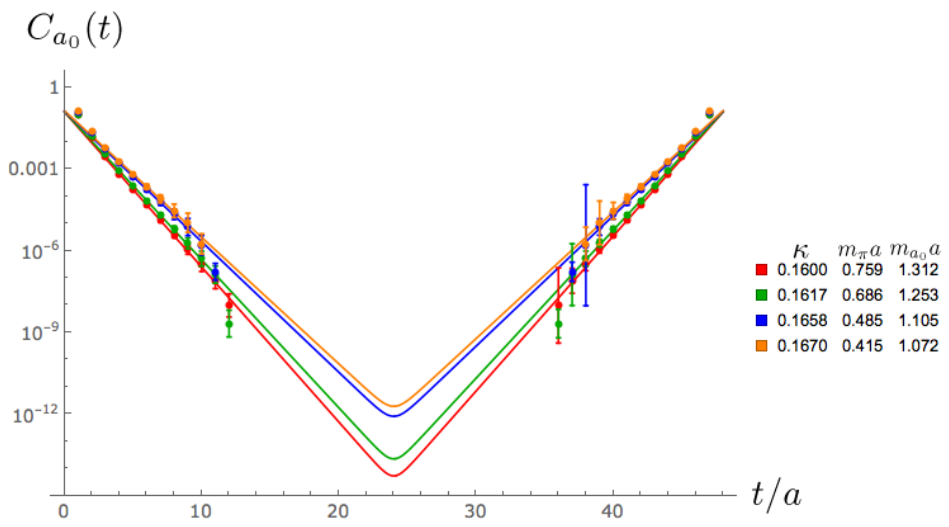


Figure 5.5: $a_0$ correlators for heavier values of $\kappa$, on a negative log scale with a fit to points shown.

correlator, $5.5 < |x|/a < 10$, to the form of a scalar propagator resulted in a mass which was significantly less than the pion mass. Suspecting that this is due to the pion being a long lived state and noting that the region $5.5 < |x|/a < 10$ includes distances large relative to the lattice size in the spatial direction, $L = 16$, the correlator was fit to a sum of scalar propagators, including the 26 nearest spatial images,

$$C(x) = a\left(\frac{K_1(m|x|)}{|x|} + \sum_{x_{\text{img}}} \frac{K_1(m|x - x_{\text{img}}|)}{|x - x_{\text{img}}|}\right) \tag{5.19}$$

$$x_{\text{img}} \in (\pm L, 0, 0, 0), (0, \pm L, 0, 0), (\pm L, \pm L, 0, 0), (\pm L, 0 \mp L, 0), (\pm L, \mp L, \pm L, 0)...$$

where $K_1$ is the modified bessel function of the first kind. Fitting to the tail resulted in the fit parameters summarized in Table 5.1 which includes a mass of $m = 0.250$ which is close to the pion mass $m_\pi a = 0.252$. Points generated using the fit of the form Eq. 5.19 using these fit parameters are shown in Fig. 5.7. While this is a good fit for the tail of the measurement, it is a poor fit for the early points due to excited pion states. To also include the first excited

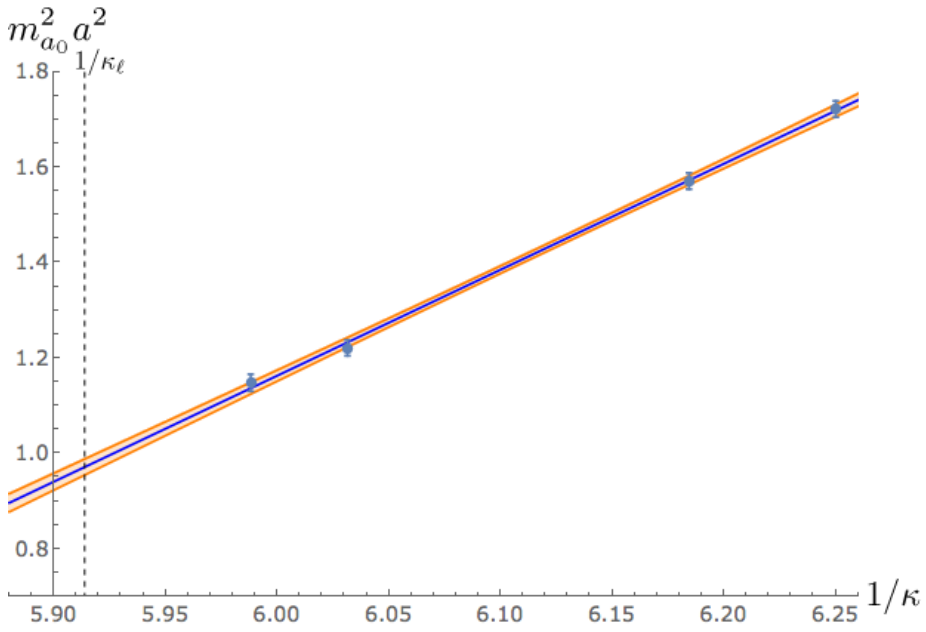


Figure 5.6: $a_0$ mass squared versus $\kappa^{-1}$. Shaded region shows mean prediction bands of the linear fit at 68.27% confidence. The dashed line indicates $1/\kappa_\ell = 1/0.1691$. Error bars represent standard error of fit in determining $a_0$ masses.

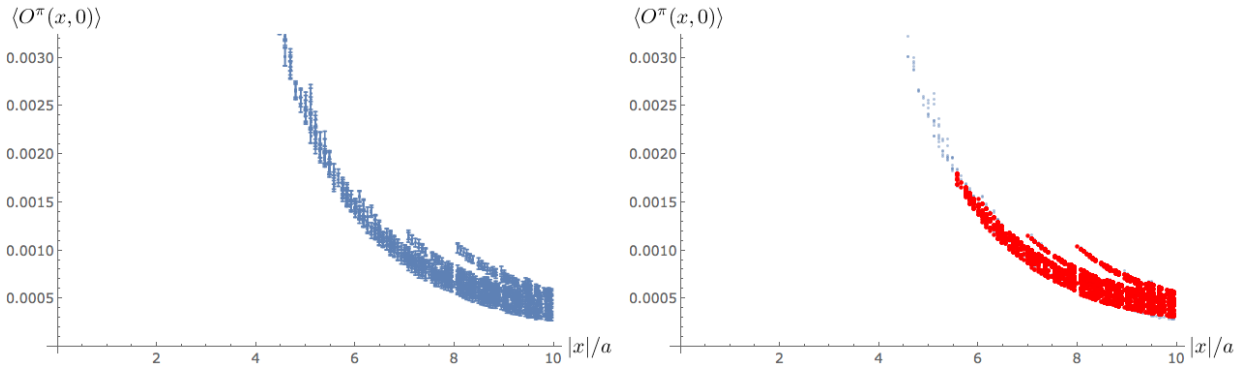


Figure 5.7: Tail of measurement of $O^\pi$ versus $|x|/a$. Left-hand plot shows points with errors, the right-hand plot shows data points in light blue along with points generated by the fit function, Eq. 5.19, using parameters found in Table 5.1.

Table 5.1: Fit parameters for tail of $O^{\pi}$ correlator

| | Estimate | Standard Error |
|---|---|---|
| a | 0.02672 | 0.00015 |
| m | 0.25001 | 0.00048 |

Table 5.2: Fit parameters for $O^{\pi}$ correlator

| | Estimate | Standard Error |
|---|---|---|
| a | 0.026849 | 0.000076 |
| b | 2.451 | 0.080 |
| $\mu$ | 1.605 | 0.015 |

pion state we have fit to the range $0 < |x|/a < 10$ using the form,

$$C(x) = a\left(\frac{K_1(0.25001|x|)}{|x|} + \sum_{x_{\rm img}} \frac{K_1(0.25001|x - x_{\rm img}|)}{|x - x_{\rm img}|}\right) + b\left(\frac{K_1(\mu|x|)}{|x|} + \sum_{x_{\rm img}} \frac{K_1(\mu|x - x_{\rm img}|)}{|x - x_{\rm img}|}\right) \ . \tag{5.20}$$

The fit parameters are summarized in Table 5.2. Points generated using the fit of the form Eq. 5.19 using these fit parameters are shown in Fig. 5.8. The last step is to subtract this fit from the correlator and look at the remainder, shown in Fig. 5.9. It appears that points with $|x|/a \lesssim 2.5$ are indistinguishable from noise, leaving a very small number of points to analyze when combined with the $O^{a_0}$ measurement.

### *5.3.3 $O^{a_0}$ Correlator*

Just as with $O^{\pi}$, the results for the two terms that make up $O^{a_0}$, seen in Eq. 5.17, were found to be nearly identical. The correlation of the measurement of each term on a given

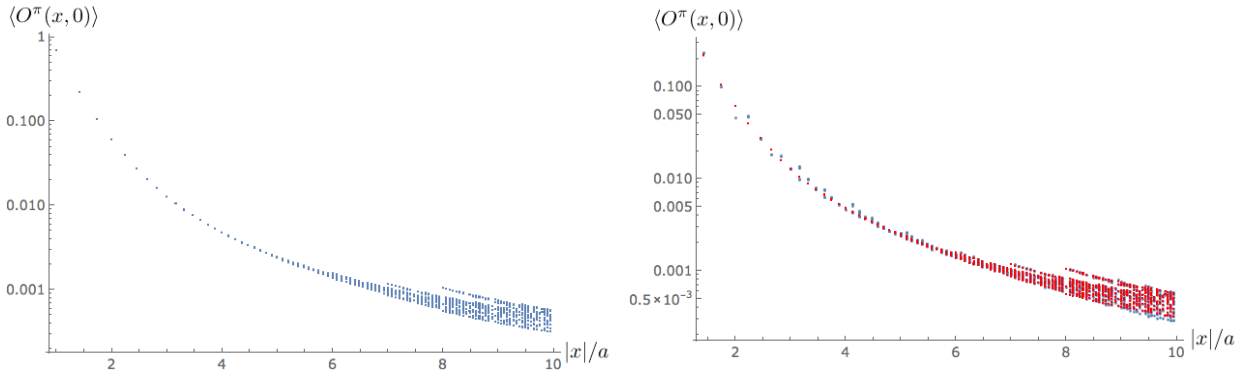


Figure 5.8: Measurement of $O^\pi$ versus $|x|/a$ on a log scale. Left-hand plot shows results with errors, right-hand plot shows results (without errors)along with the corresponding fit points generated from Eq. 5.20 using parameters found in Table 5.1.

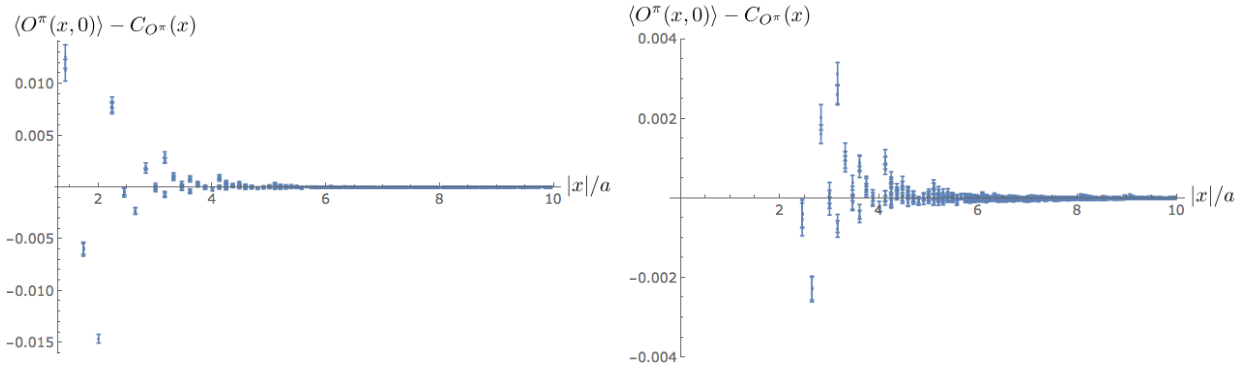


Figure 5.9: Remainder of the measurement of $O^\pi$ versus $|x|/a$ after subtracting Eq. 5.19 using parameters found in Table 5.2. The right-hand plot shows a magnified version of the same data. Error bars come from averaging over configurations and not taking into account any error on the fit.

configuration, averaged over all configurations is 0.9995 and the fit parameters were identical for all fits attempted. As seen above for the $a_0$ correlator at $\kappa_\ell = 0.1691$, the $O^{a_0}$ correlator changes sign, as seen in Fig. 5.10. Changing sign suggests, as it did for the $a_0$ correlator, that

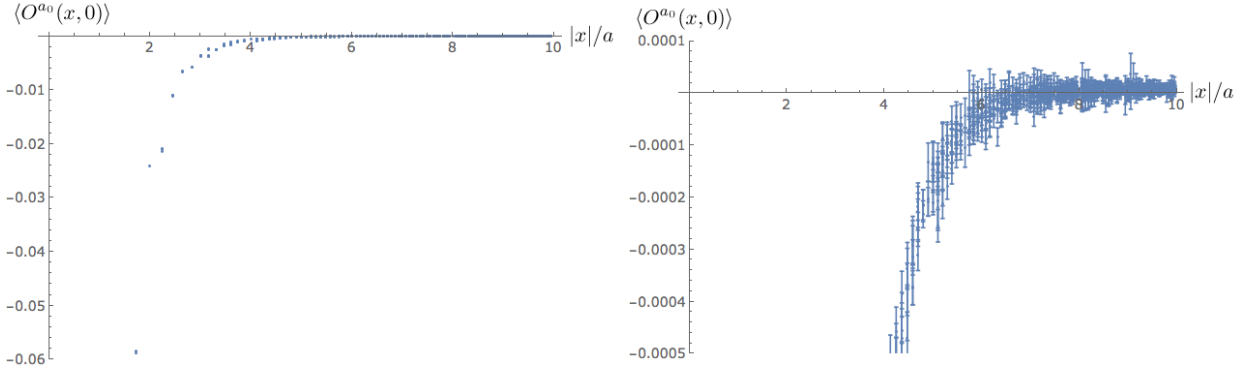


Figure 5.10: Measurement of $O^{a_0}$ versus $|x|/a$. The right-hand plot shows a magnified version of the same data

the measurement may be contaminated by the effects of using a mixed action [2]. We have fit the data in the range $2 < |x|/a < 6$, after which the majority of the points have changed sign and fitting to a strictly positive function will not yield a good fit, and before there is expected to be contamination from excited states. As in the $O^{\pi}$ case, the correlator was fit to a sum of scalar propagators, including the 26 nearest spatial images, shown in Eq. 5.19. The fit parameters are shown in Table 5.3 with the fit shown in Fig. 5.11. The mass parameter was found to be $m = 1.391$ which is significantly larger than than the estimated $a_0$ mass, $m_{a_0}a = 0.985$. This can be taken either as an indication that the extrapolation shown in Fig. 5.6 was not justified or a more careful fit, like the one used for $O^{\pi}$ in Eq. 5.20 including exciting states, is needed. Unfortunately, since the tail of the correlator has the wrong sign, it is not feasible to fit to an additional propagator in the limited allowed range.

Subtracting the fit from the $O^{a_0}$ measurement is shown in Fig. 5.12. Like with $O^{\pi}$, the resulting data looks rather noisy, such that it seem unlikely that the combination of $O^{\pi}$ and

[2]The connection of the sign change to the effects of partial quenching is not so theoretically clear cut here as in the $a_0$ correlator discussed above. This is because the operators used to create and destroy the states are not hermitian conjugates, and thus the contribution from all states does not need to have the same sign. However, in the approximation that $s\bar{s}$ can be replaced by the identity element, the connection between sign-change and partial quenching is appropriate.

Table 5.3: Fit parameters for $O^{a_0}$ correlator

| | Estimate | Standard Error |
|---|---|---|
| a | -0.781 | 0.048 |
| m | 1.258 | 0.017 |

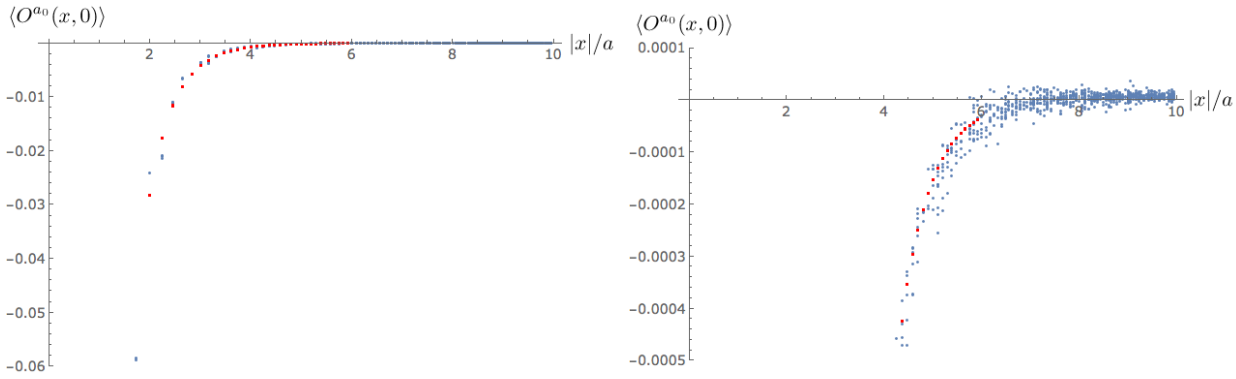


Figure 5.11: Measurement of $O^{a_0}$ versus $|x|/a$ with fit to Eq. 5.19 using parameters in Table 5.3. The right-hand plot shows a magnified version of the same data. Error bars are not shown to improve visibility.

$O^{a_0}$ will reproduce the $1/x^4$ behavior seen in Eq. 5.8.

### *5.3.4 Full $O = \frac{1}{4}(O^{\pi} + O^{a_0})$ Correlator*

The full correlator, $O = \frac{1}{4}(O^{\pi} + O^{a_0})$ of Eq. 5.14 leads to the result in Fig. 5.3. Subtracting both the fit from the $O^{\pi}$ and $O^{a_0}$ measurements is shown in Fig. 5.13. As expected from the subtractions in the $O^{\pi}$ and $O^{a_0}$, seen in Fig. 5.9 and Fig. 5.12, the remaining data is too noisy to hope to see the $1/x^4$ behavior of Eq. 5.8, as there are only three data points before the data changes sign.

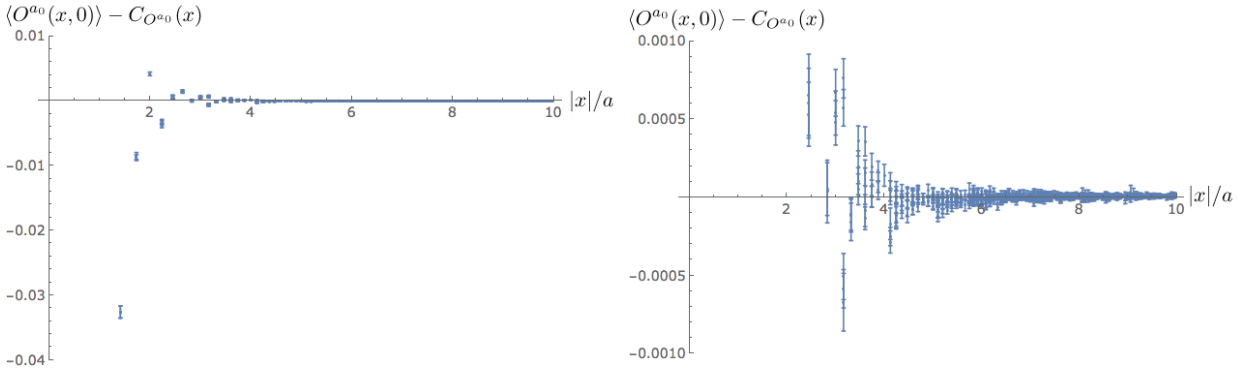


Figure 5.12: Remainder of the measurement of $O^{a_0}$ versus $|x|/a$ after subtracting Eq. 5.19 using parameters found in Table 5.1. The right-hand plot shows a magnified version of the same data. Error bars come from averaging over configurations and not taking into account any error on the fit.

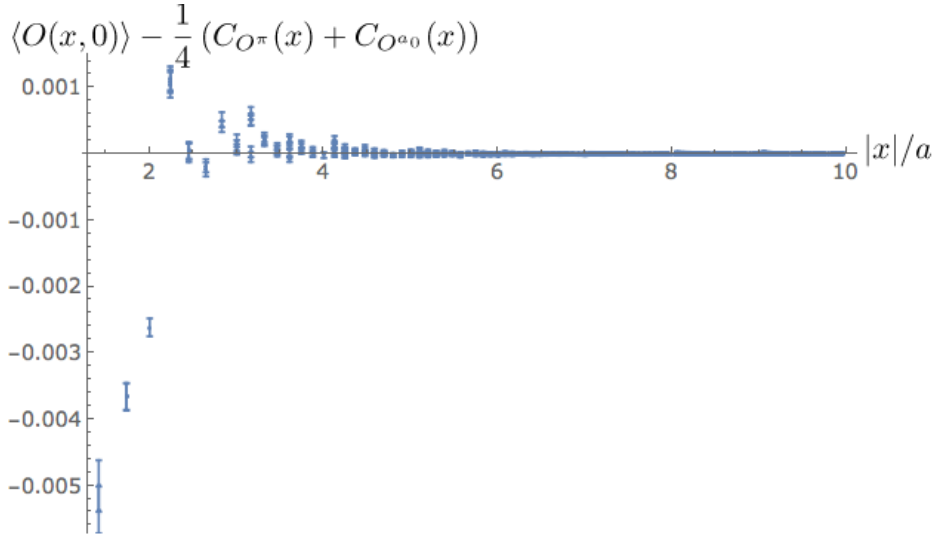


Figure 5.13: Remainder of the measurement of $O = \frac{1}{4}\left(O^\pi + O^{a_0}\right)$ versus $|x|/a$ after subtracting 1/4 multiplied by Eq. 5.19 using the parameters found in Table 5.2 and Table 5.3. Error bars come from averaging over configurations and not taking into account any error on the fit.

### *5.4 Conclusions and future directions*

Ultimately, the remainder of the results for the correlator Eq. 5.14 after subtracting the $a_0$ and pion states was too noisy to see if the expected $1/x^4$ behavior of the Greens function Eq. 5.8 exists. We believe, however, that the strategy we have used, i.e. breaking the Greens function into $a_0$ and pion-like components, is a good approach. We suspect that the largest systematic issues with our simulation were using a mixed action which did not preserve chiral symmetry and using too large of a lattice spacing. The first issue can be addressed by using both a sea and valence action which preserves chiral symmetry, such as domain wall fermions. The second issue can be addressed by using configurations with a smaller lattice spacing. Both of these solutions present challenges, as both require greater computational resources. It is possible that this increased computational cost can be somewhat mitigated by using somewhat heavier quark masses. As discussed in Sec. 5.1, the leading perturbative correction due to explicit breaking of chiral symmetry by quark masses is proportional to $m_u m_d m_s/x^{10}$, seen in Eq. 5.9. There is trade-off between using a smaller spacing versus using heavier quark masses that can be investigated and it is possible that this leading perturbative correction could be included in a fit to the remainder of the measurement of the operator Eq. 5.14. While it may be computationally difficult, we believe it is worthwhile to continue to pursue this line of investigation, as can help open a portal into measuring instanton effects directly on the lattice.

# Chapter 6

# CONCLUSION

In chapters 2 through 4 of this thesis we have shown how the phase diagram of LQCD is effected by the inclusion of non-degenerate light quark masses and electromagnetism both with and without twisting. Also included was some clarification about how twisting must be performed in the case with electromagnetism. These results are increasingly relevant as lattice practitioners strive for sub-percent level accuracy by working in the Aoki regime with all isospin breaking effects. This is even more true for collaborations which use twisted mass fermions where the process of tuning to maximal twist becomes more complicated when both non-degenerate light quark masses and electromagnetic effects are taken into account. The work presented above points out some of the potential pitfalls and offers potential solutions for future simulations.

In chapter 5 we have made a first attempt at directly measuring instanton effects in chirality violating Greens functions. A successful measurement of such an operator could confirm recent work in Ref. [24], opening a new window into studying instantons analytically. While our work did not produce useful results, we have elucidated some of the possible issues in such a measurement and have introduced a procedure which can be used in future, more resource intensive calculation.

The two topics described in this thesis are related by their connection to chiral symmetry breaking in LQCD. The first study was an analytic investigation and the later a primarily computational one. While mostly unrelated to each other, we believe both studies have helped shine light on aspects of chiral symmetry breaking on the lattice, an increasingly relevant topic in the modern frontier of highly accurate LQCD research.

# BIBLIOGRAPHY


[1] A. Abdel-Rehim, Ph. Boucaud, N. Carrasco, A. Deuzeman, P. Dimopoulos, et al. A first look at maximally twisted mass lattice QCD calculations at the physical point. *PoS*, LATTICE2013:264, 2013.

[2] G. Akemann, J. T. Lenaghan, and K. Splittorff. Dashen's phenomenon in gauge theories with spontaneously broken chiral symmetries. *Phys. Rev.*, D65:085015, 2002.

[3] Sinya Aoki. New Phase Structure for Lattice QCD with Wilson Fermions. *Phys.Rev.*, D30:2653, 1984.

[4] Sinya Aoki, Yasumichi Aoki, Claude Bernard, Tom Blum, Gilberto Colangelo, et al. Review of lattice results concerning low energy particle physics. 2013.

[5] Sinya Aoki and Michael Creutz. Pion masses in 2-flavor QCD with $\eta$ condensation. *Phys.Rev.Lett.*, 112:141603, 2014.

[6] Gunnar S. Bali, Sara Collins, and Andreas Schafer. Effective noise reduction techniques for disconnected loops in Lattice QCD. *Comput. Phys. Commun.*, 181:1570–1583, 2010.

[7] Oliver Bar, Maarten Golterman, and Yigal Shamir. Flavor symmetry breaking in lattice QCD with a mixed action. *Phys.Rev.*, D83:054501, 2011.

[8] Remi Baron et al. Computing K and D meson masses with $N_{\{}f\} = 2{+}1{+}1$ twisted mass lattice QCD. *Comput.Phys.Commun.*, 182:299–316, 2011.

[9] S. Basak et al. Finite-volume effects and the electromagnetic contributions to kaon and pion masses. *PoS*, LATTICE2014, 2014.

[10] A. Bazavov et al. Nonperturbative QCD Simulations with 2+1 Flavors of Improved Staggered Quarks. *Rev. Mod. Phys.*, 82:1349–1417, 2010.

[11] J. Beringer et al. Review of Particle Physics (RPP). *Phys.Rev.*, D86:010001, 2012.

[12] Tanmoy Bhattacharya, Rajan Gupta, Weonjong Lee, Stephen R. Sharpe, and Jackson M.S. Wu. Improved bilinears in lattice QCD with non-degenerate quarks. *Phys.Rev.*, D73:034504, 2006.

[13] Thomas Blum, Taku Izubuchi, and Eigo Shintani. New class of variance-reduction techniques using lattice symmetries. *Phys. Rev.*, D88(9):094503, 2013.

[14] Sz. Borsanyi, S. Durr, Z. Fodor, C. Hoelbling, S.D. Katz, et al. Ab initio calculation of the neutron-proton mass difference. *Science*, 347:1452–1455, 2015.

[15] N. Carrasco, A. Deuzeman, P. Dimopoulos, R. Frezzotti, V. Gimenez, et al. Up, down, strange and charm quark masses with Nf = 2+1+1 twisted mass lattice QCD. 2014.

[16] Michael Creutz. Spontaneous violation of CP symmetry in the strong interactions. *Phys.Rev.Lett.*, 92:201601, 2004.

[17] Michael Creutz. Confinement, chiral symmetry, and the lattice. *Acta Phys.Slov.*, 61:1–127, 2011.

[18] Michael Creutz. *(private communications and seminars)*, 2013.

[19] Roger F. Dashen. Some features of chiral symmetry breaking. *Phys.Rev.*, D3:1879–1889, 1971.

[20] C. T. H. Davies, E. Follana, I. D. Kendall, G. Peter Lepage, and C. McNeile. Precise determination of the lattice spacing in full lattice QCD. *Phys. Rev.*, D81:034506, 2010.

[21] Zohreh Davoudi and Martin J. Savage. Finite-Volume Electromagnetic Corrections to the Masses of Mesons, Baryons and Nuclei. *Phys.Rev.*, D90:054503, 2014.

[22] G.M. de Divitiis, P. Dimopoulos, R. Frezzotti, V. Lubicz, G. Martinelli, et al. Isospin breaking effects due to the up-down mass difference in Lattice QCD. *JHEP*, 1204:124, 2012.

[23] G.M. de Divitiis et al. Leading isospin breaking effects on the lattice. *Phys.Rev.*, D87(11):114505, 2013.

[24] Michael Dine, Patrick Draper, and Guido Festuccia. Instanton Effects in Three Flavor QCD. *Phys. Rev.*, D92(5):054004, 2015.

[25] Michael Dine, Guido Festuccia, Lawrence Pack, and Weitao Wu. Reliable Semiclassical Computations in QCD. *Phys. Rev.*, D82:065015, 2010.

[26] G. Ecker, J. Gasser, A. Pich, and E. de Rafael. The Role of Resonances in Chiral Perturbation Theory. *Nucl.Phys.*, B321:311, 1989.

[27] Robert G. Edwards and Balint Joo. The Chroma software system for lattice QCD. *Nucl. Phys. Proc. Suppl.*, 140:832, 2005. [,832(2004)].

[28] R. Frezzotti and G.C. Rossi. Chirally improving Wilson fermions. 1. O(a) improvement. *JHEP*, 0408:007, 2004.

[29] R. Frezzotti and G.C. Rossi. Twisted mass lattice QCD with mass nondegenerate quarks. *Nucl.Phys.Proc.Suppl.*, 128:193–202, 2004.

[30] Roberto Frezzotti, Pietro Antonio Grassi, Stefan Sint, and Peter Weisz. Lattice QCD with a chirally twisted mass term. *JHEP*, 0108:058, 2001.

[31] J. Gasser and H. Leutwyler. Chiral Perturbation Theory: Expansions in the Mass of the Strange Quark. *Nucl.Phys.*, B250:465, 1985.

[32] Christof Gattringer and Christian B. Lang. Quantum chromodynamics on the lattice. *Lect. Notes Phys.*, 788:1–343, 2010.

[33] Maarten Golterman. Applications of chiral perturbation theory to lattice QCD. pages 423–515, 2009.

[34] Maarten Golterman and Yigal Shamir. Vacuum alignment and lattice artifacts: Wilson fermions. *Phys.Rev.*, D89:054501, 2014.

[35] R. Gupta, Gregory Kilcup, and Stephen R. Sharpe. ONE LOOP LATTICE VACUUM ENERGY. *Phys.Lett.*, B147:339, 1984.

[36] Maxwell T. Hansen and Stephen R. Sharpe. Constraint on the Low Energy Constants of Wilson Chiral Perturbation Theory. *Phys.Rev.*, D85:014503, 2012.

[37] Masashi Hayakawa and Shunpei Uno. QED in finite volume and finite size scaling effect on electromagnetic properties of hadrons. *Prog.Theor.Phys.*, 120:413–441, 2008.

[38] Derek P. Horkel and Stephen R. Sharpe. Phase diagram of nondegenerate twisted mass fermions. *Phys.Rev.*, D90(9):094508, 2014.

[39] Derek P. Horkel and Stephen R. Sharpe. Impact of electromagnetism on phase structure for Wilson and twisted-mass fermions including isospin breaking. *Phys. Rev.*, D92(7):074501, 2015.

[40] Derek P. Horkel and Stephen R. Sharpe. Phase structure with nonzero $\Theta_{\rm QCD}$ and twisted mass fermions. *Phys. Rev.*, D92:094514, 2015.

[41] David B. Kaplan. Five lectures on effective field theory. 2005.

[42] Mario Kieberg, Kim Splittorff, Jac Verbaarschot, and Savvas Zafeiropoulos. *(talk at Lattice 2014)*, 2014.

[43] Jonathan Lenaghan and Thomas Wilke. Mesoscopic QCD and the theta vacua. *Nucl. Phys.*, B624:253–282, 2002.

[44] Nilmani Mathur, A. Alexandru, Y. Chen, S. J. Dong, Terrence Draper, I. Horvath, F. X. Lee, K. F. Liu, S. Tamhankar, and J. B. Zhang. Scalar Mesons a0(1450) and sigma(600) from Lattice QCD. *Phys. Rev.*, D76:114505, 2007.

[45] Gernot Munster. On the phase structure of twisted mass lattice QCD. *JHEP*, 0409:035, 2004.

[46] Gernot Munster and Tobias Sudmann. Twisted mass lattice QCD with non-degenerate quark masses. *JHEP*, 0608:085, 2006.

[47] K.A. Olive et al. Review of Particle Physics. *Chin.Phys.*, C38:090001, 2014.

[48] A. Portelli et al. Electromagnetic corrections to light hadron masses. *PoS*, LATTICE2010:121, 2010.

[49] Antonin Portelli. Review on the inclusion of isospin breaking effects in lattice calculations. *PoS*, KAON13:023, 2013.

[50] Gautam Rupak and Noam Shoresh. Chiral perturbation theory for the Wilson lattice action. *Phys.Rev.*, D66:054503, 2002.

[51] Stefan Scherer and Matthias R. Schindler. A Primer for Chiral Perturbation Theory. *Lect. Notes Phys.*, 830:pp.1–338, 2012.

[52] Luigi Scorzato. Pion mass splitting and phase structure in twisted mass QCD. *Eur.Phys.J.*, C37:445–455, 2004.

[53] Stephen R. Sharpe. Observations on discretization errors in twisted-mass lattice QCD. *Phys.Rev.*, D72:074510, 2005.

[54] Stephen R. Sharpe and Noam Shoresh. Physical results from unphysical simulations. *Phys.Rev.*, D62:094503, 2000.

[55] Stephen R. Sharpe and Noam Shoresh. Partially quenched chiral perturbation theory without Phi0. *Phys.Rev.*, D64:114510, 2001.

[56] Stephen R. Sharpe and Jr Singleton, Robert L. Spontaneous flavor and parity breaking with Wilson fermions. *Phys.Rev.*, D58:074501, 1998.

[57] Stephen R. Sharpe and Jackson M.S. Wu. The Phase diagram of twisted mass lattice QCD. *Phys.Rev.*, D70:094029, 2004.

[58] Stephen R. Sharpe and Jackson M.S. Wu. Twisted mass chiral perturbation theory at next-to-leading order. *Phys.Rev.*, D71:074501, 2005.

[59] Stephen.R. Sharpe. Applications of Chiral Perturbation theory to lattice QCD. 2006.

[60] Edward V. Shuryak. Why is a nucleon bound? *Nucl. Phys.*, A606:201–214, 1996.

[61] Andrei V. Smilga. QCD at theta similar to pi. *Phys.Rev.*, D59:114021, 1999.

[62] K. Symanzik. Continuum Limit and Improved Action in Lattice Theories. 1. Principles and phi**4 Theory. *Nucl.Phys.*, B226:187, 1983.

[63] K. Symanzik. Continuum Limit and Improved Action in Lattice Theories. 2. O(N) Nonlinear Sigma Model in Perturbation Theory. *Nucl.Phys.*, B226:205, 1983.

[64] Nazario Tantalo. Isospin Breaking Effects on the Lattice. 2013.

[65] Andre Walker-Loud and Jackson M.S. Wu. Nucleon and Delta masses in twisted mass chiral perturbation theory. *Phys.Rev.*, D72:014506, 2005.

[66] Edward Witten. {Some Inequalities Among Hadron Masses}. *Phys.Rev.Lett.*, 51:2351, 1983.

# Appendix A

# APPENDIX TO CHAPTER 3

## *A.1 Relating lattice masses to those in $\chi$PT*

In this appendix we describe how bare lattice masses used in simulations with Wilson-like fermions are related to the masses $m_u$ and $m_d$ appearing in $\chi$PT (contained in the mass matrix $M$). This discussion draws heavily from the results of Ref. [12]. We do not consider the impact of electromagnetism here; this is discussed in the subsequent appendix.

We must assume that the number of dynamical quarks in the underlying simulations is $N_f = 3$ (up, down and strange) or $N_f = 4$ (adding charm). Working with up and down quarks alone turns out not to be sufficient, but in any case this is not the physical theory. We must also have that $am_f \ll 1$ for all flavors $f$, so that an expansion in these quantities makes sense. This condition is met by state-of-the-art simulations. Note that this condition is much weaker than the requirement that the quarks are light in the sense of $\chi$PT, which is $m_f \ll \Lambda_{\mathrm{QCD}}$. In the main text, we assume the latter condition holds only for up and down quarks.

Let $m_{0,f}$ be the bare dimensionless lattice mass for flavor $f$ (i.e. the mass appearing in the lattice action). Because of the additive renormalization induced by explicit chiral symmetry breaking, unrenormalized quark masses are given by

$$\widetilde{m}_f = \frac{m_{0,f} - m_{cr}}{a}\,, \tag{A.1}$$

where $m_{cr}$ is the (dimensionless) critical mass for the given number of dynamical flavors. Methods to determine $m_{cr}$ are described below. Then, as shown in Ref. [12], renormalized

masses are given by[1]

$$m_f = Z_m \left[ \widetilde{m}_f + (r_m - 1) \frac{\sum_f \widetilde{m}_f}{N_f} + \mathcal{O}(a\widetilde{m}^2) \right] . \tag{A.2}$$

Here $Z_m$ is the renormalization constant for flavor nonsinglet mass combinations such as $\epsilon_q = (m_u - m_d)/2$, while $Z_m r_m$ is the corresponding constant for the average quark mass. $r_m - 1$ is a finite constant, arising first at $\mathcal{O}(g^4)$ in perturbation theory. By implementing continuum Ward-Takahashi identities, one can determine $r_m$ nonperturbatively for $N_f = 3$ and 4, although not for $N_f = 2$ [12]. This is the reason for the restriction on $N_f$ noted above. We assume here that $r_m$ has been calculated in this way.

Equation (A.2) shows that the renormalized mass $m_f$ does not vanish when $\tilde{m}_f = 0$ if other flavors are massive. Specifically, for the up and down quarks we have

$$\begin{aligned} m_u + m_d = {} & Z_m \frac{1+r_m}{2} (\widetilde{m}_u + \widetilde{m}_d) \\ & + Z_m \frac{r_m - 1}{2} (\widetilde{m}_s + \widetilde{m}_{ch}) , \end{aligned} \tag{A.3}$$

$$m_u - m_d = Z_m (\tilde{m}_u - \tilde{m}_d) . \tag{A.4}$$

(Here we we have chosen $N_f = 4$ for definiteness; the result for $N_f = 3$ is similar.) Thus the two-flavor massless point receives an overall additive shift due to the strange and charm quarks, and we also see explicitly the difference between singlet and nonsinglet renormalizations.

These results imply that, in terms of unrenormalized masses, the phase diagrams of Fig. 3.1 would be translated in the vertical direction (due to the additive mass shift) and stretched by *different* factors in the vertical and horizontal directions. The respective stretch factors are $B_0 Z_m (1 + r_m)/2$ and $B_0 Z_m$. If, however, $r_m$ is known, then the two stretch factors can be made equal by applying a finite renormalization to remove the $(1 + r_m)/2$ factor. Knowledge of $Z_m$ is, however, not useful, since it always appears multiplied by the unknown LEC $B_0$.

---

[1]The correction terms of $\mathcal{O}(a\tilde{m}^2)$ in (A.2) are subleading in our power-counting and will be dropped henceforth.

We would like to be able to remove the additive mass shift in Eq. (A.3). To do so we consider how the critical mass $m_{cr}$ is determined. The expressions above assume that it has been obtained by doing simulations with $N_f$ *degenerate* quarks of mass $m$, and equating $m_{cr}$ to the value of $m$ at which the "PCAC mass" vanishes. This is equivalent to imposing

$$\langle \pi^+ | \partial_\mu (\bar{u} \gamma_\mu \gamma_5 d) | 0 \rangle \Big|_{m=m_{cr}} = 0 \,. \tag{A.5}$$

If, instead, one imposes this condition by varying $m = m_u = m_d$, with $m_s$ and $m_{ch}$ held fixed at their physical values, then the $m_{cr}$ so obtained automatically includes the shift due to loops of strange and charm quarks. This is because one is enforcing a consequence of chiral symmetry in the two-flavor subsector. With this new choice of $m_{cr}$, and with the adjustment of stretch factors described above, the phase diagrams of Fig. 3.1 apply directly for lattice masses $\tilde{m}_f$.

This new choice of $m_{cr}$ has a second advantage: it removes an additional shift of $O(a)$ in the relation between bare quark masses and the masses appearing in $\chi$PT. As explained in Ref. [56], this shift is caused by the $\mathcal{O}(a)$ clover term in the Symanzik effective action (and is thus absent for nonperturbatively improved Wilson fermions). In the main text it is assumed that this shift has been removed.

Since we include $\mathcal{O}(a^2)$ terms in the main text, we must determine how they impact the considerations above. There is no further shift in the quark masses at this order—this next occurs at $\mathcal{O}(a^3)$ [53]. However, as illustrated by Fig. 3.1, the $\mathcal{O}(a^2)$ terms do impact the phase diagram. This means that, in general, one cannot use the vanishing of the PCAC mass to determine $m_{cr}$ with untwisted Wilson fermions. For example, if one is in the first-order scenario [Fig. 3.1(b) along the $\hat{m}_q$ axis], then the PCAC mass simply does not vanish for any $\hat{m}_q$. Instead, one must introduce a twisted component to the mass, $\mu \sim \mathcal{O}(a)$, and then enforce the vanishing of the PCAC mass (in the so-called "twisted basis"). Extrapolating the result linearly to $\mu = 0$ yields a result for $m_{cr}$ that has errors of $\mathcal{O}(a^3)$, which is sufficiently accurate for our analysis. For a detailed discussion of this point see Ref. [53].

In summary, by determining $r_m$ from Ward identities, and the critical mass from the

PCAC mass condition with twisted-mass quarks, one can obtain lattice quark masses which are proportional to those appearing in $\chi$PT at the order we work. Specifically, we find

$$\frac{\widehat{m}_q}{B_0 Z_m} = \frac{1+r_m}{2}(\tilde{m}_u+\tilde{m}_d) \text{ and } \frac{\widehat{\epsilon}_q}{B_0 Z_m} = (\tilde{m}_u-\tilde{m}_d)\,, \tag{A.6}$$

where $\widehat{m}_q$ and $\widehat{\epsilon}_q$ are the quantities appearing in the chiral potential of Eq. (3.5).

This analysis can be straightforwardly extended to arbitrary twist. We begin with maximal twist, for which the mass matrix in $\chi$PT is given by Eq. (3.28), and the relevant bare masses are $\mu_0$ and $\eta_0$ of Eq. (3.24). In this case there is no additive renormalization, but the presence of different renormalization factors for singlet and nonsinglet masses remains. Using the results of Ref. [12], we find[2]

$$\frac{\widehat{m}_q}{B_0 Z_m} = \frac{Z_S}{Z_P}\frac{1+r_P}{r_P}\mu_0 \text{ and } \frac{\widehat{\epsilon}_q}{B_0 Z_m} = \frac{Z_S}{Z_P}\eta_0\,. \tag{A.7}$$

Here $Z_S/Z_P$ and $r_P$ are finite constants, both of which can be determined from Ward identities for $N_f = 3$ and 4, but not for $N_f = 2$ [12]. Like $r_m$, $r_P$ begins at $\mathcal{O}(g^4)$ in perturbation theory.

At arbitrary twist one has four bare masses, and they are related to the corresponding four renormalized masses using the same renormalization factors as given in Eqs. (A.6) and (A.7).

Finally, we stress that the analysis presented here does not include electromagnetic effects. The dominant such effect is that the critical mass $m_{cr}$ has to be chosen differently for the up and down quarks, and is discussed in the following appendix. A subdominant, but still important, effect is that the renormalization factors now depend not only on $\alpha_S$ but also on $\alpha_{\rm EM}$. The latter dependence can presumably be adequately captured using perturbation theory. The formulae given above still hold if one uses the new critical masses and renormalization factors.

[2]Specifically, we have used $Z_m = 1/Z_S$ and $r_m = 1/r_S$.

### *A.2 Determining the critical masses in the presence of electromagnetism*

The analysis of the previous appendix must be extended when electromagnetism is included, due to the presence of charge-dependent self energy corrections proportional to $\alpha_{\rm EM}/a$. This implies that the critical masses for up and down quarks differ, and we label them $m_{cr,u}$ and $m_{cr,d}$, respectively. In Ref. [23] two methods for a nonperturbative determination of these critical masses are proposed. One of these (the method used in practice in Ref. [23]) involves only up and down quarks, and thus can be implemented, and therefore checked, within SU(2) W$\chi$PT. We do so in this appendix, finding that *the method does not fix both critical masses*, but rather constrains them to lie in a one-dimensional subspace of the $m_{cr,u}$—$m_{cr,d}$ plane. We then provide an additional condition that does completely determine $m_{cr,u}$ and $m_{cr,d}$.

The tuning conditions require the use of twisted-mass quarks, although the resulting values of $m_{cr,u}$ and $m_{cr,d}$ apply for both Wilson and twisted-mass quarks. Thus the lattice quark Lagrangian is given by Eq. (3.24). We can write the mass matrix in two useful forms

$$m_0 + \tau_3\epsilon_0 + i\gamma_5\tau_3\mu_0 + i\gamma_5\eta_0 = \begin{pmatrix} m_{0,u} + i\gamma_5\mu_{0,u} & 0 \\ 0 & m_{0,d} - i\gamma_5\mu_{0,d} \end{pmatrix} . \tag{A.8}$$

The tuning proceeds by first choosing bare twisted masses $\mu_{0,u}$ and $\mu_{0,d}$ such that, when multiplicatively renormalized as described in the previous appendix, they give rise, respectively, to the desired physical up and down quark masses.[3] The negative sign multiplying $\mu_{0,d}$ is chosen to correspond to a $\tau_3$ twist. The second step is to tune the untwisted masses $m_{0,u}$ and $m_{0,d}$ to their critical values such that the (additively) renormalized untwisted masses vanish.

The method of determining $m_{cr}$ used in the previous section is no longer useful—the vanishing of the PCAC mass is a condition based on the recovery of the chiral SU(2) group, but this group is explicitly broken by electromagnetism. The workaround proposed in Ref. [23] is to add to the sea quarks (labeled $u_S$ and $d_S$) a pair of valence quarks, $u_V$ and $d_V$, each

[3] In fact, the tuning can be done using any values of the twisted masses which respect our power counting. The critical masses do not depend on the twisted masses at the order we work.

of which has the same charge and untwisted mass as the corresponding sea quark, but has opposite twisted mass.[4] Thus $(u_S, u_V)$ and $(d_V, d_S)$ each form a twisted pair. The key point is that, within each pair, the $\mathcal{O}(\alpha_{\rm EM}/a)$ shift in the untwisted mass is common. Therefore it is plausible that one can determine the critical mass for each pair by enforcing the recovery of the corresponding valence-sea chiral SU(2). Specifically, $m_{cr,u}$ is determined by

$$\langle \pi^u_{SV} | \partial_\mu (\bar{u}_S \gamma_\mu \gamma_5 u_V) | 0 \rangle \Big|_{m_{0,u}=m_{cr,u}} = 0\,, \tag{A.9}$$

while $m_{cr,d}$ is determined by the analogous condition with $u \to d$:

$$\langle \pi^d_{SV} | \partial_\mu (\bar{d}_S \gamma_\mu \gamma_5 d_V) | 0 \rangle \Big|_{m_{0,d}=m_{cr,d}} = 0\,. \tag{A.10}$$

Here $\pi^u_{SV}$ and $\pi^d_{SV}$ are sea-valence pions composed, respectively, of up and down quarks.

When using a partially quenched theory, one also needs to add ghost fields, $\tilde{u}_V$ and $\tilde{d}_V$, to cancel the valence quark determinants.[5] Thus the full softly-broken chiral symmetry is the graded group $SU(4|2)_L \times SU(4|2)_R$. This raises the question of whether complications arising from partial quenching, or from discretization effects, can lead to corrections to the tuning criteria of Eqs. (A.9) and (A.10). This is one of the issues we address here by mapping these conditions into $\chi$PT.

We begin by mapping the mass matrix in the unquenched sector into $\chi$PT. The four parameters of Eq. (A.8) map into

$$\chi = \begin{pmatrix} \hat{m}_u e^{i\omega_u} & 0 \\ 0 & \hat{m}_d e^{-i\omega_d} \end{pmatrix} = \begin{pmatrix} (\widehat{m}_q + \hat{\epsilon}_q) e^{i(\omega+\varphi)} & 0 \\ 0 & (\widehat{m}_q - \hat{\epsilon}_q) e^{i(-\omega+\varphi)} \end{pmatrix}. \tag{A.11}$$

The choice of sign for $\omega_d$ is such that it is positive with a $\tau_3$ twist. $\chi$ contains the additional parameter $\varphi$ compared to the mass matrix analyzed in the main text, Eq. (3.27). $\varphi$ is a

[4]This description is equivalent to that of Ref. [23], but differs technically in two ways. First, we find that one need only introduce two valence quarks to describe the method, rather than the four used in Ref. [23]. This does not impact the method itself, only its description. Second, we work in the twisted basis, rather than the physical basis used in Ref. [23].

[5]For reviews of partially quenched theories and the corresponding $\chi$PT, see Refs. [59, 33].

measure of the difference between up and down twist angles,

$$\omega_u = \omega + \varphi\,, \qquad \omega_d = \omega - \varphi\,. \tag{A.12}$$

As discussed in Sec. 3.5, such a difference corresponds to the introduction of a nonzero $\theta_{\rm QCD}$—the explicit relation is $\varphi = \theta_{\rm QCD}/2$.

We note that the relations between the bare masses of Eq. (A.8) and the parameters of $\chi$ in Eq. (A.11)—which can be worked out along the lines of the previous appendix—are not needed here. All we need to know is that, if $m_{0,u} = m_{cr,u}$ and $m_{0,d} = m_{cr,d}$, then both up and down masses are fully twisted. Thus the twist angles in $\chi$ are $\omega_u = \omega_d = \pi/2$, implying maximal twist with no $\theta_{\rm QCD}$ term: $\omega = \pi/2$ and $\varphi = 0$. Reaching this point in parameter space is the aim of tuning.

When considering the PQ extension of this theory, we will focus mainly on the quark sector, since the ghosts do not play a significant role. Collecting the four quark fields in the order

$$\psi_{PQ}^{\top} = (u_S, u_V, d_V, d_S)\,, \tag{A.13}$$

the extended quark mass matrix is

$$\chi_{PQ} = \begin{pmatrix} (\widehat{m}_q + \hat{\epsilon}_q)e^{i\omega_u\tau_3} & 0 \\ 0 & (\widehat{m}_q - \hat{\epsilon}_q)e^{i\omega_d\tau_3} \end{pmatrix}\,. \tag{A.14}$$

The factors of $\tau_3$ arise because, by construction, valence quarks have opposite twisted masses to the corresponding sea quarks. We stress that the $\mathcal{O}(\alpha_{\rm EM}/a)$ shifts are incorporated into the parameters $\widehat{m}_q$ and $\hat{\epsilon}_q$, along with the usual $\mathcal{O}(1/a)$ shifts. We can also include the $\mathcal{O}(a)$ shifts in the same fashion.

To implement the conditions (A.9) and (A.10) in the PQ theory, we need the extension of $\Sigma$ to this theory. This is a $6 \times 6$ matrix transforming in the usual way under $SU(4|2)_L \times SU(4|2)_R$. In fact, as we only need matrix elements for states composed of quarks, and since we know from Ref. [7] that there are no quark-ghost condensates, we can focus on the $4 \times 4$ quark sub-block, which we call $\Sigma_{PQ}$. We now argue that the expectation value of $\Sigma_{PQ}$ has

the form

$$\langle \Sigma_{PQ} \rangle = \mathrm{diag}(e^{i\theta}, e^{-i\theta}, e^{i\theta}, e^{-i\theta}) \,. \tag{A.15}$$

This is based on the following results. First, the unquenched $2 \times 2$ block of $\Sigma_{PQ}$ (i.e. that involving the first and last rows and columns) is just the unquenched $\Sigma$ field. This is unaffected by partial quenching [54, 55], and its expectation value is given by an unquenched $\chi$PT calculation. This calculation must include not only nondegeneracy, electromagnetism and twist, but also nonvanishing $\theta_{\mathrm{QCD}}$. To our knowledge such an analysis has not previously been done, so we carry it out in Chapter 4.The result is that the unquenched condensate $\langle \Sigma \rangle$ only rotates in the $\tau_3$ direction—there are no off-diagonal condensates such as $\langle \bar{u}_S d_S \rangle$. This fixes the first and last entries in Eq. (A.15) to have opposite phase angles.

This is an important result for the following, so we emphasize its key features. Although $\theta_{\mathrm{QCD}} \neq 0$ leads to an overall phase in the mass matrix [$e^{i\varphi}$ in Eq. (A.11)], its effect on the condensate $\langle \Sigma \rangle$ is qualitatively similar to that of a twist $\omega$, despite the fact that the latter leads to opposite phases on $u$ and $d$ quarks. This happens because $\Sigma$ is constrained to lie in $SU(2)$, and so has no way to break parity other than rotating in the $\tau_3$ direction. An overall phase rotation would take it out of $SU(2)$ into the $U(2)$ manifold.

The second result needed to obtain Eq. (A.15) is the existence of relations between valence and sea-quark condensates. In particular, one can show that

$$\langle \bar{u}_V u_V \rangle = \langle \bar{u}_S u_S \rangle \quad \text{and} \quad \langle \bar{u}_V \gamma_5 u_V \rangle = -\langle \bar{u}_S \gamma_5 u_S \rangle \,, \tag{A.16}$$

to all orders in the hopping parameter expansion. The minus sign in the second relation follows from the opposite twisted mass of sea and valence quarks. The result (A.16) holds on each configuration and thus also for the ensemble average, even though the measure is complex for $\theta_{\mathrm{QCD}} \neq 0$. Since the additive and multiplicative renormalizations of these condensates are the same for valence and sea quarks, the result (A.16) implies that valence and sea up-quark condensates have opposite "twists", $e^{\pm i\theta}$. The same argument applies to the down-quark condensates, and taken together these arguments determine the form of the second and third diagonal elements in Eq. (A.15).

The final result needed to obtain the form (A.15) is the vanishing of off-diagonal condensates involving one or more valence quarks, e.g. $\langle \bar{u}_V d_V \rangle$ and $\langle \bar{u}_V d_S \rangle$. These differ from the diagonal condensates in that there is no mass term in the quark-level Lagrangian that can serve as a source for such condensates. Thus to determine whether they are nonzero one must add a source, e.g. $\Delta \bar{d}_V u_V$, calculate the resulting condensate, send the volume to infinity, and finally send the parameter $\Delta \to 0$. This analysis has been carried out in Appendix A of Ref. [36] in a theory with twisted-mass quarks, although, unlike our situation, the quarks were degenerate and $\theta_{\rm QCD} = 0$. The general lessons from Ref. [36] are (i) that to obtain a nonvanishing condensate one needs a source of infrared divergence to cancel the overall factor of $\Delta$, and (ii) that nonvanishing twisted masses cut off such divergences. These lessons apply also for all the off-diagonal condensates that we consider here. However, the argument as given in Ref. [36] assumes that the measure is real and positive, which does not hold here. Nevertheless, since we are tuning to $\theta_{\rm QCD} = 0$, we expect the impact of having a complex measure to be small. Furthermore, we know from Chapter 3that the corresponding sea quark condensates, e.g. $\langle \bar{u}_S d_S \rangle$ and $\langle \bar{u}_S \gamma_5 d_S \rangle$, vanish even when $\theta_{\rm QCD} \neq 0$. These condensates differ from those containing valence quarks only by changing the signs of some of the twisted masses. Since it is the presence of these masses, and not their detailed properties, that leads to the vanishing of the condensate, we expect the result holds for all off-diagonal condensates.

With the form (A.15) in hand, we can now apply the tuning conditions (A.9) and (A.10) in $\chi$PT. We do so by generalizing the analysis of Ref. [58], where the twist angle for unquenched twisted-mass fermions was determined in $\chi$PT by applying a PCAC-like condition. The required extension is from the $SU(2)$ sea-quark sector alone to the full valence-sea $SU(4)$ symmetry. Much of the analysis carries over with minimal changes from Ref. [58], so we only sketch the calculation.

The first step is to obtain the pion fields that couple to external particles in the tuning conditions. Following Ref. [58], we obtain these by expanding the chiral field about its

vacuum value as

$$\Sigma_{PQ} = \xi_{PQ}\, e^{2i\Pi/f}\, \xi_{PQ}\,, \tag{A.17}$$

$$\Pi = \sum_{a=1}^{15} \pi_a \lambda_a\,, \tag{A.18}$$

$$\xi_{PQ} = \sqrt{\langle \Sigma_{PQ} \rangle} = \mathrm{diag}(e^{i\theta/2}, e^{-i\theta/2}, e^{i\theta/2}, e^{-i\theta/2})\,. \tag{A.19}$$

Here $\lambda_a$ are the generators of SU(4), with $\pi_a$ the corresponding pion fields. These are the pions in the PQ theory that are composed of quarks alone, with no ghost component.[6] The pions needed for tuning, $\pi^u_{SV}$ and $\pi^d_{SV}$, are contained in the upper and lower diagonal $2 \times 2$ blocks of $\Pi$, respectively.

The next step is to determine the form, in $\chi$PT, of the axial currents appearing in the tuning conditions. These can be obtained by introducing sources into derivatives using standard methodology. Since, by definition, our chiral potential does not contain derivatives, at LO$^+$ only the LO kinetic term [shown in Eq. (3.2)] enters into the determination of the currents. We do not display the form of the currents, however, as the calculation needed for each of the tuning conditions is *exactly* the same as that carried out in Ref. [58]. This is because each tuning condition involves a separate, nonoverlapping $SU(2)$ subgroup of $SU(4)$ (upper-left or lower-right $2 \times 2$ block), and because the condensate (A.15) does not connect these subgroups. We simply quote the results of the calculation:

$$\langle \pi^u_{SV} | \partial_\mu (\bar{u}_S \gamma_\mu \gamma_5 u_V) | 0 \rangle \propto \cos\theta\,, \tag{A.20}$$

$$\langle \pi^d_{SV} | \partial_\mu (\bar{d}_S \gamma_\mu \gamma_5 d_V) | 0 \rangle \propto \cos\theta\,. \tag{A.21}$$

Thus enforcing either (A.9) or (A.10) has the effect of setting $\theta = \pm\pi/2$ and the condensate to

$$\langle \Sigma_{PQ} \rangle = \pm \mathrm{diag}(i, -i, i, -i)\,, \tag{A.22}$$

For our choices of signs of the twisted masses $\mu_{0,u}$ and $\mu_{0,d}$ in Eq. (A.8), the $\pm$ signs are in fact plusses, i.e. $\theta = \pi/2$.

[6] A similar form to Eq. (A.19) holds for the full $6 \times 6$ PQ chiral field, but we can focus on the $SU(4)$ block, since the pions we leave out in this way are those containing one or more ghost fields.

A surprising aspect of this result is that the two tuning conditions are not independent: if one enforces, say, Eq. (A.9) then Eq. (A.10) will be automatically satisfied. This dependence arises because changing $m_u$ in turn changes $\varphi$ and $\omega$ and this impacts the $d$ condensate through the quark determinant. One might, therefore, wonder how the two tuning conditions have been successfully applied in Ref. [23]. To understand this, we note that this work makes two approximations. First, isospin-breaking effects are evaluated only through linear order in an expansion in $m_u$–$m_d$ and $\alpha_{\rm EM}$. Second, insertions of $m_u$–$m_d$ or photons on sea-quark loops are dropped (the "electroquenched approximation"). The latter approximation has the effect of disconnecting the two tuning conditions—all quark loops in both conditions are evaluated with uncharged, degenerate sea-quarks, so the $u$-quark condensate cannot be impacted by changes in $m_d$ and vice versa. Since $\chi$PT predicts that there is a tight correlation between the condensates, it appears to us that the electroquenched approximation is theoretically problematic. However, from a purely numerical viewpoint, the dropped contributions may well lead only to small corrections.

The lack of independence implies that the tuning conditions cannot determine both $m_{u,c}$ and $m_{d,c}$—only one constraint on these two critical masses is obtained. In terms of the parameters of mass matrix (A.11), the conditions determine only a relation between $\omega$ and $\varphi$. Thus, after enforcing either (A.9) or (A.10) the theory is known to lie along a line in the $\omega$—$\varphi$ plane. In terms of the bare masses, the theory lies along a line in the $m_{0,u}$—$m_{0,d}$ plane (with, recall, $\mu_{0,u}$ and $\mu_{0,d}$ fixed at the values leading to physical quark masses when $m_{0,u} = m_{0,d} = 0$). We do know that this one-dimensional subspace includes the point we are trying to tune to, namely that with $(\omega, \varphi) = (\pi/2, 0)$. This follows from the analysis of Sec. 3.5.1. At maximal twist with $\varphi = 0$, the twist in the condensate is also maximal, i.e. $\theta = \pi/2$. The only caveat is that the values of the twisted masses must be such that one lies in the continuum-like phase, rather than the CP-violating phase (see Fig. 3.4).

To complete the tuning we need an additional condition that forces us to the desired point along the allowed line. At first blush one might expect that it would be simple to find an

additional tuning condition, since theories with $\theta_{\rm QCD} \neq 0$ have explicit parity violation. This is in contrast to the parity violation induced by a nonzero twist $\omega$ which, in the continuum limit, can be removed by a chiral rotation. This suggests that one should look for quantities that vanish when parity is a good symmetry. The flaw in this approach is that parity is broken by $\omega \neq 0$ away from the continuum limit—the chiral rotation required to obtain the parity-symmetric form is not a symmetry on the lattice. Thus the distinction between $\varphi \neq 0$ and $\omega \neq 0$ no longer holds.

The only choice that we have found for a second condition involves using the pion masses. Specifically, we find that, along the line picked out by setting $\theta = \pi/2$, the masses of both charged and neutral pions are minimized when $\varphi = 0$. This assumes only that we are in the continuum-like phase for the physical values of $\mu_{0,u}$ and $\mu_{0,d}$.

The details of the calculation are presented in Chapter 4.Working at LO$^+$, we find that the constraint $\theta = \pi/2$ forces the quark masses to lie on the line

$$\frac{\hat{m}_d}{\hat{m}_u} = -\left(\frac{1 - c_\ell(\hat{\mu}_u - \hat{\mu}_d)}{1 + c_\ell(\hat{\mu}_u - \hat{\mu}_d)}\right) . \tag{A.23}$$

As noted above, this line passes through the desired point $m_u = m_d = 0$. The slope is $-1$ when $c_\ell = 0$, and increases in magnitude as $c_\ell$ increases (assuming the physical situation $\hat{\mu}_u < \hat{\mu}_d$). There is no singularity when the slope reaches infinity—this simply means that the constraint line is the $m_u = 0$ axis. For larger $c_\ell$ the slope is positive. It decreases with increasing $c_\ell$, though it always remains greater than unity. The pion masses along the constraint line are

$$m^2_{\pi^0} = \frac{\hat{\mu}_u + \hat{\mu}_d}{2} - 2c_\ell \left(\frac{\hat{\mu}_u - \hat{\mu}_d}{2}\right)^2 + 2c_\ell \left(\frac{\hat{m}_u - \hat{m}_d}{2}\right)^2 - 2w' , \tag{A.24}$$

$$m^2_{\pi^\pm} = \frac{\hat{\mu}_u + \hat{\mu}_d}{2} + 2c_\ell \left(\frac{\hat{m}_u - \hat{m}_d}{2}\right)^2 + 2c_{\rm EM} . \tag{A.25}$$

Thus we see that both masses are minimized along the constraint line when $m_u = m_d = 0$. If one were to implement this tuning condition in practice, then one would apply it for the charged pion masses, since these have no quark-disconnected contractions.

This analysis breaks down when $c_\ell$ gets too large, because the theory with $m_u = m_d = 0$ then lies in the the CP-violating phase. This can be seen from the result (A.24)—for large enough $c_\ell$ the squared neutral pion mass becomes negative. This happens sooner for the first-order scenario, $w' > 0$.

We close this section by commenting on the impact of higher-order terms in $\chi$PT. Because of such terms, even if one perfectly implements our two tuning conditions—namely either Eq. (A.9) or (A.10) and minimizing the pion masses—one will not have precisely tuned to $m_u = m_d = 0$. This can be seen, for example, from the analysis of Ref. [58], where terms of $\mathcal{O}(ap^2, am)$ lead to maximal twist occurring at untwisted masses of $\mathcal{O}(a\mu)$, with $\mu$ the twisted mass, rather than zero. Shifts of this size occur also in the presence of isospin breaking, although the detailed form of the corrections will differ. Within our power-counting, however, $\mu \sim a^2$ so that the shifts in the untwisted masses are $\sim \mathcal{O}(a^3)$, beyond the order that we consider.